Use of Traveling Wave Signatures in Medium-Voltage Distribution Systems for Fault Detection and Location

Kumaraguru Prabakar,[1] Akanksha Singh,[1]
Matthew Reynolds,[1] Monte Lunacek,[1] Lucas Monzón,[2]
Yaswanth Nag Velaga,[1] Jonathan Maack,[1]
Soumya Tiwari,[1] Jinia Roy,[1] Colin Tombari,[1]
Ismael Mendoza Carrillo,[1] Xinshuo Yang,[1]
Spatika Iyengar,[1] William John,[1] Dhananjay Anand,[3]
Avi Gopstein,[3] and Deepthi Vaidhynathan[1]

1 National Renewable Energy Laboratory
2 University of Colorado, Boulder
3 National Institute of Standards and Technology

NREL is a national laboratory of the U.S. Department of Energy
Office of Energy Efficiency & Renewable Energy
Operated by the Alliance for Sustainable Energy, LLC

This report is available at no cost from the National Renewable Energy Laboratory (NREL) at www.nrel.gov/publications.

Contract No. DE-AC36-08GO28308

Technical Report
NREL/TP-5D00-78057
August 2021

Use of Traveling Wave Signatures in Medium-Voltage Distribution Systems for Fault Detection and Location

Kumaraguru Prabakar,[1] Akanksha Singh,[1]
Matthew Reynolds,[1] Monte Lunacek,[1] Lucas Monzón,[2]
Yaswanth Nag Velaga,[1] Jonathan Maack,[1]
Soumya Tiwari,[1] Jinia Roy,[1] Colin Tombari,[1]
Ismael Mendoza Carrillo,[1] Xinshuo Yang,[1]
Spatika Iyengar,[1] William John,[1] Dhananjay Anand,[3]
Avi Gopstein,[3] and Deepthi Vaidhynathan[1]

1 National Renewable Energy Laboratory
2 University of Colorado, Boulder
3 National Institute of Standards and Technology

Suggested Citation
Prabakar, Kumaraguru, Akanksha Singh, Matthew Reynolds, Monte Lunacek, Lucas Monzón, Yaswanth Nag Velaga, Jonathan Maack, Soumya Tiwari, Jinia Roy, Colin Tombari, Ismael Mendoza Carrillo, Xinshuo Yang, Spatika Iyengar, William John, Dhananjay Anand, Avi Gopstein, and Deepthi Vaidhynathan. 2021. *Use of Traveling Wave Signatures in Medium-Voltage Distribution Systems for Fault Detection and Location*. Golden, CO: National Renewable Energy Laboratory. NREL/TP-5D00-78057. https://www.nrel.gov/docs/fy21osti/78057.pdf.

NREL is a national laboratory of the U.S. Department of Energy
Office of Energy Efficiency & Renewable Energy
Operated by the Alliance for Sustainable Energy, LLC

This report is available at no cost from the National Renewable Energy Laboratory (NREL) at www.nrel.gov/publications.

Contract No. DE-AC36-08GO28308

Technical Report
NREL/TP-5D00-78057
August 2021

National Renewable Energy Laboratory
15013 Denver West Parkway
Golden, CO 80401
303-275-3000 • www.nrel.gov

NOTICE

This work was authored in part by the National Renewable Energy Laboratory, operated by Alliance for Sustainable Energy, LLC, for the U.S. Department of Energy (DOE) under Contract No. DE-AC36-08GO28308. Funding provided the U.S. Department of Energy Office of Energy Efficiency and Renewable Energy Solar Energy Technologies Office. The views expressed herein do not necessarily represent the views of the DOE or the U.S. Government.

This report is available at no cost from the National Renewable Energy Laboratory (NREL) at www.nrel.gov/publications.

U.S. Department of Energy (DOE) reports produced after 1991 and a growing number of pre-1991 documents are available free via www.OSTI.gov.

Cover Photos by Dennis Schroeder: (clockwise, left to right) NREL 51934, NREL 45897, NREL 42160, NREL 45891, NREL 48097, NREL 46526.

NREL prints on paper that contains recycled content.

Executive Summary

Protection systems are a critical for the proper operation of an electric grid. Protection systems are expected to quickly detect, identify, locate, and isolate faults that may damage grid components and cause outages. As more inverter-based photovoltaics (PV) are integrated into the grid, protection schemes that rely on signal processing in the phasor domain become less effective due to lower fault current from inverters or because the inherent latency in phasor domain detection is too slow to accurately identify and locate faults. These reasons among others highlight the need for signal processing and protection approaches tailored for distribution systems with high penetrations of inverter-based PV.

The main objective of this project is to develop protection schemes that detect faults using time domain fault signatures to enable more accurate and faster detection and localization in distribution systems and/or microgrids with high penetrations of inverter-based PV. Our approach aims to exploit traveling waves that are generated during a fault. Traveling wave analysis is suitable for systems with high penetrations of inverter-based PV because it does not depend on large fault currents or phasor information used by traditional protection schemes. Traveling wave-based protection schemes can be implemented at both the transmission and distribution system levels to simultaneously ensure the stability of the distribution system and the reliability of the bulk power system. As such, this project aims to enable increased deployment of inverter-based PV systems by addressing a critical operational barrier.

This report presents the research work on traveling wave-based fault detection and identification for distribution systems performed at the National Renewable Energy Laboratory in collaboration with the University of Colorado at Boulder and the National Institute of Standards and Technology. The report includes the following topics:

- Background on traveling wave phenomena in power systems;
- High-fidelity modeling of the distribution system for traveling wave studies;
- Medium-voltage fault experiments performed on test hardware and in the field;
- Signal-processing tools used to extract traveling waves from wide band current measurements; and
- A visualization tool to show the path of traveling waves in the distribution system.

Acknowledgments

This work was authored by the National Renewable Energy Laboratory, operated by Alliance for Sustainable Energy, LLC, for the U.S. Department of Energy (DOE) under Contract No. DE-AC36-08GO28308. This material is based upon work supported by the U.S. Department of Energy's Office of Energy Efficiency and Renewable Energy (EERE) under Solar Energy Technologies Office (SETO) Agreement Number 34237. The views expressed in the article do not necessarily represent the views of the DOE or the U.S. Government. The U.S. Government retains and the publisher, by accepting the article for publication, acknowledges that the U.S. Government retains a nonexclusive, paid-up, irrevocable, worldwide license to publish or reproduce the published form of this work, or allow others to do so, for U.S. Government purposes.

We are grateful to the U.S. Department of Energy Office of Energy Efficiency and Renewable Energy Solar Energy Technologies Office (SETO) for supporting this research. Specifically, we acknowledge David Walter, technology manager for the SETO Systems Integration team, and Hariharan Krishnaswami, ORISE Science and Technology Policy Senior Fellow, for their support, feedback, and encouragement.

The authors thank Gregory Martin, John Fossum, John Nangle, and Cat Wong for their review and valuable comments.

The authors would also like to thank Etienne Toutain, Loïc Joseph-Auguste, and Nikola Stankovic for their help with the experiments.

Contents

List of Figures

List of Tables

1 Introduction

Electric grid protection systems prevent or minimize damage to grid components and mitigate disruptions to customers when a fault occurs. Protection schemes are designed to detect faults as quickly as possible and isolate affected parts of the system while maintaining electrical service for as many customers as possible. Traditional protection schemes for distribution systems and microgrids use phasor domain information. These protection schemes are fast, but they rely on certain characteristics of existing generators to function properly. One characteristic is that when a "fault" occurs, synchronous generators produce a large amount of fault current—typically six times the rated current (Kroposki et al. 2017). Because the protection system can detect this high level of fault current, it can quickly open a protective device, such as a breaker or fuse. These schemes also use directional components and settings that are typically not dynamic. For example, relays have different profiles and settings that can be switched to account for different load profiles or for the time of day; however, existing protection systems need to adapt to the characteristics of grids with a high penetration of inverter-based resources (IBRs), such as photovoltaics (PV) and wind power. Such high penetrations can cause bidirectional power flow and have much lower levels of fault current. In this scenario, the existing protection system based on overcurrent measurements is inadequate and unable to react to a variety of faults. This project studies traveling wave-based protection schemes as an innovative method to overcome these challenges and facilitate the widespread deployment of IBRs in distribution systems.

1.1 Impact

Presently, penetration of IBRs in distribution systems is primarily limited by voltage constraints on their grid ties. These constraints that can be overcome if inverters were allowed to regulate voltage locally using shared measurements. In fact, these changes are being addressed in the updated version of interconnection standards, such as the Institute of Electrical and Electronics Engineers (IEEE) 1547 IEEE 2018. These changes enable increased penetration levels of IBRs on distribution circuits, but don't fully address ensuing protection system challenges. Existing protection systems fail to reliably operate with decreased fault current levels and reverse power flow. These conditions may become more prevalent with emerging control standards but are also being experienced by electric utilities when deploying IBRs currently. This report documents a project that considers the use of intelligent electronic devices (IEDs) that can detect traveling waves emerging from fault features and so may improve fault detection in high IBR circuits. The results from the project indicate that while sensor and measurement requirements are significant for traveling wave detection, the algorithms required to isolate faults are scalable to distribution sized circuits providing a optimistic roadmap to implementation in real circuits.

1.2 Use of Traveling Wave-Based Protection Approach in Distribution Systems

Electrical faults on transmission and distribution lines are detected and isolated by protective devices. Fast and precise fault location plays an important role in accelerating system restoration, reducing outage time and significantly improving system reliability. It has been documented that faults on the medium-voltage (11-kV) network in the United States were responsible for 74% of the outage time experience by customers averaging to 20 minutes per customer per year (Zidan et al. 2017); therefore, distribution systems contribute the most to power supply unavailability to users (Kavousi-Fard and Niknam 2014).

The North American bulk power system (BPS) and electric grids around the world are undergoing rapid changes in generation resource mix with increasing amounts of renewable generation, such as wind and PV power plants (*Reliability Guideline BPS-Connected Inverter-Based Resource Performance* 2018). These resources are either completely or partially interfaced with the BPS through power electronics (referred to as IBRs). Regardless of the type of resource, it is paramount that all BPS-connected resources provide essential reliability services and operate in a manner that supports BPS reliability. Disturbance analysis of BPS-connected solar PV tripping has identified several areas where the performance of IBRs can be improved.

For example, on August 16, 2016, the Blue Cut Fire caused a 500-kV line fault that cleared normally (less than three cycles) but resulted in the widespread loss of 1,178 MW of PV generation. This event was the primary focus of the North American Electric Reliability Corporation/Western Electricity Coordinating Council joint task force, which identified two key issues: first, inverters were tripping erroneously on instantaneous frequency measurements; second,

most inverters are configured to momentarily cease injection of current for voltages outside the continuous operating range of 0.9 p.u.–1.1 pu (NERC 2017). This report highlights the nuance of designing protection schemes around IBRs.

Looking to the future, fault detection, isolation, and service restoration are key building blocks for the self-healing capability of advanced distribution management systems. Although most interruptions are caused by faults in distribution networks, the adaptation of the successful fault location algorithms developed for the transmission system is limited by the topology and operating principles of the distribution system (i.e., nonhomogeneous feeders, load taps, laterals, radial operation, and the available measuring equipment). The presence of laterals implies that the estimated distances could correspond to several possible fault locations in the distribution system. The main techniques used to determine the location of a fault are one-terminal and two-terminal impedance-based methods, synchronized sampling methods, and traveling wave methods ("IEEE Guide for Determining Fault Location on AC Transmission and Distribution Lines" 2015). These methods make simplifying assumptions and have accuracy limitations even under ideal conditions.

Unlike protective relays, which need to detect whether faults are in the zones established by transformer locations, fault location data must be very accurate to save time and reduce the expenses of crews searching in bad weather and/or over rough terrain. Traveling wave methods use signals that are generated by a fault that can be resolved in space and time ("IEEE Guide for Determining Fault Location on AC Transmission and Distribution Lines" 2015). Traditionally, locating traveling wave faults required only a few signal processing tools that were relatively easy to implement—namely, the ability to measure, filter, and amplify surges; the ability to measure time with microsecond accuracy; and the ability to communicate with a relatively constant latency. In transmission systems, traveling wave-based fault-locating methods can approach an accuracy of 300 m, or one tower span. Advancements in the technology—especially high-speed sampling, digital signal processing, satellite-based synchronization, and digital communications—enable further improvements in traveling wave-based fault location in transmission systems. Traveling wave-based fault location in transmission systems have recently been integrated with microprocessor-based line protection relays, improving convenience and reducing the cost of ownership to utilities.

In distribution systems, however, traveling wave signals might be difficult to interpret because of the presence of laterals and load taps. Further, the limited bandwidth of conventional current transformers and voltage transformers directly curtails the resolution of fault localization (Zidan et al. 2017). Current weaknesses can be summarized as follows:

1. Signal processing methods cannot accurately distinguish fault-originated traveling wave features from other broadband signals that are generated by fault transients since localization requires model based fitting to boost the signal to noise ratio.
2. Fault-originated traveling waves propagate along the distribution lines in both directions away from the fault point and are reflected at line terminations, junctions between feeders, laterals, and the fault location. Observations of these reflections occur at fixed points along the line where the spatial context of these multiple reflected modes may not be discernable.

Research addressing the specific concerns in signal processing based distribution circuit protection issues under high penetrations of IBRs is active and varied. Some noteworthy examples include *adaptive protection* (Che, Khodayar, and Shahidehpour 2014), where protection settings and parameters are computed a-priori for changing circuit conditions such as reconfiguration and microgrid islanding. These systems change the protective relay trigger envelope to account for significant changes to the grid, but besides the optimization of parameters for operating modes and online implementation of the scheme still relies on overcurrent and differential schemes based protection. *Setting less* protection schemes (Meliopoulos et al. 2013) computes protection parameters on-line based on a continuously retuned model of the grid run in real time. This method allows precise protection of the grid, but it relies heavily on the use of an accurate model of the system and the use of communications to exchange system measurements.

The approach presented here is significantly different from these methods because it relies on traveling waves that are generally agnostic to originating fault type and the power flow condtions of the grid itself. Traveling wave signatures are *out-of-band* to the power flow signals.

Currently, traveling wave based fault localization has only been used for transmission-level protection schemes on a limited basis. Using traveling wave information in distribution systems theoretically support faster fault localization than existing methods that depend on large fault currents from the substation and zoned protection. Existing traveling wave based protection schemes for transmission systems do not directly translate to distribution circuits due in part to denser and potentilly meshed network architecture with IBRs. Challenges also extend to modeling, testing, and implemention of algorithms in a distribution system. This project targets these challenges as part of the process to develop traveling wave-based protection schemes for distribution systems (with or without microgrids) with high penetrations of IBRs.

In addition to research on distribution system protection, the traveling wave phenomena and their application to power systems have been studied by many researchers across the world. In lieu of a literature survey in this report, a comprehensive list of more than 1,000 articles published in conferences, journals, and books has been compiled by the National Renewable Energy Laboratory (NREL) library and the project team and serves as a comprehensive collection of related and background material literature. This database of references[1] is a valuable resource to anyone looking to develop an understanding of the various technical challenges, nuances and improvements to the field of traveling wave based fault localization.

This report is organized into the following chapters:

- Chapter 2 presents the modeling approach required to simulate traveling wave phenomena in distribution systems.
- Chapter 3 presents the details of test circuits modeled using electromagnetic transient (EMT) simulation software. The chapter also covers the various test scenarios considered and results from the EMT simulations.
- Chapter 4 presents details of the medium-voltage fault experiments performed to recreate traveling waves in a controlled environment. This chapter also presents the details of the measurement hardware used to capture traveling waves.
- Chapter 5 presents the signal-processing tools used to extract traveling wave information from the experimental data.
- Chapter 6 presents the details of the tool developed to visualize traveling waves using Bewley lattice charts.
- Chapter 7 presents the analysis performed on the experimental results using the signal-processing tool and visualization tool developed in the project.
- Chapter 8 concludes and provides insights to follow-on work that will help enable the use of the traveling wave-based protection approach in distribution systems.

[1] https://www.zotero.org/groups/2292877/traveling_wave_literature/library

2 Software Simulation of Distribution System/Microgrids using Electromagnetic Transient Simulations for Fault Characterization and Analysis

In this chapter we discuss methods to improve the capability of software tools to simulate the propagation of fault signtures through an electrical circuit. Although our emphasis is on point faults on distribution systems with a high IBR penetration, our analysis is useful for improving the accuracy and/or speed of simulations in relation to a variety of circuit and fault types. The software improvements developed by the team and documented in this chapter stem from four interconnected tasks performed in this work:

1. A distribution line test facility at NREL's Energy Systems Integration Facility (ESIF) was used to physically generate and observe traveling waves in a distribution line segment (see Chapter 4).
2. Electromagnetic transient programs (EMTPs) were used to model wideband propagation models for larger networks resembling archetypical distribution networks (see Section 3).
3. To complement and enhance the ESIF medium voltage line experiments, energized, online fault experiments were performed at an external site (the EDF Concept Grid in France). The description of these tests is presented in Chapter 4.
4. An extensive literature review was performed to understand the mismatch between the experimental and EMTP results, which motivated the developments described in this chapter.

As a result of our research and experiments, we believe that current software tools for EMT computations have limitations with respect to simulating realistic distribution systems with high levels of IBRs or when trying to reproduce signals from some types of faults. These limitations manifest in a mismatch between experimental and simulation results – often stymiying validation and evalutation efforts. Part of the problem can be attributed to using algorithms that are adequate for transmission systems but insufficient for complex distribution systems. Other factors also play a role in simulation discrepancies including, high-frequency voltage and current signatures, non-transposed lines, underground cables and multiphase systems with lines having different characteristics.

After our initial testing and experiments, we found that it is important to confirm or clarify simulation results. For that reason, we interacted with software developers at PSCAD and EMTP-RV to discuss several issues and understand the capabilities and limitations of their software. Our main conclusions can be summarized as follows:

1. Subtle mathematical modeling choices can lead to a significant loss of accuracy.
2. To improve efficiency, several modeling simplifications are typically introduced that are detrimental to the accuracy of the final results.
3. Improvements are possible. We identified several areas where changes in modeling and/or algorithms lead to improved accuracy and improve the speed of computations.

The next sections are organized as follows: Section 2.1 begins by reviewing line modeling techniques. Section 2.2, discusses our general theoretical approach and includes a description of our software development to test and verify our proposed techniques. The chapter finishes with Section 2.3, which presents additional derivations and observations to improve two other aspects of typical simulations—namely, interpolation and numerical integration.

2.1 Distribution Line Modeling

EMT propagation models for overhead lines and underground cables can be split into time and frequency domains. These domains require different algorithms to solve equations and to obtain nodal voltage and current solutions for each conductor. In time-domain modeling, boundary conditions are naturally integrated into the algorithm because they correspond to actual or simulated time measurements; however, the time-domain modeling can be complicated since intrinsic properties of the conductor (called line parameters) are frequency dependent. For this reason, equations formulated in the frequency domain are commonly used to compute transformed current and voltage. An important aspect of this approach is that general solutions for the frequency-domain equations can be explicitly derived;

this property is exploited in all frequency-domain approaches. Nevertheless, the frequency-domain solutions cannot be easily converted into accurate time-domain solutions, which led to a variety of approaches that—one way or another—try to circumvent the computational problems using different assumptions. To understand the impact of the simplifications and assumptions used in transmission line models and how the different models deal with the frequency dependence of the line parameters, we started our literature review on the well-established line models of Dommel and Marti (c.f. (Martí 1981; Martí 1982)). These authors have contributed extensively to the EMTP software (Dommel 1996), which contains the core algorithms for the most widely used software for modeling and simulating EMTs in electrical transmission systems. The alternate stream of EMTP-type programs could use new numerical methods and modeling approaches and provide significantly improved capabilities and numerical performance. Some examples include PSCAD-EMTDC and EMTP-RV. Although Marti's work addressed and complemented important features in Dommel's line model, there are still important modeling issues that need to be addressed. One example is the issue of transitioning from transmission system modeling to multiconductor distribution system modeling. For a comprehensive review of multiconductor line models, we recommend (Paul 1994; Paul 2007).

The two-conductor equation (also called the telegrapher's equation) is the system of linear partial differential equations in time t and position x along the line:

$$\begin{cases} \frac{\partial}{\partial x} v(x,t) = -l \frac{\partial}{\partial t} i(x,t) - ri(x,t) \\ \frac{\partial}{\partial x} i(x,t) = -c \frac{\partial}{\partial t} v(x,t) - gv(x,t) \end{cases} \tag{2.1}$$

where v is the voltage; i is the current; and the line parameters l, r, c, g are the inductance, resistance, capacitance, and conductance—all in per-unit length representation. Note that at this stage we are considering this equation under the assumption that the conductors are parallel to each other, the line parameters are constant, and there is no incident field excitation. More generally, for the multiconductor transmission line equations, we also assume that the $n+1$ conductors have length l and that they are parallel to each other and the x-axis; that the network terminals are at the source ($x = 0$) and at the load ($x = l$); and that the n line voltages are with respect to the (arbitrarily chosen) reference conductor (the zeroth conductor). It is also assumed that there are no components of the electric and magnetic fields that are directed along the line's x-axis. For this transverse electromagnetic field structure assumption, it can be shown that the sum of the currents on all $n+1$ conductors in the x direction at any cross section is zero. This is the basis for saying that the currents of the n conductors return through the reference conductor. The multiconductor transmission line equations are formally the same as in (2.1):

$$\begin{cases} \frac{\partial}{\partial x} V(x,t) = -L \frac{\partial}{\partial t} I(x,t) - RI(x,t) \\ \frac{\partial}{\partial x} I(x,t) = -C \frac{\partial}{\partial t} V(x,t) - GV(x,t) \end{cases}, \tag{2.2}$$

except that now V and I are $n-$dimensional vectors containing the voltages and currents corresponding to each conductor; and L, R, C, and G are n by n constant matrices that contain the line parameters. These line parameter matrices, together with the terminal constraints, fully determine V and I.

As described in (Paul 1994; Paul 2007) and the references therein, physical considerations translate into particular properties of the line parameter matrices. These properties play an essential role in, for example, the possibility of decoupling the multiconductor transmission line system of equations and converting them into n uncoupled two-conductor line equations. Importantly, the level of difficulty in solving the multiconductor transmission line equations depends strongly on the underlying assumptions about the line, e.g., (1) a homogeneous or inhomogeneous medium surrounding the conductors; (2) a uniform or a nonuniform line; and (3) a lossless or a lossy line. For example, for lossless lines—i.e., r and g are zero in (2.1)—the equations reduce to:

$$\begin{cases} \frac{\partial}{\partial x} v(x,t) = -l \frac{\partial}{\partial t} i(x,t) \\ \frac{\partial}{\partial x} i(x,t) = -c \frac{\partial}{\partial t} v(x,t), \end{cases} \tag{2.3}$$

a hyperbolic system of partial differential equations. By algebraically decoupling the equations in (2.3), we get two

familiar wave equations in mathematical physics:

$$\begin{cases} \frac{\partial^2}{\partial t^2} v(x,t) = \frac{1}{lc} \frac{\partial^2}{\partial x^2} v(x,t) \\ \\ \frac{\partial^2}{\partial t^2} i(x,t) = \frac{1}{lc} \frac{\partial^2}{\partial x^2} i(x,t) \end{cases} \tag{2.4}$$

where the speed of the wave is $1/\sqrt{lc}$. By incorporating terminal conditions, explicit solutions can then be obtained. It is important to remember, however, that the lossless assumptions do not allow for modeling the dissipation and dispersion of the traveling waves in distribution lines.

Although we consider only uniform lines—where the conductor cross sections and the cross sections of any homogeneous surrounding media are constant along the line, and hence the per-unit-length parameters are independent of the line axis variable—it is not true that the line parameters can be considered constant; rather, they are functions of frequency, as shown in (Martí 1982), (Paul 1994), and (Antonini, Orlandi, and Pignari 2013). In fact, as a result of the skin effect, the resistance of the wires increases proportionally to the square root of the frequency. Also, a portion of the magnetic flux internal to the conductors gives rise to an internal inductance that decreases as the square root of the frequency. The effective conductivity of the dielectric surrounding the conductors also exhibits a frequency dependence; this is primarily a result of polarization loss. This adds another loss factor that—depending on the dielectric and the frequency range—might or might not be negligible (Antonini, Orlandi, and Pignari 2013). It is claimed (see, e.g., (Paul 1994)) that it is much easier to include these frequency-dependent per-unit-length parameters when the transmission line equations are derived in the frequency domain. These equations are:

$$\begin{cases} \frac{\partial}{\partial x} \hat{V}(x,\omega) = -\hat{Z}(\omega)\hat{I}(x,\omega) \\ \\ \frac{\partial}{\partial x} \hat{I}(x,\omega) = -\hat{Y}(\omega)\hat{V}(x,\omega) \end{cases} \tag{2.5}$$

where $\hat{Z}(\omega)$ and $\hat{Y}(\omega)$ are the impedance and admittance matrices defined in terms of the line parameters as:

$$\begin{cases} \hat{Z}(\omega) = R(\omega) + j\omega L(\omega) \\ \\ \hat{Y}(\omega) = G(\omega) + j\omega C(\omega) \end{cases} \tag{2.6}$$

It is not clear in the derivations, however, how high-frequency values impact the validity of (2.5) or the computation of the frequency-dependent line parameters. In future work, we plan to address this important issue by using our hardware and simulation experiments. Standard derivations of the line parameters can be found in (Dommel 1996) and (Paul 1994), but we have not yet found literature on fully validating the results of these derivations with field data from actual transmission lines. Note that the frequency dependence of the line parameters implies that (2.2) is no longer valid and should be replaced by appropriated integral convolutions between the line parameters with the current and the voltage.

Differentiating the top equation in (2.5) with respect to x and substituting the other, and vice versa, gives the uncoupled second-order differential equations:

$$\begin{cases} \frac{\partial^2}{\partial x^2} \hat{V}(x,\omega) = \hat{Z}(\omega)\hat{Y}(\omega)\hat{V}(x,\omega) \\ \\ \frac{\partial^2}{\partial x^2} \hat{I}(x,\omega) = \hat{Y}(\omega)\hat{Z}(\omega)\hat{I}(x,\omega) \end{cases} \tag{2.7}$$

which, together with terminal conditions, provide explicit frequency solutions to the problem (2.5) for two conductors. Appropriate approximations of these frequency domain solutions enable their semianalytical inversion to obtain the sought time-domain solutions (Martí 1981). Classically, this has included the use of numerical inverse Laplace transforms; however, there are well-known numerical issues with the inverse Laplace transform. For example, they have recently been addressed in (Tavighi et al. 2018).

For the multiconductor equations, the standard approach is to assume that there exists a change in variables to diagonalize $\hat{Z}(\omega)\hat{Y}(\omega)$ (or, equivalently, $\hat{Y}(\omega)\hat{Z}(\omega)$) so that the new variables, (2.7), are decoupled; in this way, the

problem is reduced to several two-conductor cases. The matrix that provides the change in variables is referred to as a modal transformation because the important information in the original matrix is now encapsulated in its eigenvalues (modes)—which are, of course, frequency dependent.

Thus, assume that the matrix product $\hat{Z}(\omega)\hat{Y}(\omega)$ can be diagonalized—that is, there is an invertible (modal transformation) matrix $T = T(\omega)$, such that:

$$\hat{Z}(\omega)\hat{Y}(\omega) = T\hat{\gamma}^2 T^{-1} \tag{2.8}$$

where $\hat{\gamma} = \hat{\gamma}(\omega)$ is a diagonal matrix of diagonal entries $\hat{\gamma} = (\hat{\gamma}_1, \hat{\gamma}_2, \ldots, \hat{\gamma}_n)$, which are called propagation constants (this name stems from their role in Eq. (2.11)); therefore, the propagation constants are square roots of the eigenvalues of $\hat{Z}(\omega)\hat{Y}(\omega)$.

From the physical considerations, we know that both $\hat{Z}(\omega)$ and $\hat{Y}(\omega)$ are symmetric matrices; hence, transposing (2.8), we obtain $\hat{Y}(\omega)\hat{Z}(\omega) = T^{-t}\hat{\gamma}^2 T^t$. We conclude that T^{-t} (the transposed inverse of T) is the transformation matrix that diagonalizes $\hat{Y}(\omega)\hat{Z}(\omega)$. Clearly, the eigenvalues of $\hat{Z}(\omega)\hat{Y}(\omega)$ coincide with those of $\hat{Y}(\omega)\hat{Z}(\omega)$.

Next, by defining the *mode quantities* $\hat{V}_m$ and $\hat{I}_m$:

$$\begin{cases} \hat{V}_m(x,\omega) = T^{-1}\hat{V}(x,\omega) \\ \\ \hat{I}_m(x,\omega) = T^t\hat{I}(x,\omega) \end{cases} \tag{2.9}$$

we obtain the decoupled system (one independent equation for each voltage and current):

$$\begin{cases} \frac{\partial^2}{\partial x^2}\hat{V}_m(x,\omega) = \hat{\gamma}^2\hat{V}_m(x,\omega) \\ \\ \frac{\partial^2}{\partial x^2}\hat{I}_m(x,\omega) = \hat{\gamma}^2\hat{I}_m(x,\omega) \end{cases} \tag{2.10}$$

from which we obtain the general solution:

$$\begin{cases} \hat{V}_m(x,\omega) = e^{-\hat{\gamma}x}\hat{V}_m^+(\omega) + e^{\hat{\gamma}x}\hat{V}_m^-(\omega) \\ \\ \hat{I}_m(x,\omega) = e^{-\hat{\gamma}x}\hat{I}_m^+(\omega) - e^{\hat{\gamma}x}\hat{I}_m^-(\omega) \end{cases} \tag{2.11}$$

where the matrix exponential $e^{-\hat{\gamma}x}$ is a diagonal matrix, and $\hat{V}_m^{\pm}(\omega)$ and $\hat{I}_m^{\pm}(\omega)$ are four $n \times 1$ (as yet) undetermined vectors. Using (2.5) and (2.9), the vectors $\hat{V}_m^{\pm}(\omega)$ can be written in terms of $\hat{I}_m^{\pm}(\omega)$, leaving the correct number of undetermined constants (that is, $2n$) that can be derived from the terminal conditions. Finally, using (2.9) once more, we obtain the solutions to (2.5); however, the complicated dependence on frequency prevents us from deriving useful explicit expressions for the time-domain functions $V(x,t)$ and $I(x,t)$. Different techniques have been employed to provide approximate or numerical solutions as in (Paul 2007), but all of them deal with the possibility of numerical issues related to multiple eigenvalues or nonsmooth frequency changes in the modal transformation. Moreover, stability problems were thought to be caused by inaccuracies in the modal domain representation, so much of the effort went into the development of more accurate fitting techniques. More recently, the authors of (Gustavsen and Semlyen 1998c) showed that although the phase domain is inherently stable, its associated modal domain might be inherently unstable regardless of the fitting.

Importantly, even if it is correct to assume that $\hat{Z}(\omega)\hat{Y}(\omega)$ can be diagonalized, the entries of the modal transformation are frequency dependent, which further complicates the derivation of the sought time-domain solutions (Paul 2007). Although a variety of approaches had been developed to ignore this frequency dependence and simply use a constant modal transformation, it has been observed, see (Gustavsen and Semlyen 1998c), that the modal transformation could be strongly frequency dependent; in this case, it becomes impossible to approximate it by a constant matrix. As noted in (Paul 1996), the use of constant modal transformations "has led to considerable confusion," and for this reason we show in Section 2.2.1 how to avoid assuming that the product $\hat{Z}(\omega)\hat{Y}(\omega)$ is diagonalizable and how to recover the standard results if that property holds.

Next, we describe the most common line models and how they treat modal transformations.

2.1.1 The Problem of Incorporating Frequency Dependence Into Line Models

To provide a brief chronological overview of the different developments and challenges in selecting and implementing EMTP algorithms focusing on modeling frequency-dependent components, we mostly follow the review presented in a recent Ph.D. thesis (Tavighi 2017). Most authors agree that the most useful frequency-dependent transmission line and underground cable models implemented in EMTP are the frequency-dependent line (FD-Line) (Martí 1981; Martí 1982), the LMARTI model (Martí 1988), and the Universal Line Model (ULM) (Morched, Gustavsen, and Tartibi 1999). To avoid the numerically challenging inversion of the frequency-domain expressions, these three models approximate the frequency dependence of the line or cable wave functions with special rational function approximations, such as Bode's asymptotic fitting (Martí 1981) and vector fitting (Gustavsen and Semlyen 1999). The fitted rational functions are then converted into the time domain as part of the algorithms employed to derive the time-domain solution. We now briefly describe these three models:

FDLINE Model

One of the first frequency-dependent multiconductor line models was proposed in 1970 by Budner (Budner 1970). He introduced weighting functions to model the frequency dependence of the line characteristic admittance and wave propagation functions; however, the weighting functions in this model are highly oscillatory and difficult to evaluate with accuracy (Martí 1981).

In 1972, Snelson (Snelson 1972) introduced an analogous variable change to relate currents and voltages in the time domain. This idea was further developed by Meyer and Dommel in 1974 (Meyer and Dommel 1974) and resulted in forward and backward traveling functions from the weighted past history of the currents and voltages at both line ends using a convolution integral. Although this formulation gave reliable results in many cases of transient studies (Martí 1981), the time-domain solution required computationally expensive evaluation of convolution integrals at each time step and provided a less accurate response at low frequencies, including the nominal 60-Hz steady-state frequency (Martí 1981). To address these issues, in 1975 Semlyen and Dabuleanu introduced (Semlyen and Dabuleanu 1975) an efficient formulation to synthesize the line functions with a low-order rational function approximation using complex-valued parameters; however, numerical oscillations were introduced in the response of the line model, leading to numerical instability.

In in 1981–1982, J. Martí (Martí 1981; Martí 1982) introduced the FD-Line model to simplify frequency-dependence modeling by fitting the amplitude of the line functions with high-order Bode's asymptotic fitting rational approximations using negative poles and zeroes to guarantee minimum-phase-shift rational functions and match the causality of the physical system; however, FD-Line makes an important simplification that is not always valid: it replaces the frequency-dependent modal transformation matrices (of the multiconductor transmission line) by a constant transformation corresponding to a single representative frequency to be used for all other frequencies; moreover, only the real part of the constructed transformation matrix is used (its imaginary part is discarded). Even though FD-Line has been widely adopted, the use of a single representative real-valued transformation matrix to convert between modal and phase quantities can severely limit the accuracy of the approach by failing to capture a potentially large frequency range. In particular, this limitation manifests in the modeling of underground cables because in this case the elements of the modal transformation matrix can change quite drastically with frequency. For other cases, possible improvements have been suggested. For example, Gustavsen (Gustavsen 2012) showed that the accuracy of FD-Line in two parallel overhead lines can be improved by modeling each line by an FD-Line and then adding the mutual coupling between the independent FD-Lines using rational functions; however the proposed model seems to be computationally expensive, particularly if the upper bandwidth surpasses 100 kHz.

LMARTI Line Model

To address the accuracy problem in modeling underground cables, in 1988 L. Martí (Martí 1988) introduced a new model that considers the frequency dependence of the cable parameters by using modal transformation matrices that are frequency dependent. Incorporating this dependence is absolutely necessary because the conductors are very close to each other and to ground, and consequently the transformation matrices become strongly frequency dependent. In this approach, transformation matrices are synthesized via Bode's asymptotic fitting rational approximations with real negative poles, and it was shown that the method works well for underground cables (Martí, Brierley, and Grainger

1995). Nevertheless, fitting the transformation matrices with minimum-phase rational functions proved to be a challenging task, and the numerical difficulties of the direct use of the frequency-dependent transformations became a new obstacle. In particular, some entries of the transformation matrix could not be satisfactorily approximated, and there were also issues with modes switching along the frequency range (Brandao Faria and Borges da Silva 1990).

Universal Line Model

The difficulties involved in the modal domain line models led to the development of alternative line models that avoid transformation matrices by working directly in phase instead of modal coordinates. Using idempotent theory (Cullen 2012), in 1993 Wedepohl (Wedepohl 1993) synthesized the propagation function of transmission lines in phase coordinates. The idempotents are slightly better behaved functions than the eigenvectors of the modal transformation matrices, but they also suffer from issues related to their frequency dependence. Idempotency-based line models for the EMTP were first introduced in 1995 by Castellanos, J. Martí, and Marcano (see (Castellanos, Martí, and Marcano 1997)) and further developed in (Marcano 1996) and (Marcano and Martí 1997). In these models, accuracy was sacrificed to use only minimum-phase functions for asymmetrical line configurations. In 1998, Gustavsen and Semlyen relaxed the requirement of the minimum phase in the synthesis of the idempotent coefficients to gain accuracy (Gustavsen and Semlyen 1998b, 1998c, 1998a), and by 1999 this work evolved into the ULM (Morched, Gustavsen, and Tartibi 1999), a widely used approach that relies on vector-fitting rational approximation (Gustavsen and Semlyen 1999; Gustavsen 2006; Gustavsen and Nordstrom 2008). Issues related to the implementation of ULM, such as numerical instability, had been addressed in, e.g., (Kocar, Mahseredjian, and Olivier 2010; Kocar and Mahseredjian 2015; Gustavsen 2013). From the point of view of computation, however, ULM is considerably more expensive than FD-Line, which is a critical consideration in real-time simulators (see, e.g., operation counts on Eq. (2.31) and Eq. (2.35) in (Tavighi 2017)). Although efficiency improvements have been recently reported (Cabral et al. 2016), we believe that the key to improving the performance of ULM is to replace vector fitting by a more accurate and faster algorithm, as explained in Section 2.2.2.

2.2 Recommended Improvements to Modeling and Software Simulation

As mentioned in the previous section, existing models assume that there is an unavoidable trade-off between slower but more accurate and general algorithms (such as ULM) and much faster algorithms (such as FD-Line) that require additional assumptions and provide limited accuracy; however, this trade-off is not a necessity. We identified several modeling and algorithmic modifications that can simplify, accelerate, and provide comparable or improved accuracy than existing approaches. In the following sections, we list those that we believe can have a stronger impact, but we note that other improvements are necessary. For example, EMTPs do not scale well when large numbers of components are added to systems; however, the problem formulation presents the opportunity to inject existing scalable algorithms into EMTPs. Examples of existing scalable software that might be applicable to EMT computations include KLU (Davis and Palamadai Natarajan 2010), a sparse direct solver specifically designed for circuit problems, and PETSc (Abhyankar et al. 2018), a more general tool kit designed for scalable scientific computations. There is also recent work on the application of graphics processing units to EMT calculations (Zhou and Dinavahi 2014) that merits detailed examination.

2.2.1 A General Approach to Frequency-Domain Rational Approximations

In this section, we show how to avoid simplifying assumptions in the line models without sacrificing speed or accuracy. Because we are interested in incorporating a large range of possible frequencies, our approach is similar to the ULM (Morched, Gustavsen, and Tartibi 1999), but, in contrast, we avoid assuming properties of the impedance and admittance matrices.

In frequency-domain models, solutions are first explicitly obtained in the frequency domain, and then voltages and currents are transformed back to the time domain. Numerical transforms are not straightforward and introduce a variety of issues (see, e.g., (Nagaoka and Ametani 1988; Gustavsen 2005; Tavighi et al. 2018)). Alternatively, relevant matrix functions can be approximated via rational functions (with a common set of poles), leading to explicit exponential representations (with a common set of exponents) in the time domain. In this way, the necessary convolutions in the time domain can be efficiently performed by exploiting properties of exponential functions (see, e.g., (Beylkin and Monzón 2005, Section 5.3)).

An important aspect of our approach is to replace existing rational or exponential approximations used through existing EMTP software by recent nonlinear methods for the fast and accurate computation of optimal rational or exponential approximation of signals and functions ((Beylkin and Monzón 2002), (Beylkin and Monzón 2005), (Beylkin and Monzón 2009), (Beylkin and Monzón 2010)). These methods are optimal because they minimize the required number of approximation terms for any user-selected target accuracy. Members of our team have been instrumental in the development and application of these methods, and we are confident that improvements can be achieved by employing this powerful methodology ((Beylkin, Kurcz, and Monzón 2008), (Beylkin, Kurcz, and Monzón 2007), (Beylkin, Kurcz, and Monzón 2009), (Beylkin, Lewis, and Monzón 2012), (Beylkin and Monzón 2016), (Reynolds, Beylkin, and Monzón 2013), (Yarman, Lewis, and Monzon 2016), (Yarman et al. 2013), (Damle et al. 2013), (Lewis, Beylkin, and Monzón 2013), (Haut, Beylkin, and Monzón 2013), (Beylkin et al. 2012), (Castro et al. 2018)). For the rational approximation of multiple functions using a common set of poles, we plan to replace vector fitting by the modified multi-input adaptive Antoulas-Anderson (MIAAA) algorithm (see Section 2.2.4), which is an extension of very recent results on rational approximations (Nakatsukasa, Sète, and Trefethen 2018).

In practice, it is very useful to consider equations in the $s-$domain (which is unfortunately referred to in the literature as a Laplace-domain approach). We can arrive to them if, in the equations in Section 2.1, we substitute $s = i\omega$ and denote this substitution in the functions involved by the use of the variable s instead of the frequency ω.

Hence, in frequency domain, the multiconductor transmission line equations for $n+1$ conductors can be written as

$$\frac{\partial}{\partial x}\begin{bmatrix} \hat{V}(x,s) \\ \hat{I}(x,s) \end{bmatrix} = -\begin{bmatrix} 0 & \widetilde{Z}(s) \\ \widetilde{Y}(s) & 0 \end{bmatrix}\begin{bmatrix} \hat{V}(x,s) \\ \hat{I}(x,s) \end{bmatrix}, \tag{2.12}$$

where $\hat{V}$ is the voltage vector, $\hat{I}$ is the current vector, and $\widetilde{Z}(s)$ and $\widetilde{Y}(s)$ are the $n \times n$ impedance and admittance matrices containing the frequency-dependent line parameters. The $\widetilde{Z}(s)$ and $\widetilde{Y}(s)$ matrices are defined as

$$\begin{cases} \widetilde{Z}(s) & = R(s) + sL(s) \\ \\ \widetilde{Y}(s) & = G(s) + sC(s), \end{cases} \tag{2.13}$$

where the line parameters are given by the inductance, L; resistance, R; capacitance, C; and conductance G. Note that these parameters, such as $\widetilde{Z}(s)$, might grow as $\sqrt{s}$ for large s, an important consideration for choosing a functional representation, as will be shown later.

The goal is to solve (2.12) for the temporal voltages and currents, $V(x,t)$ and $I(x,t)$, for some given line parameters and boundary conditions at $x = 0$, $V(0,t)$ and $I(0,t)$. Here, $t \geq 0$ is time and, x represents the position on the line.

The solution of the system (2.12) can be written as:

$$\begin{bmatrix} \hat{V}(x,s) \\ \hat{I}(x,s) \end{bmatrix} = \hat{\Phi}(x,s)\begin{bmatrix} \hat{V}(0,s) \\ \hat{I}(0,s) \end{bmatrix}, \tag{2.14}$$

where:

$$\hat{\Phi}(x,s) = \exp\left(-x\begin{bmatrix} 0 & \widetilde{Z}(s) \\ \widetilde{Y}(s) & 0 \end{bmatrix}\right). \tag{2.15}$$

Using Remark 1, $\hat{\Phi}(x,s)$ can be computed explicitly in terms of hyperbolic functions applied to the matrix products $\widetilde{Y}\widetilde{Z}$ and $\widetilde{Z}\widetilde{Y}$. When these matrix products are diagonalizable, we recover the formula obtained in some ULM approaches; and for the two conductor cases, we recover equations (1.34)–(1.35) in (Martí 1981).

To approximate $\hat{\Phi}(x,s)$ by rational functions, we follow previous work involving nonlinear approximations (see (Haut, Beylkin, and Monzón 2013; Beylkin, Monzón, and Satkauskas 2018, 2019)) and introduce a particular functional form that is maintained in solving equations. We use two different representations, one for parameters of the system and

another for the solutions of the governing equations. For parameters of the system, we choose the functional form for each single function to be:

$$s\sum_{k=1}^{K}\frac{c_k}{s-p_k} \tag{2.16}$$

because it allows us to account for the growth of the frequency dependent-parameters caused by the skin effect, e.g., $\widetilde{Z}(s)=\mathscr{O}(\sqrt{s})$. The sum in (2.16) involves residues, c_k, and a set of distinct poles, p_k. In this form, the sum in (2.16) decays to zero as $s\to\infty$. On the other hand, the initial conditions and the solutions are represented as proper rational functions.

To explain our approach, first fix x in (2.14) and assume that we already approximated each entry of $\widetilde{Z}(s)$, $\widetilde{Y}(s)$ by functions of the form (2.16). The poles are obtained via a combination of optimal and suboptimal algorithms that fit the given functions within a user-specified error and with an (almost) minimal number of poles. Note that once $\widetilde{Z}(s)$ and $\widetilde{Y}(s)$ are approximated in this form, the Caley-Hamilton theorem shows that $\hat{\Phi}(x,s)$ can be written in the same form, where the set of poles remains unchanged.

The critical assumption of diagonalization can now be avoided in computing (2.15). In fact, by using the scaling and squaring method for computing matrix exponentials (see, e.g., (Golub and Loan 1996, Algorithm 11.3.1)), we can accommodate matrices that cannot be diagonalized.

In practical computations, multiplications of matrices with entries of the form (2.16) can be performed rapidly by simply updating the residues of the input fractions. More explicitly, each product of two factors with different poles leads to:

$$s\frac{a}{s-\alpha}\cdot s\frac{b}{s-\beta}=s\left(\frac{c_1}{s-\alpha}-\frac{c_2}{s-\beta}\right)$$

where $c_1=\frac{ab\alpha}{\alpha-\beta}$ and $c_2=\frac{ab\beta}{\alpha-\beta}$. For coincident poles, we can use the approach in (Haut, Beylkin, and Monzón 2013, p. 89) to replace a pole of multiplicity two by several distinct poles of multiplicity one; thus, the form (2.16) is maintained under multiplication and (clearly) under linear combinations. The only remaining issue is that the number of terms in the sum will increase: this is the reason for using optimal reduction algorithms to control the number of terms in the sum.

Using this approach, we compute the exponential $\hat{\Phi}(x,s)$ so that each entry will be in the form (2.16), and then we perform the product in (2.14). It is important that entries of the vector $\begin{bmatrix}\hat{V}(0,s)\\ \hat{I}(0,s)\end{bmatrix}$ are approximated by proper rational functions, leading to each entry of $\begin{bmatrix}\hat{V}(x,s)\\ \hat{I}(x,s)\end{bmatrix}$ to also be described as a proper rational function. For this case, we have one multiplicand with a factor s coming from the representation of $\hat{\Phi}(x,s)$ and another factor without it; we obtain:

$$s\frac{a}{s-\alpha}\cdot\frac{b}{s-\beta}=ab\left(\frac{c_1}{s-\alpha}-\frac{c_2}{s-\beta}\right),$$

where $c_1=\alpha/(\alpha-\beta)$ and $c_2=\beta/(\alpha-\beta)$, which is also of the desired form.

Remark 1. For square matrices A,B, we show how to derive an explicit expression for $e^{\begin{bmatrix}0 & A\\ B & 0\end{bmatrix}}$. Expanding the Taylor series of the exponential function into even and odd powers:

$$e^{\begin{bmatrix}0 & A\\ B & 0\end{bmatrix}}=\sum_{n=0}^{\infty}\frac{1}{(2n)!}\begin{bmatrix}(AB)^n & 0\\ 0 & (BA)^n\end{bmatrix} \tag{2.17}$$

$$+\sum_{n=0}^{\infty}\frac{1}{(2n+1)!}\begin{bmatrix}0 & A\\ B & 0\end{bmatrix}\begin{bmatrix}(AB)^n & 0\\ 0 & (BA)^n\end{bmatrix} \tag{2.18}$$

$$=\begin{bmatrix}f(AB) & A\,g(BA)\\ B\,g(AB) & f(BA)\end{bmatrix}, \tag{2.19}$$

where the two auxiliary functions f and g are defined as:

$$f(z) = \cosh\sqrt{z} = \sum_{n=0}^{\infty} \frac{z^n}{(2n)!}$$

and:

$$g(z) = \left(\sqrt{z}\right)^{-1} \sinh\sqrt{z} = \sum_{n=0}^{\infty} \frac{z^n}{(2n+1)!}.$$

Because f, g are entire functions, using the Jordan form of AB and BA, we can explicitly compute the entries of the matrices in (2.17). These entries correspond to values of f, g and higher derivatives (the number of derivatives depends on the size of the Jordan blocks) evaluated at the eigenvalues of AB or BA.

2.2.2 Software Development

Based on our study of EMTP theory and implementations, we concluded that the best approach to modeling distribution lines with parameters that depend on frequencies over a wide bandwidth is to use the ULM. Specifically, ULM provides more accurate solutions over a broad range of frequencies, and thus it is the method of choice for simulations that involve high-frequency signatures. As discussed in Section 2.1.1, however, deficiencies on the ULM approach have a strong impact on simulations that are aggravated for larger and complex distribution systems. For this reason, one task of the software team has been to analyze the specific algorithmic issues that impact the accuracy and performance of ULM.

One key algorithm behind the ULM approach is to represent the frequency dependence of the line's wave matrix functions via special rational function approximations—namely, each entry of the matrix is approximated by rational functions that share a common set of poles. This property permits to (analytically) convert the corresponding solutions into the time domain. The fitted matrices become linear combinations of exponentials that share a common set of exponents. This, in turn, permits the efficient recursive computations of the resulting time-domain integrals. Considering that the number of poles used in the rational approximations directly translates into the number of exponentials used in the time-domain computations, it is of great importance to minimize (for a target accuracy) the number of common poles in the rational approximations. This minimization results in a strong reduction in the computational cost as well as in improving stability. We refer to obtaining a minimal (or close to minimal) number of poles as obtaining an optimal (or close to optimal) rational approximation.

Although there are excellent algorithms to obtain the optimal (or close to optimal) rational approximation of a single function, the multi-input/multi-output (MIMO) problem involving several functions presents important challenges, and we are not aware of any optimization algorithm for this case. Even finding close to optimal solutions for the MIMO problem via robust and efficient algorithms is still an active area of research in applied mathematics and engineering. In the engineering literature, the most popular approach for the MIMO problem is the (iterative) vector-fitting algorithm (Gustavsen and Semlyen 1999), including several improvements introduced to it over time (see (Gustavsen 2006), (Morales-Rodriguez et al. 2019)). Although vector fitting might do a reasonable or even a good job on a variety of problems, it has several well-known limitations (such as indeterminant convergence or convergence to low-accuracy solution) that we investigated and documented in this report. The deficiencies of vector fitting led us to consider other possible approaches (see (Morales Rodriguez 2019)) and eventually to develop an alternative algorithm (see Section 2.2.4) that does not suffer from vector-fitting drawbacks. In particular, for problems where vector fitting can provide an accurate solution, we show that our algorithm yields a more efficient (fewer poles) solution with the consequent direct improvement on the overall speed of the approach. For accurate but computationally expensive algorithms such as Rational Krylov Fitting (RKFIT) (Berljafa and Güttel 2017), our initial tests show that our approach is considerably faster. Our preliminary results have already been accepted for publication in (Monzón et al. 2020).

2.2.3 Software Development: Python Electromagnetic Transients

To analyze and test alternative approaches for EMTP simulations, we developed an object-oriented and lightweight EMT-like simulation software named PyEMT for this project. The goal of PyEMT is not to replace existing EMT programs but rather to provide a platform for investigating and developing potential improvements in EMT modeling. This objective is realized in PyEMT through an open-source modular design. The design lets researchers control every

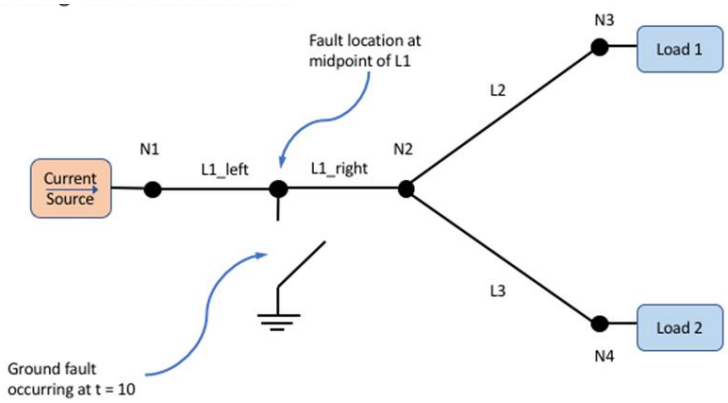

Figure 1. Simplified test network used to simulate traveling waves emerging from a ground fault.

step of their EMT computations while providing the ability to insert modules of code to modify whatever part of the program they desire. During our research, we have found it advantageous to be able to modify only certain parts of the code as a way to isolate its impact on the overall program. For example, users can modify only the line-modeling code to more effectively explore the phenomenon of EMT, experiment with scalable linear system solvers to speed up EMT computations, or to insert higher fidelity models where needed to describe components of their test system. This ability to easily swap out components of code comes from Python, which is the programming language the tool is written in. By using an object-oriented approach to develop PyEMT, the software team researchers enabled not only an object-oriented approach to building networks but also a modular framework within which we can replace portions of the code to test higher fidelity and/or faster components. Because Python can easily integrate other software, PyEMT enables users to experiment with software written in a variety of languages while using different types of hardware (e.g., high-performance computing, graphics processing unit). We believe that the functionality of Python will enable us—and other researchers—to explore new components in EMT programs in greater detail and contribute to its development.

Figure 1 depicts the test network used to create this simulation. The network comprises four normal nodes—N1, N2, N2, and N4; a fault node; fault; and three two-phase lines—L1, L2, and L3. A current source injects current into the network at N1. Attached to N3 and N4 are two constant impedance loads.

2.2.4 Vector Fitting and Adaptive Antoulas-Anderson Algorithms for Rational Approximations

In this subsection, we provide an overview of the mathematics behind the vector fitting algorithm and Adaptive Antoulas-Anderson algorithm (AAA) and comment on the distinctions between the two. More details can be found in the team's analysis in (Monzón et al. 2020) and the references therein.

Vector Fitting

The vector-fitting methodology can be understood as a reformulation of the Sanathanan-Koerner iterative algorithm for polynomial approximation. Although the Sanathanan-Koerner algorithm does not find the optimal least-squares solution to the fitting problem, it remains stable during successive iterations (see (Hendrickx and Dhaene 2006) and references therein). In contrast with the Sanathanan-Koerner algorithm, vector fitting relies on rational function approximations instead of polynomials, which (theoretically) guarantees more succinct representations—that is, it requires less representation parameters than its polynomial counterparts. For the selection of poles, vector fitting follows the strategy of iteratively relocating the poles to improved locations.

For ease of understanding, we first describe how the vector-fitting algorithm finds the fit of a single function, f. The goal of vector fitting is to fit a set of sample values of f, $\{f(s_n)\}_{n=1}^{N}$, by $\{r(s_n)\}_{n=1}^{N}$, where r is the rational function

to be found described in partial fraction form:

$$r(s) = \sum_{m=1}^{M} \frac{r_m}{s - p_m} + d_0 + d_1 s. \tag{2.20}$$

The poles, p_m; residues, r_m; and constants, d_0 and d_1, are found in the following way. A set of initial pole guesses, $\{z_n\}_{1 \le n \le N}$, is provided by the user, and the corresponding residues and constants are computed via least squares. The procedure is iterated to obtain updated poles (pole relocation) until some convergence criteria are met; the resulting set is used as the approximation of the target poles, p_m.

The algorithm is easily generalized to the multifunction case, which takes as input the samples of several functions and finds partial fraction approximations of all of them using a common set of poles. For practical use, it is important to keep the number of common poles (and hence the number of parameters describing the approximations) as small as possible for a desired approximation accuracy. Because of the absence of optimization with respect to the number of poles, we show that vector fitting generates far from optimal rational approximations.

Single-Input AAA Algorithm

The adaptive Antoulas-Anderson (AAA) algorithm was formally introduced by Y. Nakatsukasa and collaborators in (Nakatsukasa, Sète, and Trefethen 2018), but it had been previously used as part of Chebfun [2], an open-source software system written in MATLAB. The AAA algorithm is very fast, accurate, robust, and easy to use. It approximates a single function f by using the barycentric interpolation formula that, given samples $f(z_n)$, defines a rational function B_f as:

$$B_f = \frac{\sum_{n=1}^{N} \frac{w_n f(z_n)}{s - z_n}}{\sum_{n=1}^{N} \frac{w_n}{s - z_n}}, \tag{2.21}$$

where w_n is an (arbitrary) set of nonzero weights, and the distinct points z_n are referred to as support points. The function B_f interpolates f at the points $\{z_n\}_{n=1}^{N}$—that is,

$$B_f(z_n) = f(z_n); n = 1, \ldots, N. \tag{2.22}$$

Therefore, in the AAA algorithm, rational functions are represented in barycentric form with interpolation at certain support points selected from an input set provided by the user. This set typically includes the sample points for which sample values of f are available or computed. The algorithm grows the approximation degree one by one, selecting support points in a systematic greedy fashion to avoid numerical instabilities. Once the final barycentric approximation is determined, that representation is converted into partial fraction form, which, we noticed, could be a delicate step that requires carefully designed special algorithms to prevent accuracy loss.

Comparison Of Vector Fitting and Adaptive Antoulas-Anderson

AAA is related to vector fitting in that they are both iterative algorithms that solve a least-squares problem at each step of the iteration, and after convergence both algorithms find the zeros of a rational function written in partial fractions form; thus, both algorithms rely on the iterative solution of linear systems followed by a nonlinear algorithm to determine the desired poles of the solution. Once poles are obtained, residues of the final rational approximation can be obtained by a linear procedure.

Comparison of vector-fitting and AAA approaches: Some disadvantages of vector fitting with respect to AAA:

- The number of poles is fixed in advance. (AAA finds this number algorithmically.)
- Estimates of poles are needed to start the algorithm. (AAA requires no estimates.)
- Results can be far from optimal. (AAA gives results very close to optimal.)
- Numerical issues might prevent convergence or limit the accuracy of the solutions.

[2] https://www.chebfun.org/

Some advantages of vector fitting with respect to AAA:

- It applies to vector functions. (The original AAA is limited to a single function.)
- It has been used extensively and has well understood computational formulations. (AAA is quite new.)

We note that the comparisons between both algorithms are not straightforward. In (Nakatsukasa, Sète, and Trefethen 2018), the authors comment that "It was our intention to compare the performance of AAA against that of vector fitting, but our experiments with vector fitting failed to give satisfactory convergence." In our opinion, this appears to be related to how initial guesses of pole locations were chosen. Considering that the main disadvantage of AAA is that it is limited to single-input problems, the software team designed and tested a new algorithm (named MIAAA) that extends AAA to the multi-input setting while keeping the main advantages of the standard AAA algorithm. Our preliminary results, described in the next section, are very encouraging (Monzón et al. 2020), and we plan to keep developing and improving our current version.

2.2.5 Computational Examples: Comparing the Performance of Vector Fitting and MIAAA Algorithms

To compare the performance of MIAAA with vector fitting, we consider two examples from the literature and as discussed in our analysis paper (Monzón et al. 2020).

First example: A problem with multiple resonance peaks

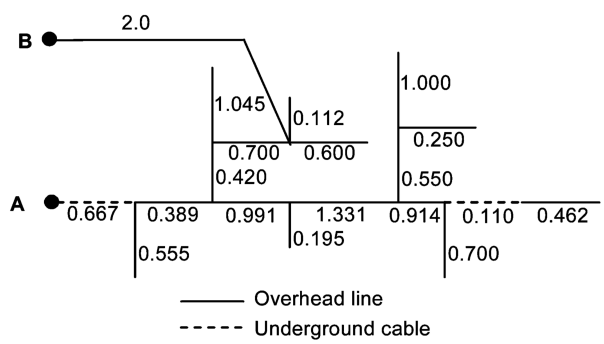

Figure 2. Power system diagram for the admittance matrix example in (Deschrijver, Gustavsen, and Dhaene 2007; Morales-Rodriguez et al. 2019). Numbers indicate lengths of lines in kilometers.

This standard test problem is presented in several publications, such as (Gustavsen 2008, Example 4a), (Deschrijver, Gustavsen, and Dhaene 2007), and (Morales-Rodriguez et al. 2019, Section III.D). A frequency dependent network equivalent (FDNE) approximation is performed on a single column of a 6-by-6 terminal admittance matrix of a power distribution system. The system has two three-phase buses as terminals, denoted as A and B in Figure 2; and the admittance matrix to be approximated has been sampled in the frequency range from 10 Hz to 100 kHz. To illustrate the results, the first two entries of the admittance matrix, $f(1)$ and $f(2)$, and their approximations using MIAAA and vector fitting are displayed in Figure 3, and the fitting errors of both methods are displayed in Figure 4. We observe that the MIAAA approximation error is always less than the normalized target accuracy 10^{-6} and fits the linear section of the function with error close to double precision; in contrast, vector fitting performs significantly worse. Importantly, MIAAA also provides a better approximation order because it requires only 36 common poles to reach the target accuracy—in contrast with vector fitting, which requires 50 poles. Although MIAAA was also faster than vector fitting, we do not provide speed comparisons because additional work is necessary for a more thorough comparison, and for the intended applications, the final number of poles used in the approximation is the dominant factor in running time and not the running time of vector fitting or MIAAA.

In Table 1, we report the fitting error on the 6 functions being approximated, computed using the metrics:

$$\varepsilon_{RMS} = \sqrt{\sum_{n=1}^{N}\sum_{k=1}^{K} |\varphi_k(z_n) - \phi_k(z_n)|^2/(N \cdot K)}, \tag{2.23}$$

$$\varepsilon_{relative} = \sum_{n=1}^{N}\sum_{k=1}^{K} \left| \frac{\varphi_k(z_n) - \phi_k(z_n)}{\varphi_k(z_n)} \times 100 \right| /(N \cdot K), \tag{2.24}$$

where ϕ_k is the MIAAA or VF approximation of the kth input function φ_k.

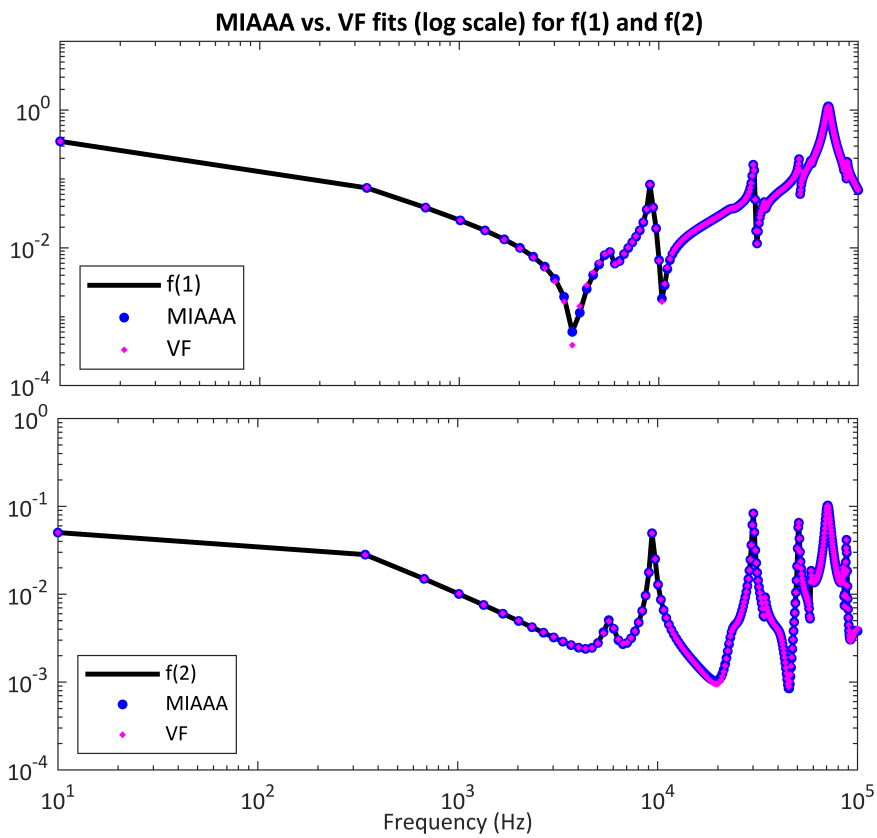

Figure 3. Comparing vector fitting and MIAAA approximations of the admittance matrix example in (Gustavsen 2008; Deschrijver, Gustavsen, and Dhaene 2007; Morales-Rodriguez et al. 2019). We display results for two entries, $f(1)$, top, and $f(2)$, bottom, as functions of frequency. The units for the Y-axis is normalized per unit admittance.

Table 1. Relative and RMS Errors for Vector Fitting and MIAAA Approximations of Functions $f(1), \ldots, f(6)$.

Technique	Order	ε_{RMS}	$\varepsilon_{relative}$
VF	50	1.563×10^{-4}	2.556
MIAAA	36	6.159×10^{-8}	2.702×10^{-3}

Remark: Observations on Carson's formula

Because the inputs for vector fitting and MIAAA rely on accurate functional valued inputs, it is essential to get the earth-return impedance in overhead lines correct. The canonical set of equations used to model this phenomenon are Carson's equations; however, the derivation of these equations (Carson 1926) relies heavily on the transverse electromagnetic assumption for electromagnetic wave propagation. Requiring the transverse electromagnetic assumption

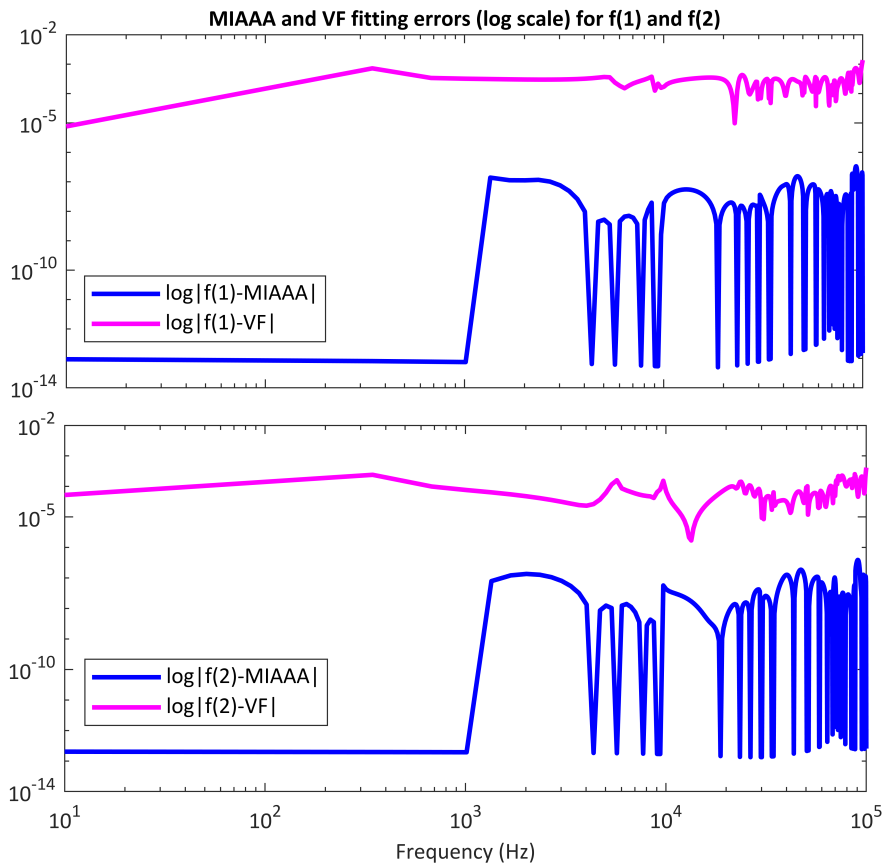

Figure 4. Comparing vector fitting and MIAAA fitting errors for the two functions shown in Figure 3. The MIAAA errors correspond to the final partial fraction approximations, not the intermediate barycentric approximations.

presents a problem when using transient phenomena for fault detection on distribution systems: we are interested in measuring phenomena with much higher frequencies than the steady-state operating frequency. At such high frequencies, it is unclear if the transverse electromagnetic assumption holds; thus, more investigation is required to ascertain if a different model is needed. In our interactions with EMTP software developers, we have learned that they have similar concerns and are currently investigating alternatives.

Second example: An admittance matrix of a simple pi-circuit

This example is taken from (Morales-Rodriguez et al. 2019, Section III.C) with the goal of illustrating the improvement on accuracy as we increase the order of the approximation. We consider the 2-by-2 symmetric admittance matrix Y of a simple pi-circuit, of entries (admittances of the circuit elements of the pi-model) given by:

$$Y_{11} = Y_a + Y_b, \quad Y_{21} = Y_{12} = -Y_a, \quad Y_{22} = Y_a + Y_c, \tag{2.25}$$

where

$$Y_a(s) = \frac{2}{s+5} + \frac{20 \pm 50j}{s+30 \mp 1000j} + 0.4, \tag{2.26}$$

$$Y_b(s) = \frac{6}{s+12} + \frac{17 \pm 30j}{s+35 \mp 3000j} + 0.2, \tag{2.27}$$

$$Y_c(s) = \frac{4}{s+10} + \frac{12 \pm 24j}{s+15 \mp 5500j} + 0.3. \tag{2.28}$$

Table 2. Comparison of vector-fitting and MIAAA techniques for fitting the 2×2 admittance matrix given by equations (2.25)–(2.28)

Technique	Order	ε_{RMS}	$\varepsilon_{relative}$
VF	7	2.20×10^{-3}	8.33×10^{-2}
MIAAA		2.18×10^{-4}	3.24×10^{-2}
VF	8	2.13×10^{-4}	1.00×10^{-2}
MIAAA		1.63×10^{-5}	1.97×10^{-3}
VF	9	5.10×10^{-15}	2.69×10^{-13}
MIAAA		3.75×10^{-16}	4.15×10^{-14}

We fit all entries of the matrix Y using MIAAA with a fixed order—that is, by rational functions with a fixed number of common poles (7, 8, and 9). The approximation errors are reported in Table 2, where the RMS and relative errors are defined as before, using (2.23) and (2.24), respectively. The reported vector-fitting results are taken from (Morales-Rodriguez et al. 2019, Section III.C).

As expected, the sharp drop in errors of both vector-fitting and MIAAA approximations at order 9 are because there are only 9 distinct poles in the entries of the admittance matrix. We observe that MIAAA outperforms vector fitting for all orders considered and that MIAAA outperforms vector fitting by an order of magnitude in all but one case.

2.2.6 Further Developments

We have tested the MIAAA on different problems—not necessarily related to power lines—and we observed that it is a very robust algorithm that can provide a user-selected target accuracy. MIAAA not only outperforms vector fitting, but also—even in our preliminary implementation—is already faster than RKFIT (Berljafa and Güttel 2017), a less known alternative MIMO algorithm that can also provide accurate rational approximations.

We plan to continue our algorithmic development on two important directions:

Passivity constraint

Passivity constraints are typically enforced in an ad hoc fashion by simply replacing the undesired poles with their symmetric versions as part of the iterative process, leading to the solution of the problem. We have observed that this approach not only lacks a rigorous justification, but also could lead to significant accuracy loss. We would like to develop robust ways to enforce passivity constraints in our rational approximations and to estimate the errors introduced by enforcing passivity of solutions. Because MIAAA permits enforcing passivity in a more general way than alternative algorithms, we believe that it will allow us to minimize the accuracy losses observed in vector fitting and RKFIT when passivity is enforced. One important advantage of our approach over vector fitting and RKFIT is that we can theoretically analyze the impact of different algorithmic choices to enforce passivity. Because measurement errors might limit or prevent passive approximations, we will also use our approach to detect such errors and warn users that the data or model being used is not well represented passively.

Minimal (optimal) approximation order

Problems with multiple correlated input signals are ubiquitous in a variety of applications, and it is well understood that rational approximations with a common set of poles are an excellent tool to represent input signals. Finding optimal representations (minimal number of poles) is highly desirable because it reduces computational time and typically improves accuracy by avoiding unnecessary terms in the rational representation. The algorithms we plan to develop for the accurate and succinct representation of input data should also facilitate understanding of fundamental properties of the MIMO systems. A common strategy to tackle minimization of parameters is to split the approach into two problems—namely, first obtain an accurate but nonoptimal (too many parameters) representation, and then optimize it by exploiting the fact that the representation is already in the desired form. For this reason, we expect that MIAAA will play an essential role in our overall optimization strategy.

2.3 Suggested Improvements to Interpolation and Numerical Integration

The interpolation and numerical integration schemes used in EMTP are similar in that they both use a linear interpolation. For a single-phase, lossless line model, the equations solved by EMTP are linear and of the following form:

$$Gv(t) = i(t) - h(t) \tag{2.29}$$

where G is the $n \times n$ symmetric nodal conductance matrix, $v(t)$ is the vector of n node voltages, $i(t)$ is the vector of n current sources, and $h(t)$ is a vector of n known history terms (e.g., past nodal, current, and voltage values) (Dommel 1996). Historical terms corresponding to the line connecting nodes i and j are denoted by $h_{ij}(t-\tau)$, where the value τ is the travel time across the line:

$$\tau = \frac{linelength}{c}. \tag{2.30}$$

Interpolation becomes necessary when the travel time τ does not match up with the length of the time step Δt used to discretize the model. In such cases, linear interpolation (see (Dommel 1996)) is used to approximate the value of the historical terms to input into (2.29); however, this causes an accuracy problem: traveling wave events have a fast rise time, and thus significant errors can arise through the linear interpolation of these phenomena (see diagram in Figure 5). Further, these errors propagate throughout future time steps and become more severe as the computation of solutions proceeds with time. To illustrate the propagation of errors caused by linear interpolation, we perform a simple computational experiment using a network with three nodes and lossless lines, as described in Table 1. In Figure 2, we compare the errors of using EMTP-style computations (see Chapter 1 in (Dommel 1996)) with respect to the result of an exact method. The errors at every node—initially caused by linear interpolation—compound with time.

Also of interest for distribution systems is the modeling of inductive and capacitive elements. In such simulations, EMTP uses the trapezoidal rule for solving the resulting differential equations. In many ways, this integration rule is similar to the linear interpolation method used for the lossy line equations: given the differential equation:

$$\frac{du}{dt} = f(t,u) \tag{2.31}$$

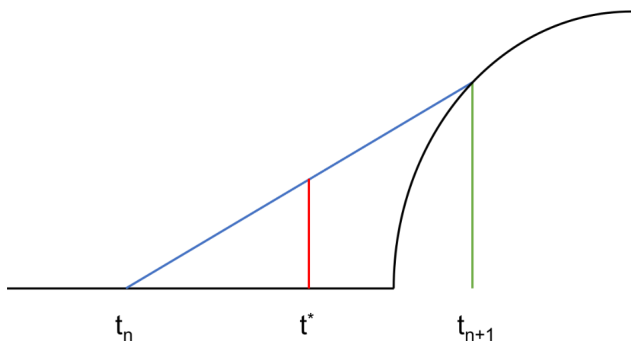

Figure 5. Error caused by the use of linear interpolation for computing historical terms.

Table 3. Simulation Setup for Testing the Effects of Linear Interpolation on EMT Solutions. This simulation was designed to use non-dimensional quantities relative to line capacitance and inductance per unit length, this representation is useful when comparing approximation error. Appropriate scaling is required to restore SI units for the four parameters listed.

Line	Length	Surge Impedance	Velocity	Propagation time
Line 1	1.0	2.8	2.6	0.4
Line 2	2.0	0.7	1.7	1.2

we invoke the fundamental theorem of calculus, integrating both sides of the previous equation:

$$\int_{t_{n-1}}^{t_n} \frac{du}{dt} dt = \int_{t_{n-1}}^{t_n} f(t,u) dt \tag{2.32}$$

Analytically evaluating the left-hand-side, and using the trapezoidal rule to approximate the right-hand-side yields:

$$u_n = u_{n-1} + \frac{\Delta t}{2}\{f(t_{n-1}, u_{n-1}) + f(t_n, u_n)\} \tag{2.33}$$

where $\Delta t = t_n - t_{n-1}$. The trapezoidal rule is implicit, A-stable, and has $O(h^2)$ global error (Iserles 2009); however, using the trapezoidal rule for modeling capacitive and inductive components has drawbacks. First, as observed by (Martí and Lin 1989), large abrupt changes in either inductor current or capacitor voltage can lead to oscillatory artifacts that can persist in the solution to the differential equations. To address this problem, (Martí and Lin 1989) suggests an approach called the critical damping adjustment, where the trapezoidal rule is used until a large change in input is detected. In the presence of such a large change, the trapezoidal rule is replaced by the implicit Euler method, which does not exhibit the oscillatory behavior. Although these approaches might be sometimes successful in damping out the artificial oscillations caused by the trapezoidal rule and sampling issues, these methods are still not very accurate. Although it is well known that the common use of the trapezoidal rule in EMTP is caused by its stability and accuracy properties, there exist more accurate numerical integration schemes that also contain favorable stability properties. For example, an implicit Runge Kutta approach to computing EMTP models was applied in (Noda, Takenaka, and Inoue 2009). This scheme has similar accuracy to the trapezoidal rule and is also A-stable. Further, implicit Runge Kutta schemes based on Gaussian quadrature rules are A-stable and can have higher order accuracy. More modern approaches to developing A-stable, implicit Runge Kutta schemes are also available (Beylkin and Sandberg 2014) and have shown promise in orbital propagation problems (Bradley et al. 2014). We intend to explore these options and determine if there are any benefits to using newer approaches instead of the trapezoidal rule. Reference (Martí and Lin 1989) provides a useful set of examples that we can mimic to explore the effects of different integration schemes, sampling rates, and step sizes in terms of their ability to accurately model higher frequency signals interacting with complicated electrical components, such as nonlinear inductors.

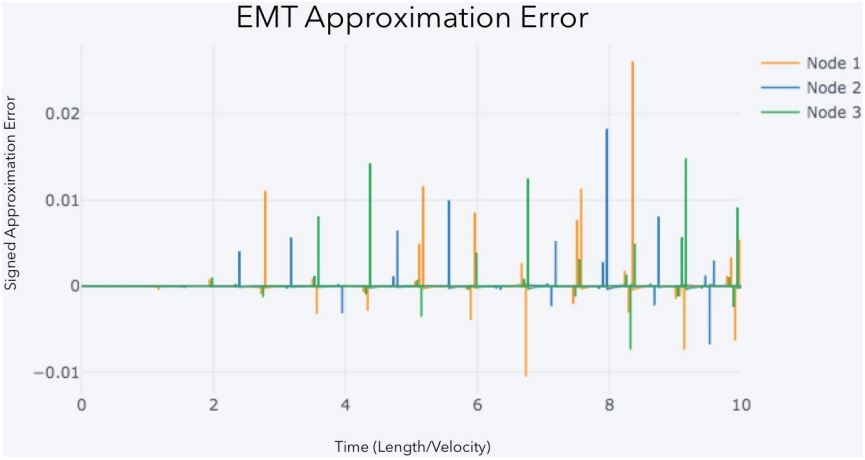

Figure 6. Errors in EMT propagation caused by linear interpolation.

3 Simulation Using Existing Electromagnetic Transient Program Platforms

Faults on a distribution line generate surges that propagate in the form of high-frequency waves at finite velocity along the line from the fault location. The propagation velocity, wave shape of these high-frequency waves and characteristic impedance of the line depend on the line parameters: resistance (R), inductance (L), capacitance (C), and conductance (G). Generally, line parameters are distributed and depend on the physical aspects of the line design, such as tower geometry, type of conductor, conductor spacing, shield wire, and insulator type. Figure 7 shows the equivalent circuit of a single conductor line of length Δx.

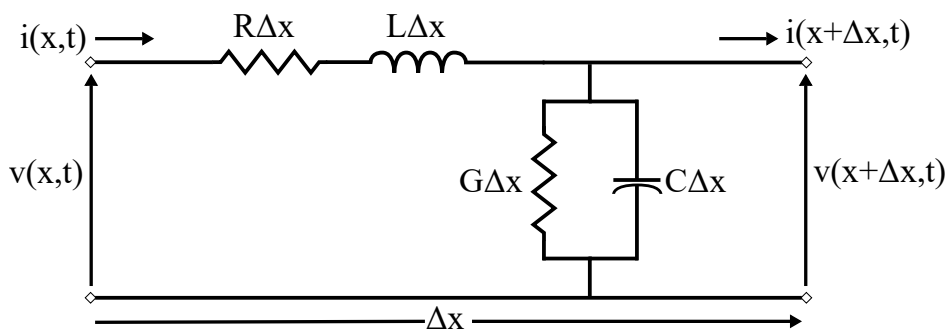

Figure 7. Equivalent circuit of single-conductor line

Consider the simple system shown in Figure 8 with a overhead line segment of characteristic impedance Z_c between buses A and B. The line left of Bus A has a characteristic impedance Z_d, and the line right of the Bus B has a characteristic impedance Z_e. A fault on the line between terminals A-B (as shown in Figure 8) initiates the wave transients A_i & B_i (voltage and current) traveling at approximately the speed of light. As the fault-generated transients approach the terminals A-B, part of the wave is reflected as A_r & B_r, and the rest is transmitted as A_t & B_t to the adjacent sections of the terminal. This reflection and transmission of the high-frequency wave at the junction (or taps) are caused by the changes in characteristic impedance.

These waves also attenuate as they propagate along the line because of losses caused by the line resistance (R) and conductance (G). Attenuation of these waves is greater in distribution systems because of the higher resistance in the lines.

Use of such traveling waves for fault detection and fault location in transmission systems are relatively straightforward by using the characteristics of the line, such as length and impedance, but there are challenges in using the traveling wave-based approach in a distribution network. This is because of the presence of unbalanced short lines, underground cables, transformers, voltage regulators, capacitor banks, and frequent taps (points of discontinuities), which can impact traveling waves in a distribution system.

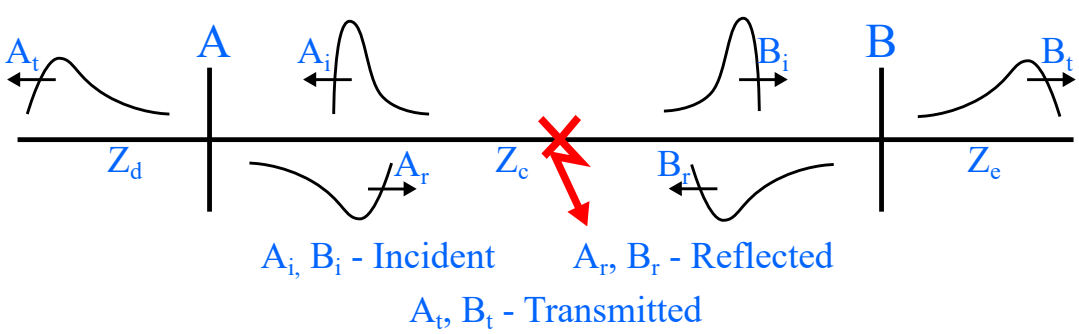

Figure 8. Illustration of traveling wave at junctions

Accurate representation of the component model is crucial for all transient analysis. Power systems component modeling for EMT analysis is developed by considering the frequency band of the transients to be analyzed and the frequency dependence of the parameters. Figure 9 shows the general classification of the line models applicable to overhead lines and underground cables. Line models are divided into two groups: lumped and distributed parameter models. Selecting the model group depends on the highest frequency involved in the study and, to a lesser extent, on the line length.

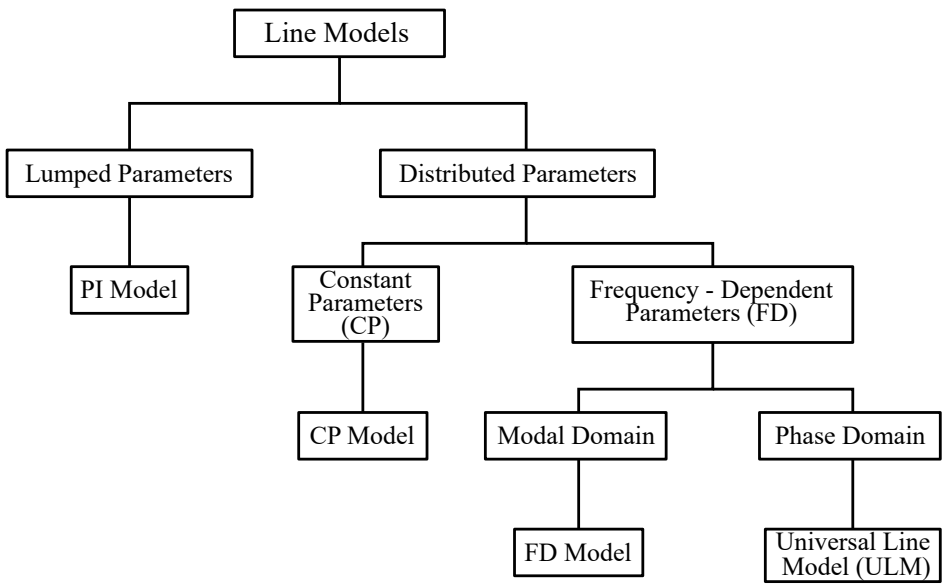

Figure 9. Classification of line and cable model based on software modeling approach

3.0.1 Lumped Parameter Models

Lumped parameter models, also known as pi models, represent the lines and cables by using lumped resistance (R), inductance (L), conductance (G), and capacitance (C) elements. These values are calculated at a single frequency of interest. These models are commonly used for steady-state analyses, but they can also be used for transient studies provided the parameters are evaluated at the frequency of interest. In some cases, these short pi sections are cascaded to approximate the distributed nature of the line. The number of such sections depends on the expected frequency of the transient (*Guidelines for Representation of Network Elements When Calculating Transients* 1990). Cascaded pi sections are computationally expensive because of the increase in matrix size. Because pi models do not represent a propagation delay and attenuation of waves, they are best suited for steady-state analyses where high-frequency events are ignored.

3.0.2 Distributed Parameter Models

Distributed parameter line models are divided into two subgroups: constant parameter and frequency dependent.

Constant Parameter Model

A constant parameter or Bergeron's model calculates the line parameters at a single frequency. Then the calculated line parameters (inductance and capacitance) are distributed. The losses in the line are represented through lumped resistances at three discrete points along the line (at 25%, 50% and 75% of line length) (Neville Watson and Jos Arrillaga 2003). Because the line impedances are assumed to be frequency independent, this approach gives inaccurate results if the frequency of the event under study differs from the frequency used to calculate the parameters.

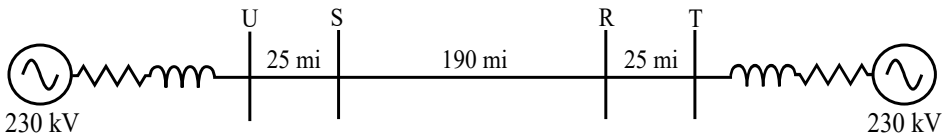

Figure 10. High-voltage, 230-kV, four-bus transmission test network

Frequency-Dependent Model

The frequency-dependent model has the potential to represent the frequency-dependent nature of the line. Frequency-dependent line/cable models can further be divided into two groups based on the domain in which the frequency-dependent line parameters are evaluated: modal and phase domain.

A modal domain model uses the transformation matrix to transform quantities from phase to mode. The frequency dependence of the line parameters are considered in modal domain. The frequency-dependent model assumes the frequency-independent transformation matrix, which is constant and real (Marti 1982). The accuracy of the frequency-dependent model is limited to symmetrical or balanced overhead lines because the transformation matrices are frequency dependent for unbalanced lines and cables.

The Universal Line Model (ULM) is a phase domain model that works directly in the phase domain by taking the full frequency dependence of the line parameters in the form of the characteristic admittance (YC) and the propagation constant (H) matrix transfer functions (Morched, Gustavsen, and Tartibi 1999). ULM models avoid the transformation matrix and simplifying assumptions in the form of modal to phase transformations. This model is highly accurate for any overhead line and underground cable configurations. The ULM model or wideband model is the best choice for most EMT studies and is used in this study.

3.1 Simulation Cases for Comparing Traveling Wave Characteristics and Results

This section describes the test networks that are simulated in EMTP-RV to present the characteristics of traveling waves under different transient events and the results from the simulation scenarios. A four bus transmission network and a five bus distribution network were simulated.

Because there is plenty of literature on traveling waves in transmission systems, only one transmission system test case is simulated in this report. But for the distribution network, four different scenarios are simulated. The focus is to provide a clear understanding and characterization of traveling waves using generic representative features of the distribution system under different system topologies.

3.1.1 Test Network Characteristics

The test network for the transmission simulation scenario is shown in Figure 10. This test network is a four bus (buses U, S, R, and T) 230 kV system with two sources at buses U and T. Lines are characterized by long and short lines, with 40.24 km (25 miles) of line length between buses U-S and R-T, and with 305.78 km (190 miles) of line length between buses S-T. [3]

The test network for the distribution simulation scenario is shown in Figure 11. This test network has five buses: U, S, R, T, and V. The line lengths between the five buses are shown in Figure 11.

The overhead lines and underground cables in the transmission and distribution test networks are modeled using ULM. The tower structure and conductor spacing were modeled using the rural utility standard 1724E-200. Finally, the sources used in both test networks are modeled as voltage source behind a equivalent Thevenin impedance. The impedance values are calculated from the fault MVA at base system frequency.

[3] In keeping with trade practice amongst U.S. based electrical utilities, the unit of distance miles is used in place of the SI unit kilometers in some of the diagrams in this report.

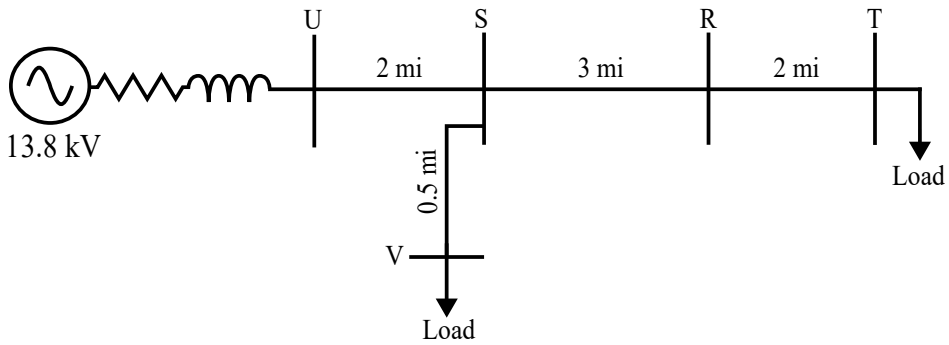

Figure 11. Medium-voltage, 13.8 kV, five-bus distribution test network

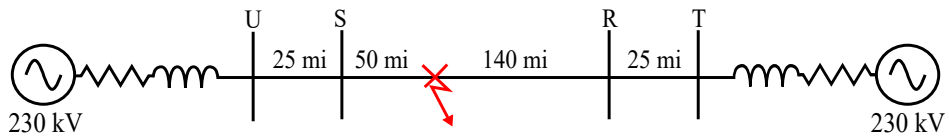

Figure 12. Scenario 1: phase-to-ground fault in overhead line section between buses S and R in the test transmission network

3.1.2 Simulation Scenarios

This subsection describes the transient scenarios simulated in EMTP-RV using the test network systems to provide the characteristics of traveling waves under different network and system conditions.

Scenario 1: phase-to-ground fault in overhead line section between buses S and R in the test transmission network

In this scenario, a phase-to-ground fault was simulated in the test transmission network. The fault was simulated in Phase A at the overhead line section between buses S and R. The fault was simulated at approximately 80.47 km (50 miles) from Bus S and 225.31 km (140 miles) from Bus R, respectively. This is shown in Figure 12. In this research, this scenario is used as the benchmark for studying traveling wave behavior in a simple transmission system.

Scenario 2: phase-to-ground fault in overhead line section between buses S and R in the test distribution network

In this scenario, a phase-to-ground fault was simulated in the test distribution network. The fault was simulated in Phase A at the overhead line section between buses S and R. The fault was simulated approximately 1.61 km (1 mile) from Bus S and 3.22 km (2 miles) from Bus R, respectively. This is shown in Figure 13. In this research, this scenario is used as the benchmark for a studying traveling wave behavior in a simple distribution system.

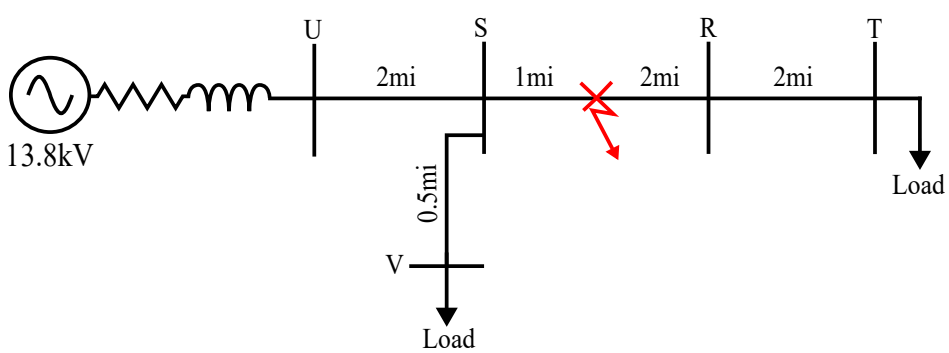

Figure 13. Scenario 2: phase-to-ground fault in overhead line section between buses S and R in the test distribution network

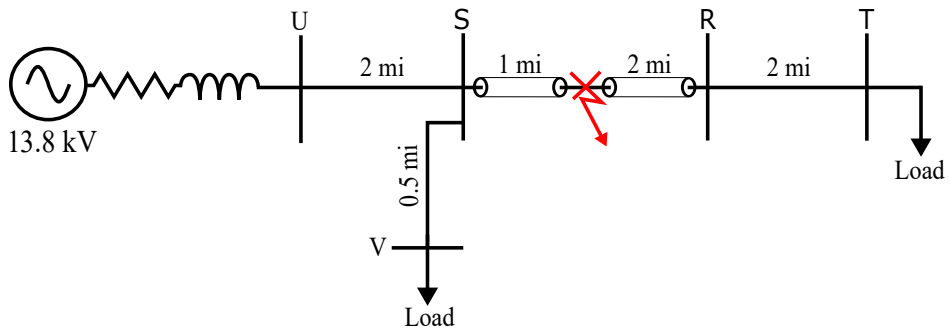

Figure 14. Scenario 3: phase-to-ground fault in underground cable section between buses S and R in the test distribution network

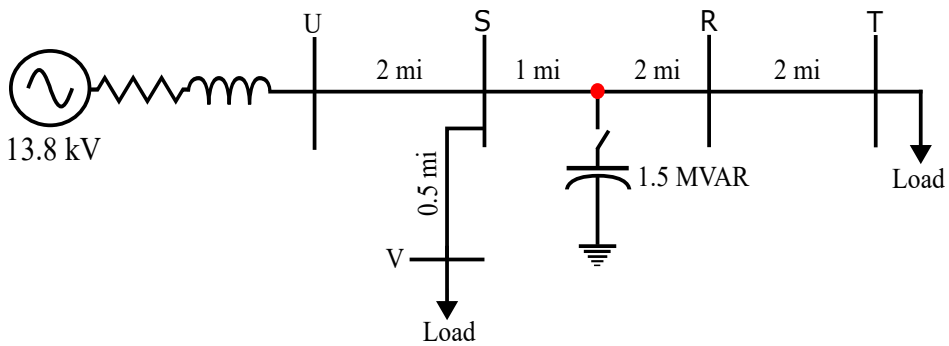

Figure 15. Scenario 4: energizing capacitor bank between buses S and R in the test distribution network

Scenario 3: phase-to-ground fault in underground cable section between buses S and R in the test distribution network

Similar to Scenario 2, a phase-to-ground fault was simulated between buses S and R, but the overhead line section between S and R was replaced with an underground cable section. The test scenario is shown in Figure 14. The results from this scenario are compared with those from Scenario 2 to show the impact of underground cables on traveling wave propagation.

Scenario 4: energizing capacitor bank between buses S and R in the test distribution network

In this scenario we see the difference between a fault-generated transient and a capacitor energizing-based transient. The fault transient event in Scenario 2 is replaced by a capacitor bank energizing event. This scenario assumes that the capacitor bank is energized in the same location as the fault in Scenario 2—that is, the capacitor bank was energized between buses S and R 1.61 km (1 mile) from Bus S and 3.22 km (2 miles) from Bus R. This scenario is shown in Figure 15. The reasoning behind the location of the capacitor bank is to show the difference in the frequency content between a fault transient event and a capacitor bank energizing event.

Scenario 5: phase-to-ground fault in overhead line section between buses S and R in the test distribution network in the presence of multiple sources

This scenario explains the behavior of traveling waves in the presence of multiple sources in the distribution system. The model used in Scenario 2 was used with another source added at Terminal T, as shown in Figure 16.

3.1.3 Analysis of Simulations Results from the Transmission and Distribution Test Systems

The EMT models are simulated at a time step of 100 ns. Current and voltage measurements are included in all the terminals and recorded at each time step. The measured voltage and current values are filtered using a passive linear

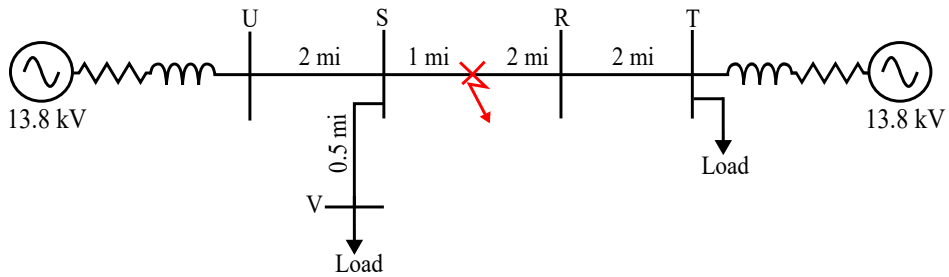

Figure 16. Scenario 5: phase-to-ground fault in overhead line section between buses S and R in the test distribution network in the presence of multiple sources

hight pass filter with rolloff (-3 dB) at 10 kHz.[4] In all the simulation scenarios, the simulation is allowed to settle, and a phase-to-ground fault on Phase A is applied at 51.83 ms (Phase A voltage peak).

Comparison between Scenario 1 and Scenario 2

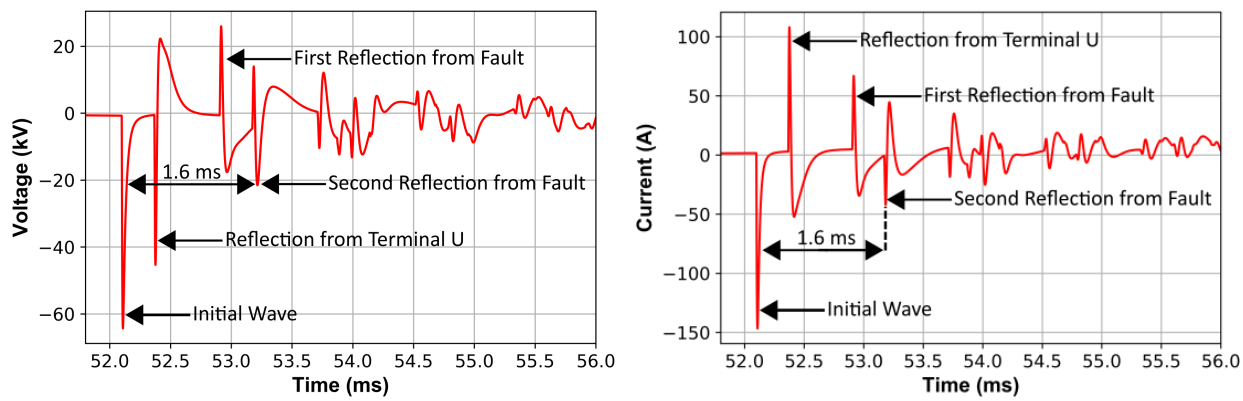

(a) Filtered voltage **(b) Filtered current**

Figure 17. Voltage and current traveling waves for a phase-to-ground fault in transmission test network between terminals S-R

The filtered voltage and current measurements at Bus S for both Scenario 1 and Scenario 2 are shown in Figure 17 & 18, respectively. An immediate observation is the order of magnitude difference between the time intervals on the X-axis for Figures 17 and 18. While the former has a window length of approximately 4.00 ms, the latter has a window length of approximately 0.25 ms; illustrating the theoretical determination that the propagation velocities for traveling waves are higher in distribution circuits than transmission circuits. Reduced propagation times translate to the need for wider bandwidth transducers in distribution systems than transmission systems to ensure effective detection of wave fronts. An additional challenge in the design of transducers and algorithms is that these reflected waves are often superimposed in time, as shown in Figure 18 (a) & 18 (b). Also note that reflected voltage and current waveforms bear opposite sign, as evident in Figure 17 (a) & 17 (b). This superimposition of traveling waves makes it challenging to differentiate wavefronts reflected from the myriad of discontinuities (such as branches, terminations and interconnects) that exist in a distribution system.

Comparison between Scenario 2 and Scenario 3

Distribution systems have more underground cables when compared to transmission systems. The characteristic impedance of an underground cable is approximately 10 times less than that of overhead lines. The fault-generated

[4]Time steps and frequency set points mentioned here are parameters passed to a numerical simulation. The uncertainty in simulated results emerging these values were not characterized.

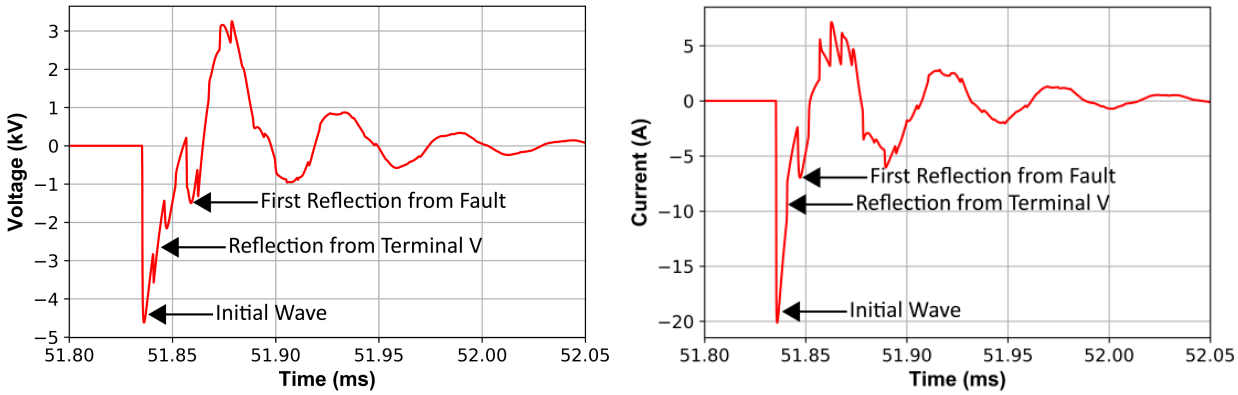

(a) Filtered voltage **(b) Filtered current**

Figure 18. Voltage and current traveling waves for a phase-to-ground fault in the distribution test network between terminals S-R

traveling waves will experience different mediums of propagation when they travel through underground cables and overhead lines. In an underground cable, traveling waves travel at approximately 50% of the speed of light. This is much slower than that of overhead lines. In Scenario 3, when the fault is simulated at 51.83 ms, voltage and current waves are launched (similar to Scenario 2), moving away from the fault point toward buses S and R. A comparison of the voltage traveling waves between Scenario 2 and Scenario 3 is shown in Figure 19. The reflections take much longer to arrive back (even though the distance traveled by the waves is the same in Scenario 2 and Scenario 3). The voltage signals at terminal S shown in Figure 19 move slower through the cables than the overhead lines. Discernable wave features are sustained longer due the lower dissipative resistivity of underground cables. The slower rate of propagation as well as the different characteristic impedance directly affect traveling wave propagation requiring special consideration given to detecting and triangulating faults in distribution systems that have a mix of overhead lines and underground cables.

Comparison between Scenario 2 and Scenario 4

Capacitors are predominantly present in distribution systems to address the power factor and voltage regulation issues. Utilities switch the capacitors during peak loads and remove them when the load drops ("Application of Capacitors on Rural ELectric Systems" 2018). This capacitor switching causes transient surges that are similar to those generated during a fault. It was important to understand the behavior of traveling waves during capacitor bank switching and contrast them against fault originated traveling waves. The system shown in Figure 15 is simulated with a capacitor bank of 1.5 MVAR capacity. High-frequency transients initiated by switching the capacitor bank are similar to the fault initiated signals. This comparison, as observed at Terminal S, is shown in Figure 20 (a). Transients generated while energizing capacitor banks sustained longer than fault originated waveforms. In addition, capacitor bank energization spectra differ from phase-to-ground faults. A low-pass filter with roll-off (-3 dB) at 1 kHz was applied to both signals and the results are shown in Figure 20 (b) this filtered signal highlights the difference between the low-frequency features associated with energy transfer into (and from) the capacitor bank that are not present in fault signatures. These low-frequency capacitor bank transients depend on the lumped circuit inductance in the charging and discharging path and can be estimated using the methods in (Selman 1990). In summary, the transients emerging from capacitor banks can be differentiated from fault-generated transients by the merit of their spectrum and with the use of model based estimation.

Comparison between Scenario 2 and Scenario 5

Finally, the comparison between Scenario 2 and Scenario 5 is shown in Figure 21 (a) & 21 (b). It is evident from Figure 21 (a) that the presence of a source at Terminal T does not affect the behavior of the waves. At terminal R, the presence of a source in Figure 21 (b) shows that the oscillatory signal has a higher voltage magnitude overall because of the prefault voltage support from the source. This scenario is particularly relevant for future distribution systems

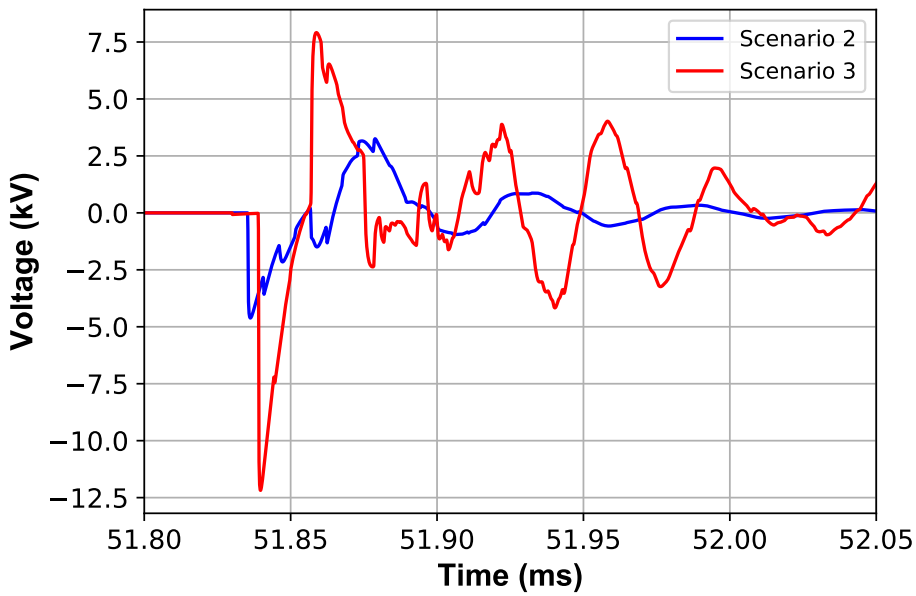

Figure 19. Voltage traveling waves observed at Terminal S for Scenario 2 and Scenario 3

where stochastic or diurnal source strength and fault current contribution from distributed energy resources have to be considered in the fault protection scheme.

3.2 Test System for High-Frequency Wave Validation

Figure 22 is a modified version of the IEEE 13-bus test distribution system (Kersting 2001) . This modified test system has one feeder operating at 13.8 kV. This feeder runs from the substation for a total length of 6.44 km (4 miles). There are four taps taken off the main feeder to represent real-world feeder taps. We use this example of a distribution circuit with many of the features of a typical distribution system to understand the propagation of fault initiated signals.

Configurations for tower structures, overhead lines, and underground cables used in the test system are based on ("Distribution Conductor Clearances and Span Limitations" 2003). The configuration details are presented in Figure 23. Table 4 shows the various conductors used in the overhead line configurations. Figure 23(a), (b), & (c) show the geometric structure of the overhead lines and conductor spacing. Concentric neutral cable (250 AWG) data taken from (Kersting 2001) are used for the underground cable modeling (shown in Figure 23 (d)). The overhead lines and underground cables in the test networks are modeled using ULM.

Alpha-mode velocities per ULM are overlayed on the network topology of the test system in Figure 22 (b). Table 5 shows the single- and three-phase loads modeled in the test system. The steady state loads set the prefault current for the network in steady state. The source in the test network is modeled as a voltage source behind the equivalent Thevenin impedance. The impedance values are calculated from the fault MVA at power frequency.

3.3 Simulation of Transient Scenarios for High-Frequency Study

This section outlines multiple fault transient scenarios that were simulated to characterize traveling wave propagation in a multi-line distribution network. The simulations are run at a time step of 100 ns. Faults are applied 51.83 ms (Phase A voltage peak) after initialization. Current and voltage values were obtained from every bus at a rate of 10^6 Hz in order to adequately record traveling wave phenomena. The reported values from each bus are filtered through a linear high-pass filter with a cutoff frequency of 10 kHz. Two fault types—single-line-to-ground (SLG) and line-to-line—are simulated in two locations: first on the main feeder and second on Tap 1.

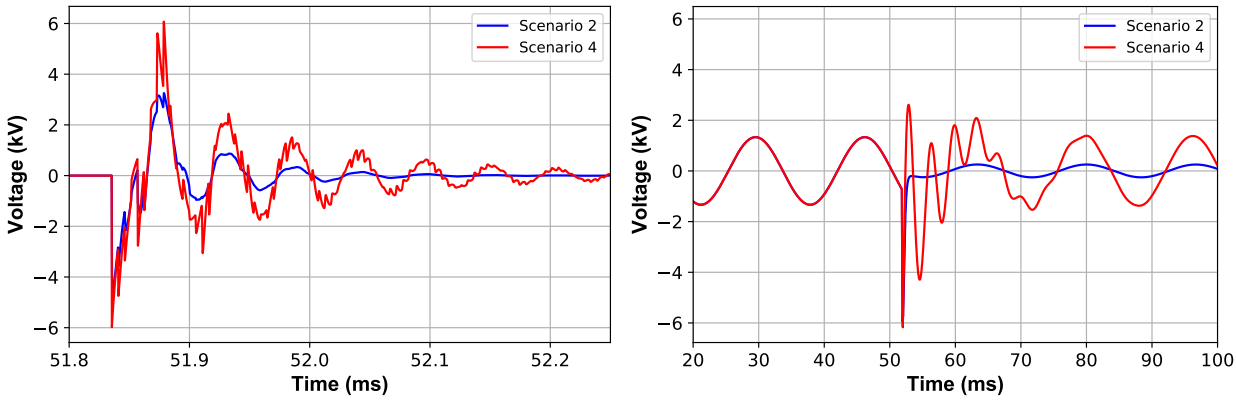

(a) Voltage filtered at high frequency

(b) Voltage filtered at mid-band frequency

Figure 20. Capacitor switching and phase-to-ground fault-generated voltage traveling waves observed at Terminal S

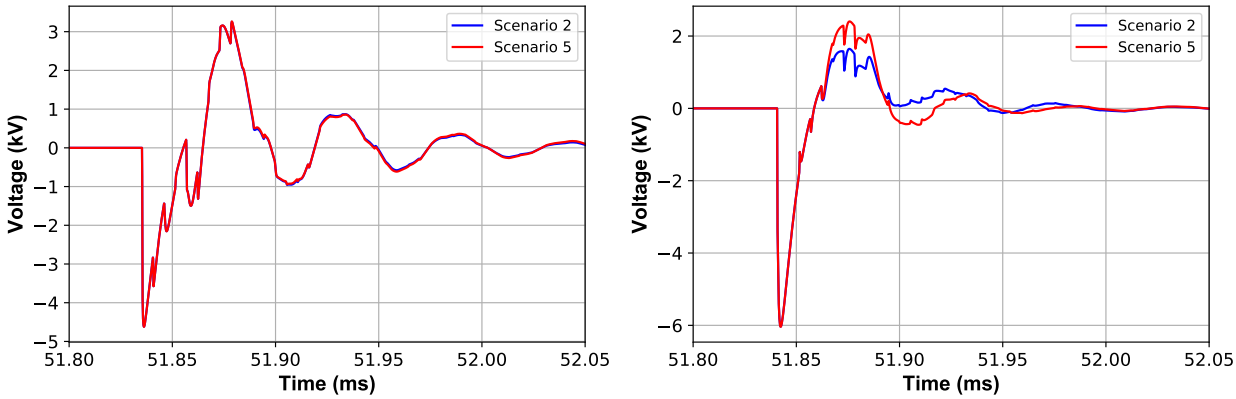

(a) Terminal S

(b) Terminal R

Figure 21. Voltage traveling waves for a phase-to-ground fault between terminals S and R in the test system with one source and two source

3.3.1 Overhead Lines with Single-Line-to-Ground Fault on Bus 680

An SLG fault is applied on Phase A at Bus 680 (see Figure 22 (a)). High-pass filtered signals from Taps 1 and 3 are plotted in Figures 24 and 25 to show the arrival times for fault features. The times observed can be compared to the theoretical propagation times overlayed on Figure 22 (b). The faulted bus current (at bus 680) is included in all the plots as a reference to compare the wave arrival estimates.

High-frequency current features are smaller in magnitude in proportion to the line voltage. Voltage and current waves are initiated at the fault point on Phase A at time index 51.83 ms. The current waves propagate and arrive at bus 671B; part of the energy is reflected back; and the rest gets split between Tap 3, Tap 4, and the main feeder. The initial current wave times estimated from Figure 22 (b) in Tap 3 (at buses 671B, 684, 611) are 5.39, 10.78, and 12.42 μs, respectively. From the simulations, they arrive at 5.3, 10.7, and 12.3 μs, as shown in Figure 24. Faulted Bus 680 records considerably longer duration waves with higher magnitude, as shown in Figure 25, than the waves in Tap 3. This is because the wave energy attenuates as it travels away from the fault point.

Phase-to-ground instantaneous values of the bus voltages in Tap 3 are shown in Figure 24 (a). The estimated times of arrival at each bus are determined in the same way as the currents. Voltage and current present similar wave propagation characteristics, so the wave arrival times mentioned in Figure 24 (b) are applicable to Figure 24 (a).

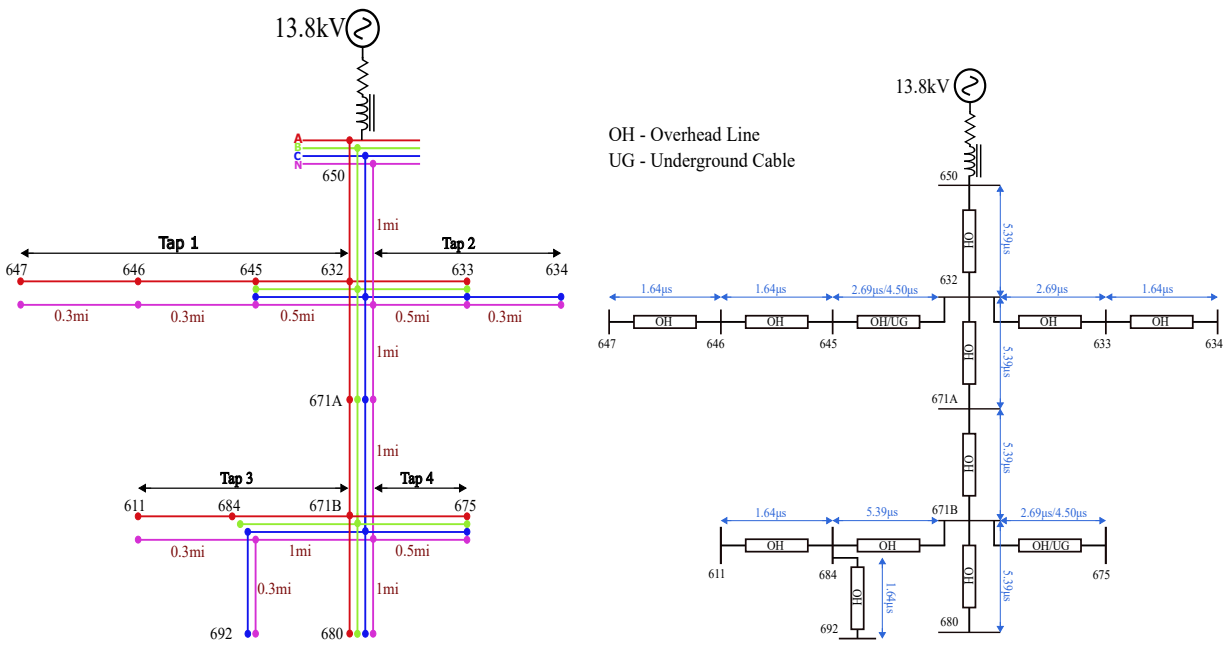

(a) Network structure **(b) Propagation time in the simulated network**

Figure 22. Modified IEEE test system used in EMT simulation

Current transients recorded in the Tap 1 buses are shown in Figure 25 (b). Signals in the Tap 2 bus timings are very close to the estimated times shown in the timing diagram. Comparing the magnitude of the wave that arrived at Tap 1 and Tap 3 in Figure 24 (b) and 25 (b), the former is lower than the latter because of the attenuation when the way travels through the 2 mi of the main feeder. More taps result in the wave energy getting split at every tap. As the wave attenuates, it also gets broader in shape due to frequency dependent attenuation —losing its sharp rising edge. Initial waves arriving at the bus terminals are always distinct from the system under normal conditions because these wave transients exist only during faults and switching. For faults on the main feeder, any taps that are far from the fault might not see measurable reflection from the fault because the energy dissipates in every line between the fault and the tap. The closest taps might see the second wave from the fault.

Voltage signals in the Tap 1 buses are shown in Figure 25 (a). The peak voltage of the traveling wave at Bus 632 is approximately 1.7 kV—compared to 4.1 kV at Bus 671B. Because Bus 632 three-phase and Bus 645 single-phase line are impedance matched, most of the reflected energy is transmitted to an adjacent line. In distribution systems, different conductor types may be used even if the voltage level in a line remains the same. Different conductor types could present discrete changes in line parameters including characteristic impedance but for the conductors chosen in this simulaton impedance differences appear to be minimal. As a consequence, Figure 25 (a) shows that signals in adjacent buses are only displaced in time. A greater difference in characteristic impedance is seen with underground cables in the network.

3.3.2 Overhead Lines and Underground Cables with a Single-Line-to-Ground Fault on Bus 680

Underground cables are most commonly used in distribution systems to serve densely populated areas. The characteristic impedance of an underground cable is approximately 10% that of the overhead lines and the wave propagation velocity is approximately 50% the speed of light because of the insulation permittivity. These crucial differences impact the speed and the attenuation inside the cables. Understanding and studying these differences between overhead lines and underground cables are critical when using traveling wave based protection schemes for systems with both overhead and underground cables.

To evaluate the impact of overhead versus underground cables, lines between buses 632 and 645 and between buses

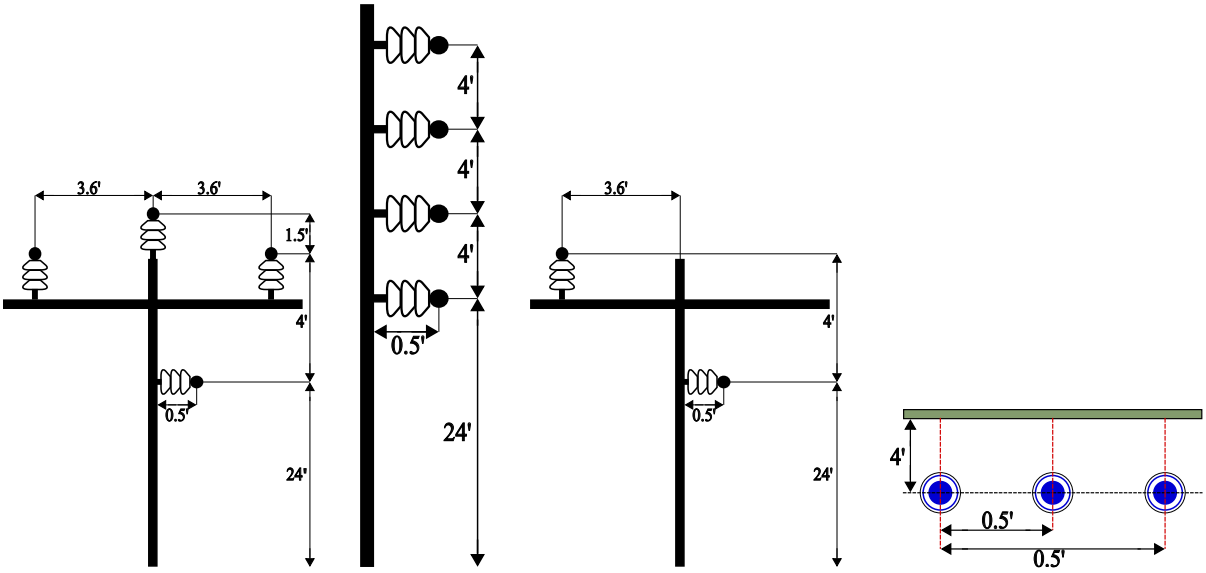

(a) ID-500 (b) ID-505 (c) ID-510 (d) ID-515

Figure 23. Overhead line tower geometry and underground cable layout

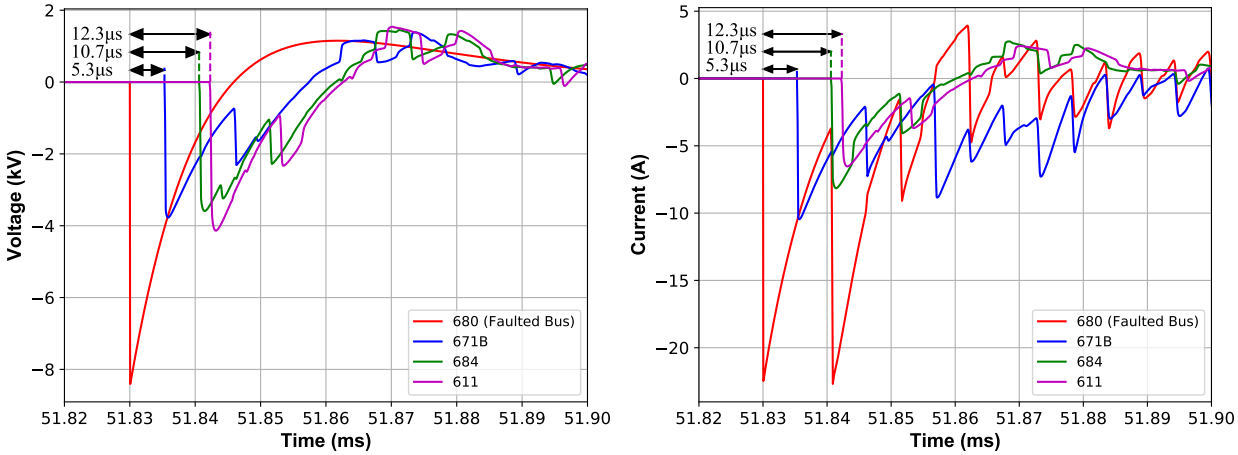

(a) Filtered voltages in Tap 3 buses for an SLG fault (b) Filtered currents in Tap 3 buses for an SLG fault

Figure 24. Traveling waves observed in voltage and current measurements from Tap 3 buses under SLG fault conditions

Table 4. Overhead Line Data. The units used in this table are not SI but reflect parlance commonly used by electrical utilities.

Node A	Node B	Length (mi)	Phase (AWG)	Neutral (AWG)	Spacing ID
650	632	1	4/0	1	500
632	633	0.5	1/0	2	505
633	634	0.3	4/0	1	510
632	645	0.5	1/0	2	505
645	646	0.3	4/0	1	510
646	647	0.3	4/0	1	510
632	671A	1	4/0	1	500
671A	671B	1	4/0	1	500
671B	680	1	4/0	1	500
671B	675	0.5	1/0	2	505
671B	684	1	4/0	1	500
684	611	0.3	4/0	1	510
684	692	0.3	4/0	1	510

671B and 675 are replaced by a 3-single core underground cable. Each cable has a central conductor to carry load current and fault current and an outer sheath to carry ground fault current. Characteristic impedance was observed to change significantly as expected. Figure 26 compares the observations at Tap 4 to show a comparison between voltage signals at the buses 671B and 675 when the change was made. Traveling wave features appeared to be superimposed on an 8 kHz resonant mode requiring a high-pass filter tuned at 10 kHz to produce feature comparison in Figure 26.

Consistent with expected performance underground cables have slower propagation times of 4.5 μs as opposed to 2.6 μs for overhead lines. Voltage signals at Bus 671B and Bus 675 also appear to have smaller magnitudes when underground cables are used instead of overhead lines — also an expected observation given the dissipative properties of insulation permittivity.

Table 5. Test System Load Data

Bus	Type	Real Power (kW)	Reactive Power (kVAR)
647	1-ph	100	50
634	1-ph	100	50
692	1-ph	30	1
611	1-ph	100	50
645	3-ph	500	250
633	3-ph	5000	2500
675	3-ph	500	100
680	3-ph	2000	1000

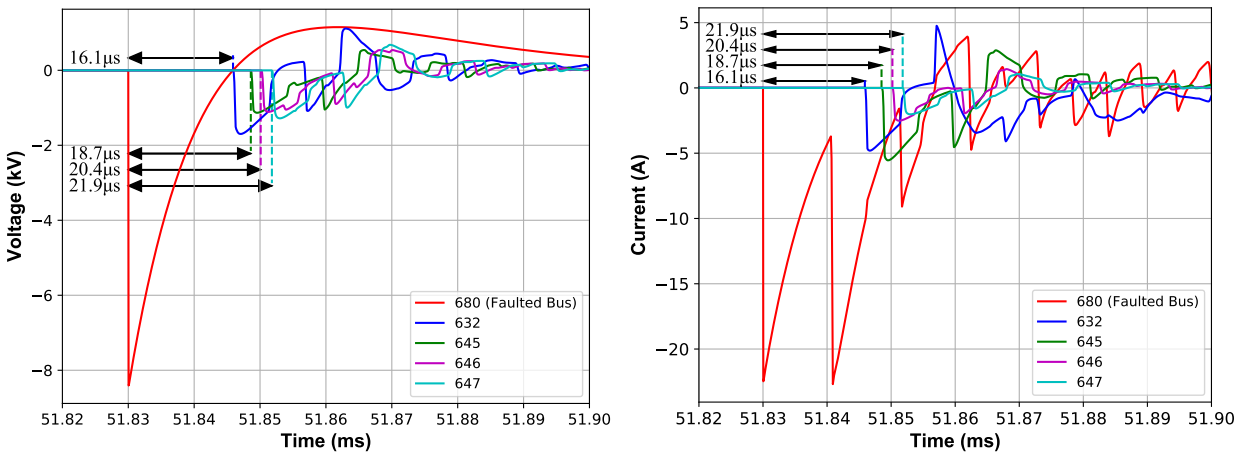

(a) Filtered voltages in tap 1 buses for a SLG fault

(b) Filtered currents in tap 1 buses for a SLG fault

Figure 25. Traveling waves observed in voltage and current measurements from Tap 1 buses under SLG fault conditions

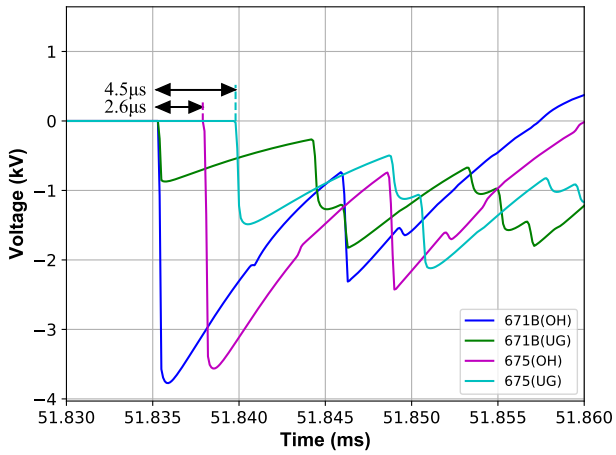

Figure 26. Voltage wave travel between overhead and underground in Tap 4 for a SLG fault

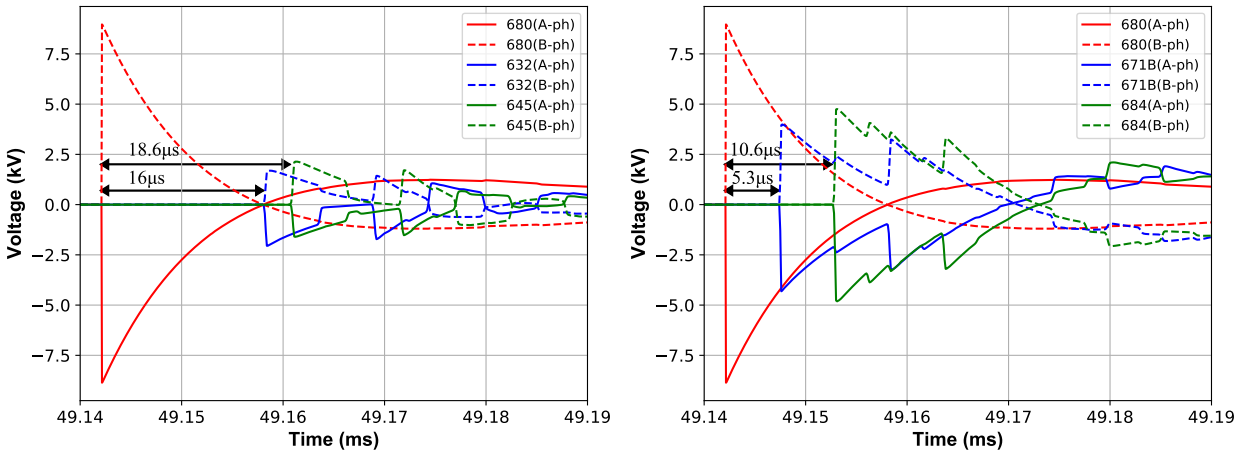

(a) Filtered voltages in Tap 1 buses for a line-to-line fault

(b) Filtered voltages in Tap 3 buses for a line-to-line fault

Figure 27. Traveling waves observed in voltage measurements under line-to-line fault conditions

3.3.3 Overhead Lines with Line-to-Line Fault on Bus 680

A line-to-line fault is the second most commonly occurring fault in the power system. An SLG fault on Bus 680 is replaced by a line-to-line fault between phases A and B in this scenario. Wave transients that are propagated in phases A and B are equal in magnitude and opposite in polarity. This phenomenon is also observed in the current during a line-to-line fault event. When the waves propagate down the line in both phases, they attenuate and disperse based on the characteristic impedance of two phases. For horizontal line and vertical line configuration, distributed parameters—such as inductance and capacitance—are the same for all phases except for the mutual impedance, resulting in small differences in magnitude and dispersion of the waves in both phases.

A fault is applied at 49.14 ms, when the instantaneous difference in phase-to-phase voltage is large enough to clearly observe. The arrival times of the waves match the estimated values shown in Figure 22 (b). Voltage waves of the selected buses in Taps 1 and 3 are shown in figures 27 (a) and 27 (b). A maximum voltage difference of 17.8 kV is observed between the phases at 49.14 ms. An overhead line between Bus 680 and Bus 671B is horizontally configured, with Phase B slightly above phases A and C. Transients in both phases look very similar in terms of attenuation and dispersion. There is a difference in the magnitude observed in Figure 27 (a) because of the difference in characteristic impedance. As the waves travel away from the fault, magnitude, attenuation, and dispersion between the phases become distinct, as shown in Figure 27 (b). The line between Bus 632 and Bus 645 is vertically configured resulting in the wave experiencing different distributed characteristic impedances.

3.3.4 Overhead Lines with Single-Line-to-Ground Fault on Bus 645

All the cases discussed so far have the fault on the main feeder. In this case, the fault is assumed in the laterals closer to the substation at Bus 645 in Tap 1. When the waves move away from the fault in both directions, one travels down the lateral until it gets reflected, and the other reaches the junction and gets reflected back toward the fault. Voltages in the tap are plotted starting with the faulted bus (see Figure 28 (a) and 28 (b)). The first wave reaches Bus 646 1.6 μs after the fault. Single-phase lines between buses 645, 646, and 647 have the same characteristic impedance so the wave launched at 645 attenuates as it travels through two lines unreflected until it reaches Bus 647. The waves in the other direction of the fault reach the junction at Bus 632 after 2.6 μs.

Filtered voltages at buses in Tap 3 are plotted in Figure 28 (b). Compared to the signal peak at Bus 632, 43% of the wave is recorded at 671B. Traveling wave features observed at buses 632 and 671B are sustained longer than buses inside the tap. Intuitively, relays located on circuit taps are best able to detect and isolate faults close to the junction on the main feeder or on the tap itself.

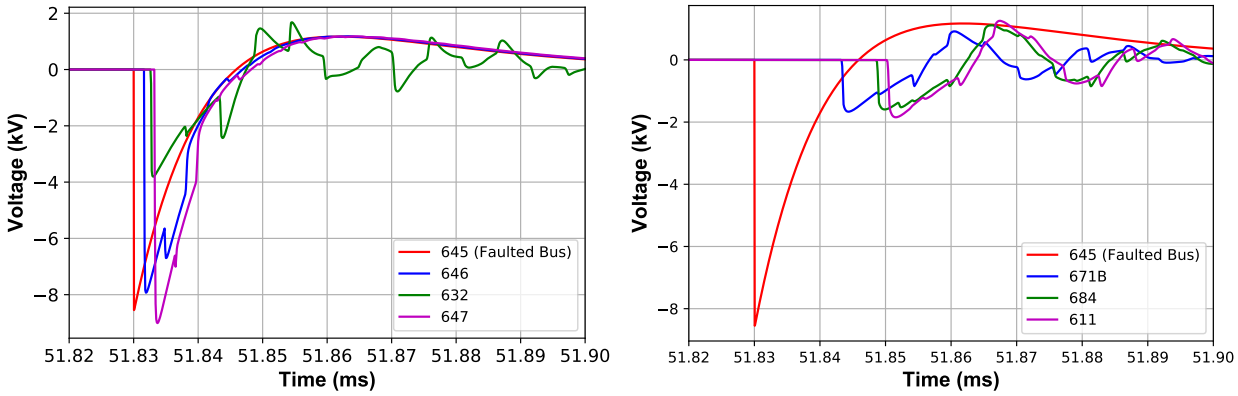

(a) Filtered Voltages in Tap 1 buses for a SLG fault

(b) Filtered voltages in Tap 3 buses for a SLG fault

Figure 28. Traveling waves observed in voltage measurements under SLG fault condition at Bus 645

3.3.5 Summary of Simulation Results Using the High-Fidelity IEEE 13–Bus System Model

The simulation results for the faults on the main feeder show that two taps beyond the faulted bus might not see a measurable second wave reflection from the fault. The results show that the line-to-line fault transient attenuation is less than those of the faults that involve the ground line. High-frequency waves are attenuated faster in laterals because of the high resistance of conductors combined with skin effect. The impact of attenuation is illustrated in our results when the fault location is changed from the main feeder to a tap. In the scenario simulated in Subsection 3.3.2, results show that waves travel slower through underground cables than overhead lines.

3.4 Requirements for Field Implementation of Traveling Wave Approach in Distribution System

Our analysis is in agreement with an industry wide observation that there are challenges in using legacy sensing equipment for the traveling wave-based protection approach. Measurement devices such as current transformers and potential transformers are not typically designed for wider band frequency measurements. Further, IEDs that process measurements to identify, isolate and localize faults might not have the necessary processing and communication capabilities. Lastly, existing instrumentation lack time-synchronization capabilities at the level of performance and accuracy that is essential for traveling wave analysis. Despite the current limitation of available measurment and processing technology in the field, traveling wave-based protection schemes hold promise for faster detection of transient events in distribution systems.

Current Transformers and Potential Transformers

Current transformers and potential transformers used in distribution systems today are optimized for nominal 60 Hz operation. Power systems metrology applications rarely require frequency response above 100 kHz. Current transformers therefore have large error budgets (exceeding 10% error) at frequencies between 100 kHz and 500 kHz (Redfern et al. 2003),(Redfern 2004). There is limited information available about potential transformers but one can assume a similar performance specification would apply to them as well. As seen in previous sections in this report, distribution system disturbances generate signatures that have spectral footprint that would benefit from measurement devices with wider bandwidth than installed currently (Bo, Weller, and Redfern 1999). In addition, traveling wave based protection requires current transformers and potential transformers to accurately reproduce the time domain wave shape of transients. From our testing we expect that measurement instrumentation needs to have a usable frequency bandwidth of approximately 10^7 Hz.

Digital Signal-Processing and Time-Synchronization Requirements

Noting the desired sensor bandwidth of 10^7 Hz, sampling and digital conversion hardware within IEDs will also need to significantly upgraded to ensure the desired fidelity in processing. While the nuance of sampling rate and digitization

resolution is beyond the scope of this report, we expect as a rule of thumb that the digitization pipeline be able to operate at approximately 10^8 samples-per-second (Shannon 1949) to meet the needs of the distribution system. This rate is significantly higher than the 10^6 samples-per-second rate used by IEDs in present day transmission systems. This requirement is in part because of the shorter line length and the superposition of the reflected and transmitted waves (Schweitzer, Kasztenny, and Mynam 2016). We also expect that significant speed ups in signal processing and feature detection will be required in order to extract traveling wave signatures fast enough for on-line fault detection. In addition to the signal-processing requirements, traveling wave signature based localization requires accurate time synchronization between IEDs, measurement points and processing nodes. Uncertainties associated with reflections at points of impedance mismatch, changing line parameters and dispersion of fault features further emphasize the need for a precise global time scale in order to accurately localize the originating fault based on its traveling waves. In the tests performed in this report, we anticipate a synchronization system with an integrated clock offset error $<10^{-9}$ s. We recognize that the high timing accuracy requirement has long been an impediment to the practical deployment of traveling wave based fault detection systems however, recent trends in wide area time synchronization (Lipiński et al. 2018), (Gutt et al. 2018), (Morton et al. 2021) do purport to meet the timing performance we assume in our work.

4 Experimental Fault Recreation To Study High-Frequency Signatures in Distribution Lines

This chapter focuses on hardware emulation of the fault, metrology, and analysis of fault signatures on a distribution system with a high penetration of IBRs. Because the main objective of this project is to generate and identify patterns (signatures) in high frequency signals associated with traveling waves, a crucial step in our research was gathering real field data for both the development and testing of the protection scheme. Collecting reliable data from real distribution circuits is particularly challenging because existing current transformers and potential transformers in the field do not have the bandwidth to reliably capture these signatures. Accurate synchronization between sensors is critical because traveling wave signatures propagate at close to the speed of light, and lines in a distribution circuit are significantly shorter than transmission lines. Robust noise rejection is required due to the prevalence of branches, junctions, and electrical interconnects in the circuit that create closely spaced reflections from points of impedance mismatch (Dwivedi and Yu 2011).

As discussed earlier, software-based simulation of the propagation of traveling wave features is both computationally intensive and frequently uses simplified representations of lines and interconnects. For conventional power system dynamics, a hardware-in-the-loop evaluation might have been appropriate, but the bandwidth required to measure and manifest traveling wave signals greatly exceeds the capabilities of the present state-of-the-art, digital real-time simulators that are limited to a time step of 50 μs. At this temporal resolution, most propagation information from traveling waves in distribution lines would be lost. There are special commercially available digital real-time tools to simulate traveling waves in transmission lines, but at the time of this writing, such tools for distribution systems were nascent. Moreover, there are practical challenges in applying fault currents from a digital real-time simulator into a test circuit.

In this project, real field distribution lines (both overhead lines and underground cables) were used as test articles on which we were able to apply faults and gather data. This data could be recorded at a sufficiently high bandwidth to characterize different types of faults and ultimately to develop a protection scheme based on the high-frequency signature of the traveling waves generated from the faults. By decoupling the measurement and simulation aspects of the project, we were able to validate line models and mathematical solvers used for simulation studies with recorded data collected from real distribution lines—filling a gap in the field in the existing theoretical work.

This chapter first discusses the state-of-the-art line emulators along with their limitations in recreating true high-frequency waves generated during a fault. Second, it describes specialized test equipment and tests performed on de-energized circuit proxies. Third, it presents a discussion on the sensing and data acquisitions systems and the results from the tests performed at the Medium-Voltage Outdoor Test Area (MVOTA) facility at ESIF. This experimental setup can be used as a platform for future hardware-in-the-loop experiments on protection schemes involving solid-state power converters and grid-edge PV generation.

Table 6. Commercially Available Distribution Line Emulators

Vendor	Function	Limitations
1	Distribution trainer	Insufficient fault voltage magnitude and Insufficient frequency bandwidth
2	Distribution trainer	Insufficient frequency bandwidth
3	Distribution, transmission, protection and SCADA simulator	Insufficient fault voltage magnitude and Insufficient frequency bandwidth
4	Line impedance simulation network	No fault simulation capability

4.1 Present State of the Art

As a first step, multiple commercial line emulators were compared on the basis of their supported voltage level, power capacity, fault emulation capacity, and sampling bandwidth. Table 6 summarizes the shortcomings we observed with four commercial emulator systems. We also evaluated emulators based on their ability to reliably recreate a fault, and the ensuing traveling waves, and we were not able to find an existing system with this capability. Following our initial review, we approached manufactures of medium-voltage line emulators to assess their willingness to modify or develop custom systems tailored to emulate traveling wave propagation. The requirements for a custom line emulator promulgated among vendors were as follows: The device should permit simultaneous emulation of at least three three-phase lines rated between 480 V and 13.2 kV. The emulator should be capable of emulating multiple faults scenarios, such as SLG, line-to-line, and multiphase-to-ground. The emulated frequency response to current transients with frequency spectra in the kilohertz-to-megahertz range should be validated and accurate. The power level for injected test signals should be at least 20 kVA. In addition, some optional features that would be advantageous to better resolving traveling waves—such as an adjustable line impedance—to model varying distances, the ability to add junctions or branches to simulate reflection effects in radial distribution feeders were also requested.

To make a decision on whether to purchase or build a line simulator with the capability to recreate traveling wave signatures for faults, we also reviewed research done in the field. Accurate fault location in medium-voltage distribution networks is an area of significant research interes and so various procedures for fault location assessment have been evaluated using test hardware or demonstration circuits. A survey of tests and algorithms being considered by industry is presented here ("IEEE Guide for Determining Fault Location on AC Transmission and Distribution Lines" 2015). Some of these methods use fault-originated EMTs, i.e., the traveling waves generated following a fault ((El-Hami et al. 1992), (Borghetti et al. 2006), (Borghetti et al. 2008), (F. Yan et al. 2002), (Yan, Ge, and Zhao 2008)). Zhao et. al. in (Zhao, Qi, and Li 2011) described a digital signal processor-based traveling wave detector that uses power line carrier communications to send information and to mark time. (Vigni et al. 2017) describe a two-end detection system and also employ special high-frequency current transformers with a bandwidth ranging from 500 kHz to 50 MHz. The authors in (Bo, Redfern, and Weller 2000) developed fault transient detector units and connected them to relaying points to capture fault-generated high-frequency transients. They also described ways to use iron core current transformers to extract high-frequency transient signatures.

Some research we reviewed described laboratory emulations of traveling waves. The authors in (Grasselli and Prudenzi 2010) developed a laboratory-scale setup for generating and capturing traveling waves during fault or abnormal operations in a distribution power line at frequencies up to 200 MHz, and the setup was successfully able to capture traveling waves. The authors in (Borghetti et al. 2010) used wavelet decomposition to develop a fault detection scheme using a scaled experimental setup. A $^1/_{50}$ scale model of a feeder was constructed, supplied by an equivalent reduced-scale power supply frequency operating at 3 kHz.

4.2 De-Energized Experiments to Validate Measurement Systems

Our literature review identified that a commonly cited practical consideration in applying traveling wave-based fault localization to distribution systems was the prevalence of multiple junctions and branches in a distribution system that would confound existing localization algorithms. Because uninterrupted segments of cabling in distribution systems tend to be significantly shorter than in transmission systems, experimenters report detrimental effects to the signal-to-noise ratio for traveling wave detection when reflected modes are generated at mismatched points of impedance in the network. Last, spurious traveling waves are commonly observed from switching action or congestion management.

To assess the performance of different sensors and the data acquisition system given these practical considerations, we performed several controlled experiments on de-energized segments of a distribution line by injecting electrical impulses and taking measurements of traveling wave features. We were also able to leverage the Energy Systems Integration Facility's MVOTA distribution line (see Figure 30), which was de-energized and disconnected from upstream and downstream equipment and used to observe propagation velocities of traveling waves and the magnitude of reflected modes emerging from the "open" ends of the line. These reference measurements then served to validate models as a part of our our validation pipeline. The de-energized experiments are described in more detail in the following section.

4.2.1 Commercial Traveling Wave Test System

The project team purchased a commercial secondary pulse injection test set for testing traveling wave fault locators and line protective relays used in transmission systems (SEL-T4287, 2020 (accessed June 30, 2020)). This product is specifically designed to trigger traveling wave fault locators and protection elements that measure relative polarities and rise times in currents and voltages over a time interval of 1 μs. The commercial device generates output current signals with the required nanosecond precision triggers, rise time, and adequately slow decay, which are common in traveling waves found in transmission lines. We used this setup for our initial de-energized field-testing. The test signals generated from this apparatus could be applied to an actual line, a line emulator, or directly to a protective relay. The device creates two sets of three-phase currents spaced in time to simulate a secondary traveling wave. An optional voltage module accessory (low-inductance shunt) could be used if voltage triggers are preferred. As an initial test of our measurement system, the equipment was used to inject a pulse into a 200 $m\Omega$ resistor to capture the current pulse waveform (see Figure 29). A digitized representation of this test waveform was used as the input fault signature for software simulations using EMTP.

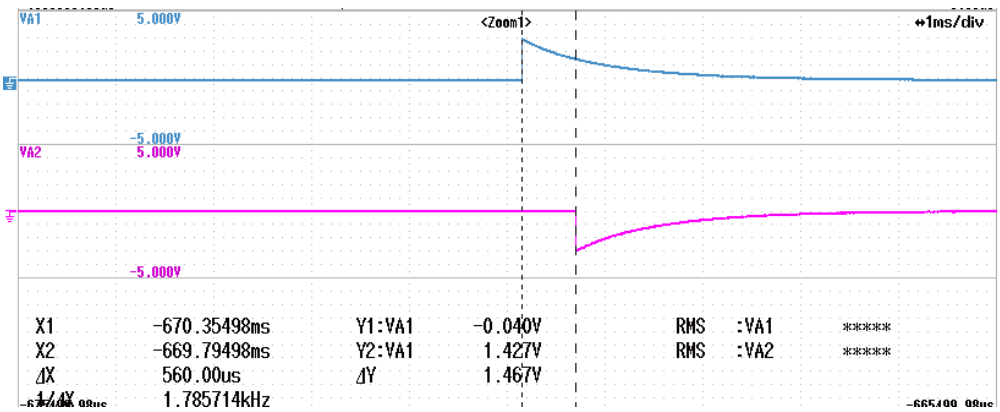

Figure 29. Waveform of the voltage across and current injected from the T4287 equipment into a 200 $m\Omega$ resistor.

After initial validation testing, multiple test cases were executed on the MVOTA. This area features a 13.8-kV test distribution line (see Figure 30) comprising a three phase link of 2 AWG Sparrow steel-reinforced aluminum conductors. Dimensions and specifications of this segment of distribution line—including the elevation of lines and the spacing between lines—were measured and included in the software model of the system to maximize consistency of our simulation studies.

Test Case 1: The first test case was to inject a current pulse in the MVOTA distribution line with both ends of the line grounded. The current pulse was injected into a conductor loop with one of the injector leads closer to the line end. The second injector lead was installed at the middle of the line. The schematic of the test setup is shown in Figure 31. Two terminals of the commercial traveling wave injector were connected in parallel to inject a current pulse with peak of 8 A. Currents from the injection system were split into fractions flowing through the loop and a out of the loop directly into the grounded termination. Both fractional currents were measured. Figure 32 shows the waveforms of the currents in the line and discharged through the ground cable in blue and pink, respectively.

Test Case 2: In this test, the current pulse was injected at the same location as Test Case 1, except both the ends of the distribution line were left ungrounded (see Figure 33). This test was done to ensure that there were no spurious current paths within the insulation and termination hardware. The waveform of the current traveling through the loop (blue) is shown in Figure 34. The discharge current fraction (pink) was measured to be close to zero and this confirms that the the current path was fully closed within the loop.

Next, we performed a control experiment to observe traveling wave voltage features on a RIGOL MSO2072A oscilloscope at ESIF. Figure 35 shows the test setup for the direct injection test with a single span of 106.7 m (350 ft) of the 2 AWG conductor. The commercial test system was ill-suited to inducing clearly detectable traveling wave features in this short conductor span because the rise time, fall time, and the pulse width injected by the test system

Figure 30. The Energy Systems Integration Facility's MVOTA used for tests.

are preset and cannot be configured; and the period of the injected signal greatly exceeds the propagation time for the cable being tested. A Tektronix 3390 Arbitrary Waveform/Function Generator was used in place of this commercially available test system to create a voltage impulse that would, in theory, be easier to resolve. Here, we encountered some practical limitations to coupling an energy-limited signal source to the section of distribution cable. We observed that parasitic dissipation effects along the length of the cable significantly attenuated the applied impulse to a point where no detectable pulse feature was observed on the oscilloscope.

We then repeated this experiment using a 45.7 m (150 ft) span of RG223 coaxial cable and a similar length of 2 AWG bare conductor. Both cables were tested in a setup shown in Figure 36 comprising a Tektronix 3390 Arbitrary Waveform/Function Generator and a RIGOL MSO2072A oscilloscope. The Arbitrary Waveform/Function Generator was configured to generate a 4 Volt impulse with a rise time of 5 ns and a pulse width of 20 ns. The voltage impulse was realized by a 14-bit, 125×10^6 samples/second digital to analog converter. This impulse was applied to one end of the cable being tested, and reflected modes of this impulse were recorded in time using the oscilloscope. The oscilloscope was configured to sample the signal at the rate of 1×10^9 samples/second with a channel-to-channel skew rated to be under 2 ns.

Oscilloscope displays observed when pulses were injected into the RG223 cable with both open and shorted termination are shown in Figure 37 (a) and Figure 37 (b) respectively. As theoretically expected, the reflections from the open termination retain the polarity of the injected pulse, whereas reflections from the shorted termination have reversed polarity. Another important artifact noticed from this experiment is that interconnection hardware used for the experiment often introduce unique signatures to the reflection. For instance, using banana jack connectors resulted in a bimodal reflections, as shown in Figure 38.

The above experiment was repeated with a 2 AWG bare conductor in place of the RG223 cable. The resulting oscilloscope display is shown in Figure 39 (a).

Intuitively, the time taken for a reflection to return to the point of injection is a directly related to the length of the conductor ($t_{reflection} = \frac{2 \cdot l}{c}$). Assuming that the wavefront propagates at the speed of light $c = 3 \times 10^8$ m/s and the total

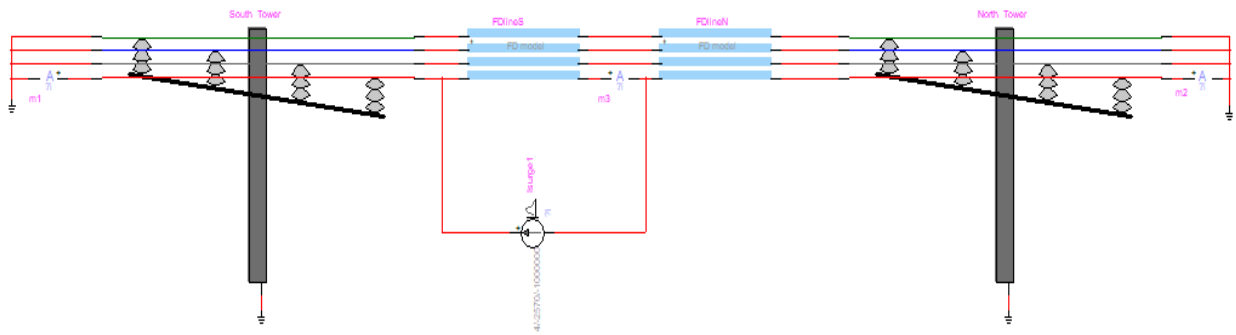

Figure 31. Test setup (MVOTA) schematic for Test Case 1

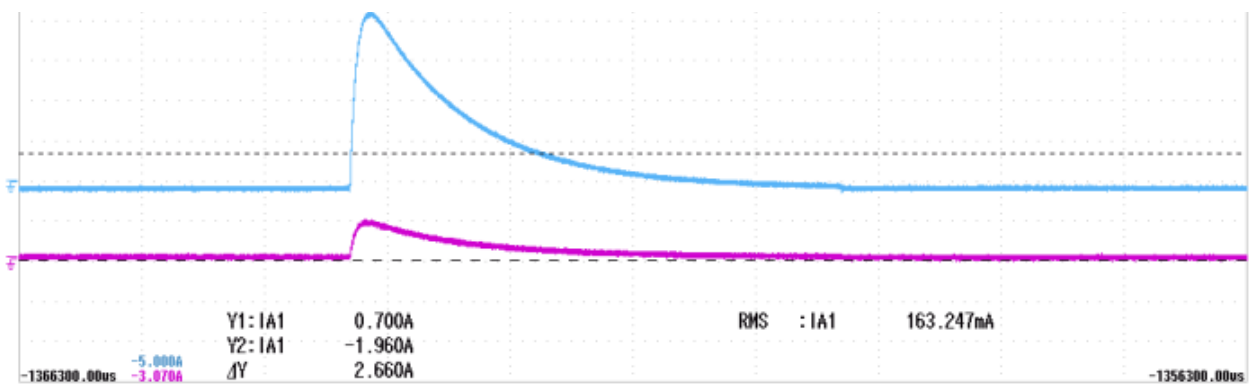

Figure 32. Current waveform for current traveling in the cable and into the ground for Test Case 1

length of the cable under test $l = 3.04$ m then $t_{reflection} = 20.26 \times 10^{-9}$ s, which is close to 23.13×10^{-9} s observed on the oscilloscope. As verification of the conservation of group velocities in a traveling wave, the pulse width of the injected pulse was increased to 80 ns, and the experiment was repeated. As expected, the leading edge of the reflected impulse was observed at the point of injection in 23.13×10^{-9} s, as seen in Figure 39 (b).

In order to mitigate coupling effects related impedance mismatch between the impulse generator and the conductor being tested, future tests used electromagnetic pulse injection instead of an electrical connection.

4.2.2 Electromagnetic Pulse Injection and Validation Experiments

Given the challenges in inducing electrical impulses of sufficient magnitude and quality, we proceeded to generating voltage impulses by modulating a magnetic field with a high-frequency current signal. This section outlines our efforts to induce a voltage in a test circuit and to and observe the traveling wave signatures. A preliminary test setup is shown in Figure 40 (b), and three different bobbins used for the tests are shown in Figure 40 (a). Table 7 provides the details of the bobbins—including the number of winding turns, the number of layers, the length of the winding, and the external diameter of the bobbin—because all these attributes affect the strength of the resultant magnetic field. The cable under test is 2 AWG, similar to the conductor used in the MVOTA. To perform these preliminary tests, we used the commercially available test system to produce a current impulse with a 1 μs-rise time and a halfway decay time of 389 μs, and this current impulse was passed through each of the three bobbins in turn to observe the induced voltage signal in the conductor being tested. Tests were repeated with both open and grounded terminals at the end of the conductor.

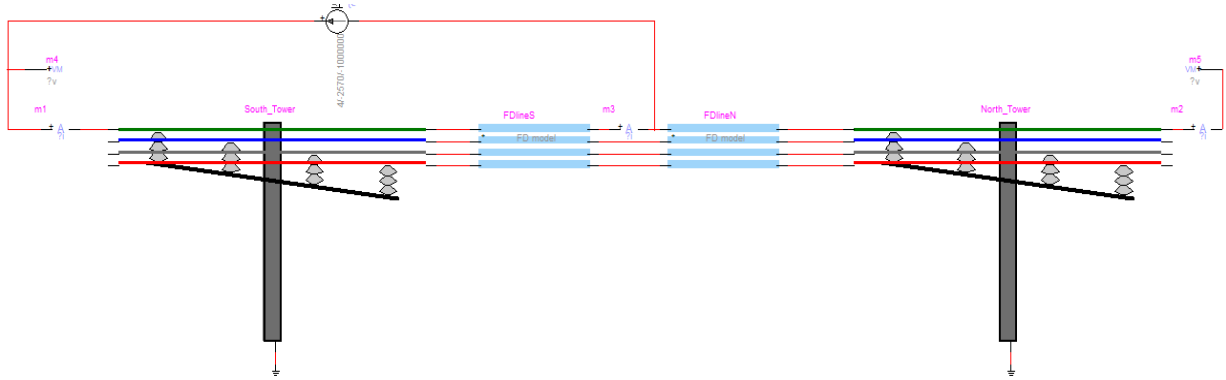

Figure 33. Test setup (MVOTA) schematic for Test Case 2

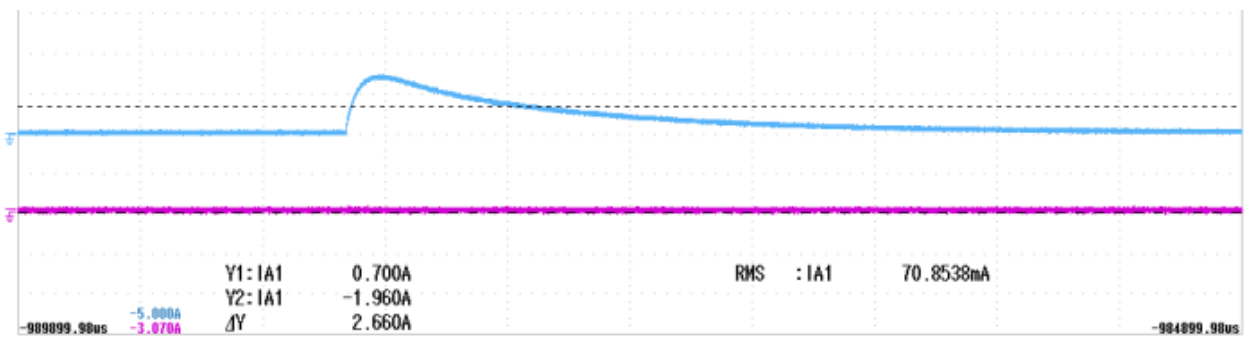

Figure 34. Current waveform for current traveling in the cable and into the ground for Test Case 2

Figure 41 shows some of our observations, with the current injected from the commercially available traveling wave test system displayed in red, the voltage across the bobbin wound coil in blue, and the induced voltage with reference to the ground shown in orange and pink. The system acquiring data is able to sample at a "high" and "low" rate, corresponding to the orange and pink marker colors, respectively. Figures 41(a) and (b) use a timescale of 10 ms/div, whereas Figure 41(c) shows a smaller window of time, with a resolution of 500 μs/div. Clearly, a voltage impulse was injected using this test system; however, no traveling waves or reflected wave features can be observed. The figure also shows some of the artifacts resulting from the use of the commercially available traveling wave injector, including a burst of noise 4 ms after the current pulse is injected. The manufacturer of the commercial test system reports that this anomaly may be caused by an internal capacitor being discharged after an impulse event. Also, it is important to note that there is significant background electromagnetic interference in the data. This interference appears to be correlated

Table 7. Details of the Bobbin Used for the Test

Attributes	Bobbin I	Bobbin II	Bobbin III
Number of layers	2	5	14
Total number of turns	95	100	250
Wire gauge	AWG 12	AWG 18	AWG 22
External diameter of the bobbin (d)	3 cm	2.6 cm	1.8 cm
Length of the winding (l)	19 cm	5.7 cm	8.5 cm

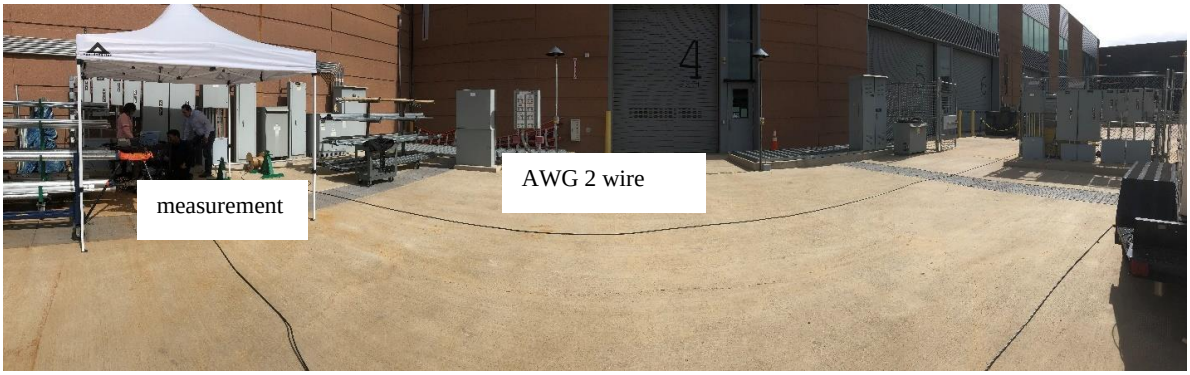

Figure 35. Test setup for the direct injection test with the 350-ft AWG 2-wire at ESIF

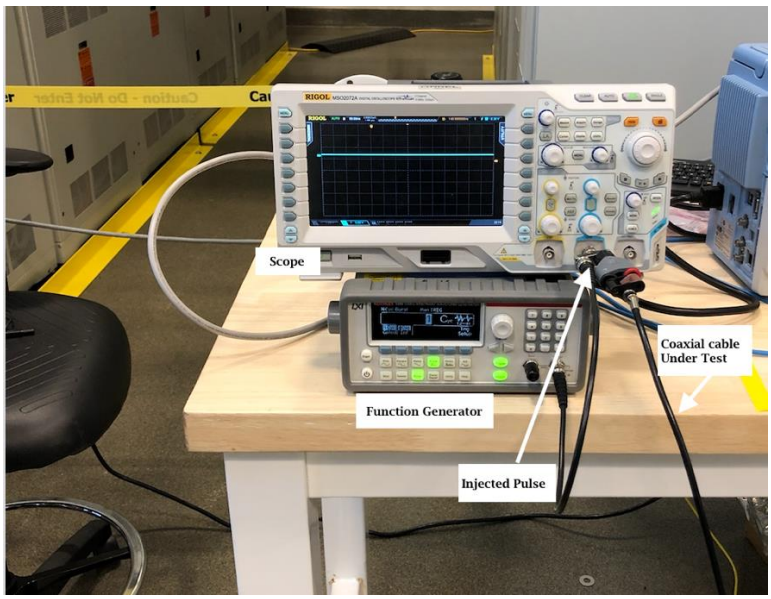

Figure 36. Direct pulse injection setup with coaxial cable

with the presence and operation of other high-power equipment in the vicinity of this experimental setup. We can see from the plots that the magnitude of the induced voltage is lowest for Case a, whereas it is maximum in Case c. These results are consistent with the theory that the voltage magnitude is a function of the number of turns and confinement of the magnetic field. (Bobbin III has the highest number of tuns and is placed very close to the cable under test, with d of 1.8 cm.)

Custom-Designed Electromagnetic Impulse Injector

As described earlier, a stated goal of the project is to reliably inject impulses into the circuit being tested, as illustrated in Figure 42. The circuits being tested include the MVOTA at NREL and distribution test facilities under a controlled environment. Reliable impulse injection across this diverse range of test circuits poses several challenges. The obvious challenge is that the nominal impedance of the circuit is not known (in the wideband sense) a priori. Consequently, it is very difficult to match the output impedance of an impulse generation circuit to the apparent impedance of the test circuit at the point of injection. An impedance mismatch at this point would result in artifacts induced by the interconnection point. Traveling waves are particularly vulnerable to these mismatches because they not only alter the propagation characteristics of the line but also could induce spurious reflected wave fronts that would be severely

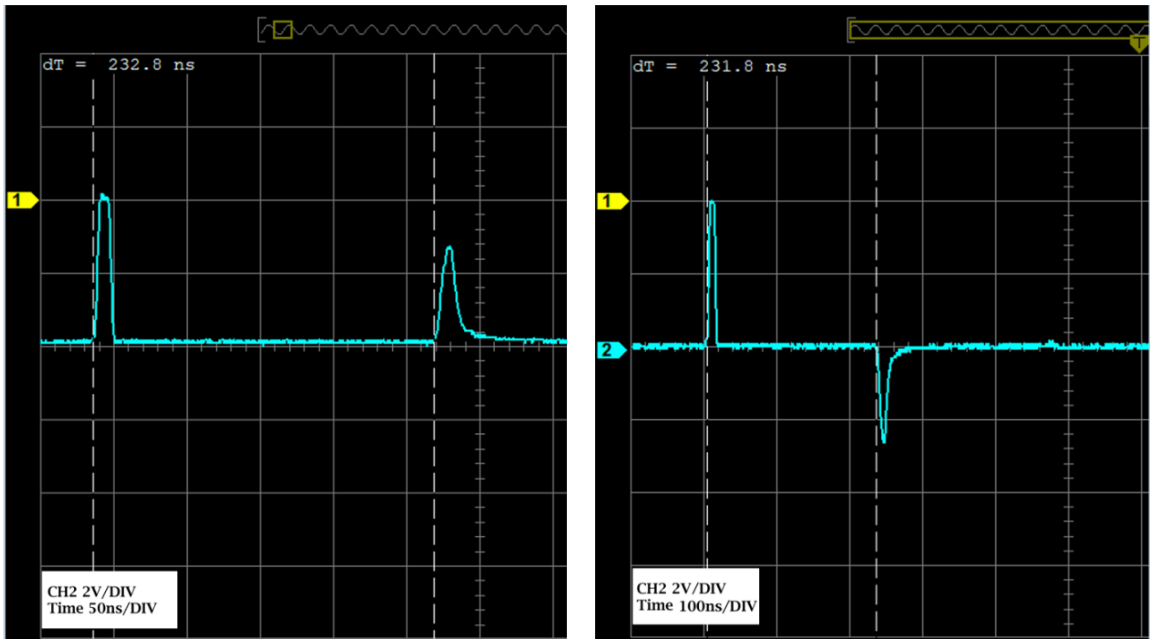

(a) (b)

Figure 37. Reflections observed with (a) open-end termination and (b) short-circuit termination

detrimental to any fault-localization algorithm.

As shown in Figure 42, an ideal impulse injection circuit would apply a desired impulse signature at a specified time, T, to a segment of line being tested. The impulse would be transmitted along the line at the speed determined by the propagation constants of the line (as considered in the line model) and reflected by line terminations and discontinuities modeled in the topology model. If the impulse signature resembled an ideal discrete impulse over the interval ΔT bearing the temperate distribution, $\delta_T(t) = 0 \sim \forall t \notin [T, T+\Delta T]$, we gain several analytical benefits when recovering model parameters from the data collected. The primary benefit is that the impulse has an analytical Fourier transform and can be factored for analyses performed in the frequency domain. The impulse function also offers some testing benefits because the convolution of the impulse function with a function representing the line model effectively time shifts the transfer function, $(f * \delta_T)(t) = f(t-T)$. This property is essential for accurate traveling wave measurements that are sensitive to timing uncertainties and require precise time alignment of sampled data to the impulse injection time. Because the power and phase spectrum of the impulse is constant for all the valid frequencies in the interval $[0, \frac{1}{2\Delta T}]$, there are signal-quality improvements associated with reducing ΔT as well. Minimizing ΔT would maximize the sampling bandwidth for the data acquisition system over the range where artifacts associated with the impulse could be ignored. As mentioned earlier in this document, the sampling rates desired for our work are in the order of tens of megahertz to measure impulse duration with order of a few nanoseconds.

These specifications rule out the use of conventional arbitrary function generators to apply a voltage impulse. Even with impedance matching and impulse width considerations aside, a conventional digital voltage source has an output impedance significantly larger than the systems being tested; consequently, the voltage amplitude induced is greatly reduced, directly curtailing the signal-to-noise ratio of the resulting traveling waves.

To address these concerns, our approach is to induce a voltage transient in the system being tested by subjecting it to a rapidly changing magnetic field. Following Faraday's law, we know that the voltage induced in a conductor is proportional to the rate of change in the magnetic field, (ϕ), incident on it, $\varepsilon = -\alpha \frac{d\phi}{dt}$. Critically, the voltage magnitude of the induced electromotive force (EMF) (ε) is not dependent on the electrical parameters of the line. The magnetic field, in turn, is generated using a Helmholtz coil (DeTroye and Chase 1994). The setup comprises of two

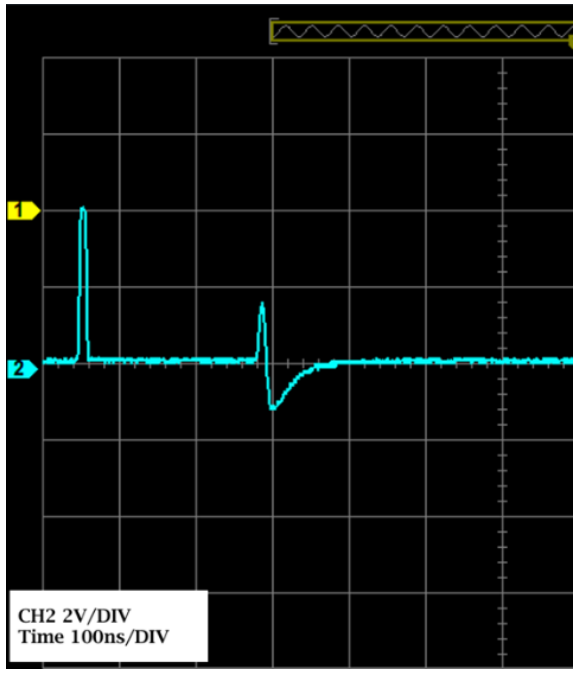

Figure 38. Reflections observed with coaxial cable with banana jack connectors.

circular magnetic coils placed along a common diametrical axis and parallel to one another. The line or conductor being tested is placed in a gap maintained between the two coils, as illustrated in Figure 43. Each coil carries currents that are equal magnitude and direction, producing a magnetic field of the same sense. The Helmholtz arrangement governs the chosen coil diameter and spacing to produce a uniform magnetic field across the cross section of the coil while ensuring that the field lines are parallel across the gap. This configuration reduces the sensitivity of the impulse injection system to changes in alignment of the line or conductor being tested. This feature is of particular importance given the need to test systems in the field, where precise alignment is not possible, as noted in the test installation in Figure 45b. The magnetic coils were wound around a ferromagnetic core to improve flux concentration through the conductor being tested. The core was further optimized to ensure that the magnetic field lines were directed to the center of the conductor being tested. This feature was necessary to support conductors of varying diameter and design. The core spacing could be adjusted in the field to manually optimize the setup, if needed.

We would also like $\varepsilon(t)$ to approach $\delta(t)$. For this, we also need to maximize $\frac{d\phi}{dt}$, where $\phi(t) = \frac{8\mu_0 NAi(t)}{\sqrt{125}R}$. Note that the coil design lends us direct control over $\frac{d\phi}{dt}$ by generating a current impulse, $\frac{di}{dt}$, meeting the desired properties. Also note that the gain of the magnetic field generator is a function of the ratio $\frac{\mu_0 NA}{R}$. This key design parameter can be maximized by increasing the cross-section diameter of the windings, the number of turns, and the permeability of the magnetic circuit while at the same time minimizing the resistance of the windings. These specifications are achieved in our design by constructing the winding around a ferromagnetic core and by using tightly wound, lacquer-insulated copper wire. The windings are potted in a thermally conductive epoxy and encased in a heat sink can. This design is optimized to accommodate short impulses of large current with a focus on thermal dissipation.

To generate the current impulse of the desired properties, we use a series-resonant impulse generator using a Hewlett-Packard 8114A 100-V Pulse Generator with appropriately tuned coupling parameters to ensure our ideal case, where $\varepsilon(t)$ induced in the conductor under test approaches the properties of $\delta(t)$. Figure 44 shows a plot of $\varepsilon(t)$ induced in an isotropic test medium. Note that the width of the impulse is 30 ns, which is significantly narrower than the prior methods using the commercial test apparatus or the arbitrary function generator. The direct advantage offered by this narrow pulse is that traveling waves emerging from this impulse can be safely sampled at a rate $\leq 33MHz$, which meets the sampling rate desired for analysis.

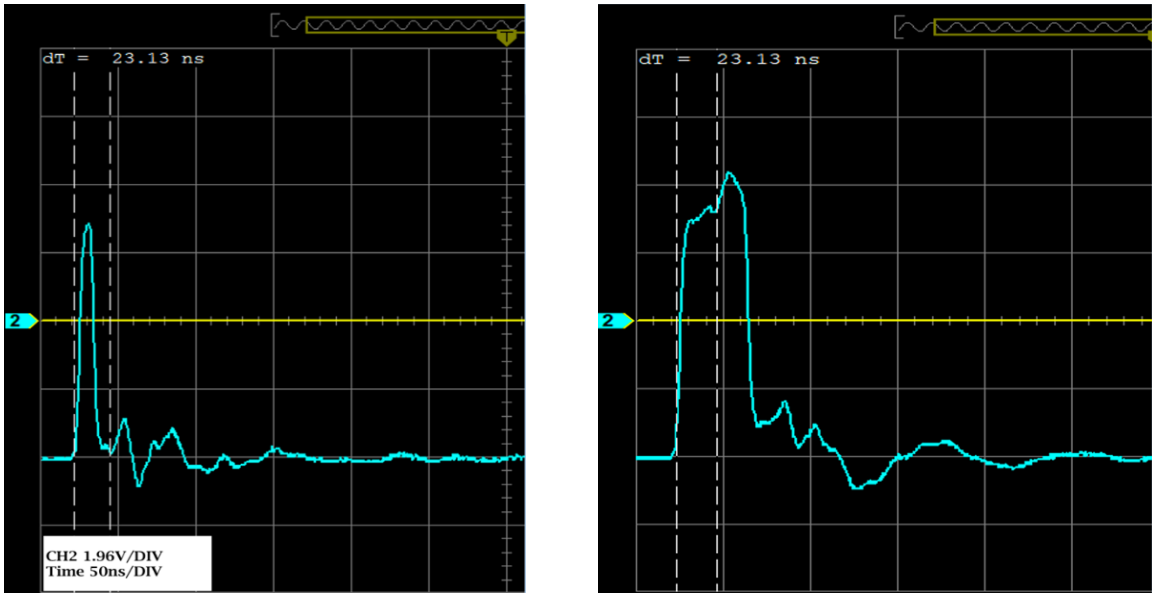

(a) (b)

Figure 39. Reflections observed with 10-ft bare conductor and the signal generator (a) pulse width of 20 ns and (b) pulse width of 80 ns

Electromagnetic impulse test

The first field test of the impulse generator was to induce an impulse in an overhead section of 2 AWG Sparrow conductor located at NREL. This section of cable is 11.5-m long, which means that the impulses traverse the length of this cable on the order of several nanoseconds. The propagation time constant for this cable poses a measurement challenge but also requires near-ideal impulse injection. The injector described was used for a preliminary test on the MVOTA cable, with due fixturing, isolation, and alignment as illustrated in Figure 45 (a) & (b). Note that the pair of coils in the figures are on an adjustable frame that allowed us to reset the field geometry to maximize α.

This test was conducted after ensuring that the MVOTA was de-energized with the line terminations left open. All the impulse injection equipment could therefore be lifted to the line on a scissor lift and installed safely. Impulses were injected into the cable at 3 m from one end, and measurement probes were placed 1 m from either side of the injection point and were connected to a single logging oscilloscope with leads of equal length. As shown in Figure 46, a clearly resolved traveling wave was captured by the logging oscilloscope. Note that after the initiated impulse, the electromagnetic injector system is electrically isolated from the the test circuit. This electrical isolation from the circuit being tested results in an uncorrupted traveling wave feature, where the only reflections are from the open terminations on either end of the cable. The test also showed 24 clearly detectable peaks resonant at two times the length of the cable, providing ample data for a localization algorithm to detect the phase relationship between the two recorded channels. Also observable in the data are subpeaks in the waveform consistent with the spacing of bushings and couplings close to the cable termination point. These preliminary tests support the hypothesis, and our injection scheme seems to provide accurate impulses with minimal interaction with propagating traveling waves. A new version of this setup—featuring coils with faster response time–will be used in future tests.

Identifying Propogation Parameters for the MVOTA

Following the results shown in Figure 46, we wanted to model the traveling waves observed in the impulse test in a software simulation (using EMTP). This validation exercise required us to retrieve the wideband model parameters for the 2 AWG Sparrow conductor in the MVOTA. We performed a four-port impedance measurement of the MVOTA line over a range of frequencies. This task focused on the interval between $10^3 - 10^6$ Hz as being a practical range for instrumentation used to measure fault signatures in the field. The instrument used to make wideband impedance mea-

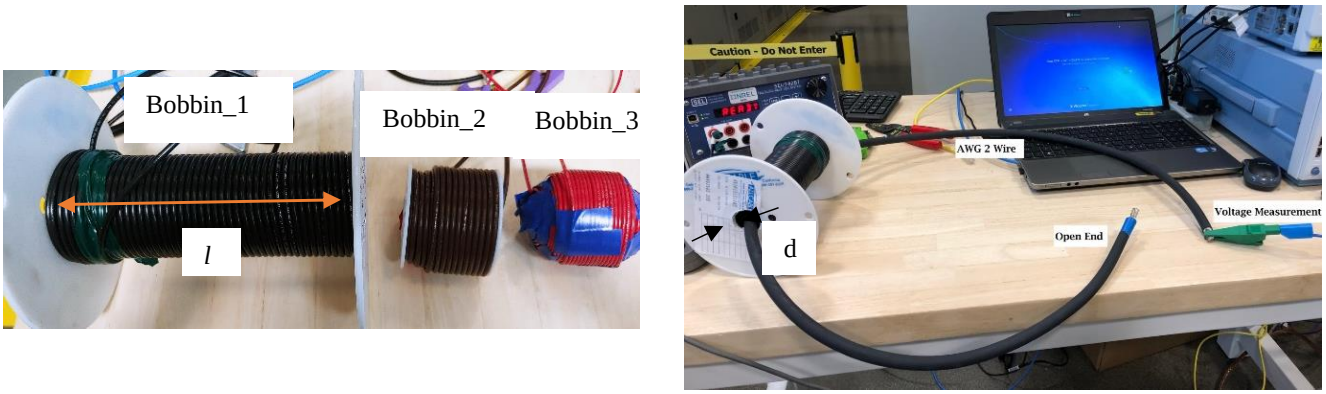

Figure 40. (a) Bobbin structure and (b) experimental setup with bobbin for the electromagnetic injection

surements was an Agilent 4284A Precision LCR meter (Hewlett-Packard 1991) with software controls for averaging and automation. The 4284A LCR meter has a base accuracy of 0.05% over test frequencies ranging from 20 Hz to 1 MHz, and is able to resolve signal amplitudes above 5 mV and 50 μA.

The MVOTA uses a short length of distribution line segment, so the ability to estimate impedance at currents as low as 50 μA is particularly helpful. The measurement circuit used to make impedance measurements is comprised of a signal source, a voltmeter, and an I-V converter (see Figure 47(a)). Vector measurements of (magnitude and phase) of the voltage drop (V_x) and branch current (I_x) thus obtained were averaged over an acquisition window until a stable impedance measurement was obtained. Stability in this case was established by comparing the measurement variance to the base uncertainty of the device.

Additional design considerations employed to reduce uncertainty include the use of a trans-conductance amplifier based I-V converter to minimize the series impedance of the current measurement circuit. Here, V_r serves as a proxy measurement for branch current I_x. The impedance of the MVOTA line segment is thus a function of two voltage measurements made in relation to an internal voltage reference. Pre-test calibration is performed to determine R_r and fixture impedance quantities.

The fixture design for the MVOTA experiment is an important factor particularly because the MVOTA is several feet overhead and over 15 meters of test leads were needed in order to perform the measurement. To minimize the impact of test leads, contact resistances, and fixtures, a four-terminal measurement configuration was used for all measurements. In the four-terminal setup, one pair of leads measures voltage, and an independent set of leads measures current minimizing the impact of fixture impedance on the measurement (see Figure 47(b)).

In conjunction with guarding, stray capacitance was manually compensated using open-lead measurements, and contact resistance effects were compensated using a shorted-lead measurement. Figure 48 shows the impedance of the MVOTA (Z, θ) measured from 10^4 Hz to 10^6 Hz. The figure demonstrates one of the complexities in frequency-dependent line models, which is that the impedance regime of the circuit is not constant across a range of frequencies. We see that at 10^5 Hz and greater, the series-inductive elements in the line become dominant, resulting in a positive slope for $|Z|$ with respect to frequency. At 70×10^4 Hz and greater, shunt capacitance effects are observed to be dominant. The figure presents a qualitative appreciation for the behavior of a line segment, and further analysis is needed to extract usable quantitative parameters from these data. Circuit theory suggests that the positive and negative slopes observed for $|Z|$ should be ωL and $\frac{1}{\omega C}$, respectively. The impedance analysis shows a maxima at $\approx$0.7 MHz, which is consistent with the resonant frequency observed in the impulse experiments.

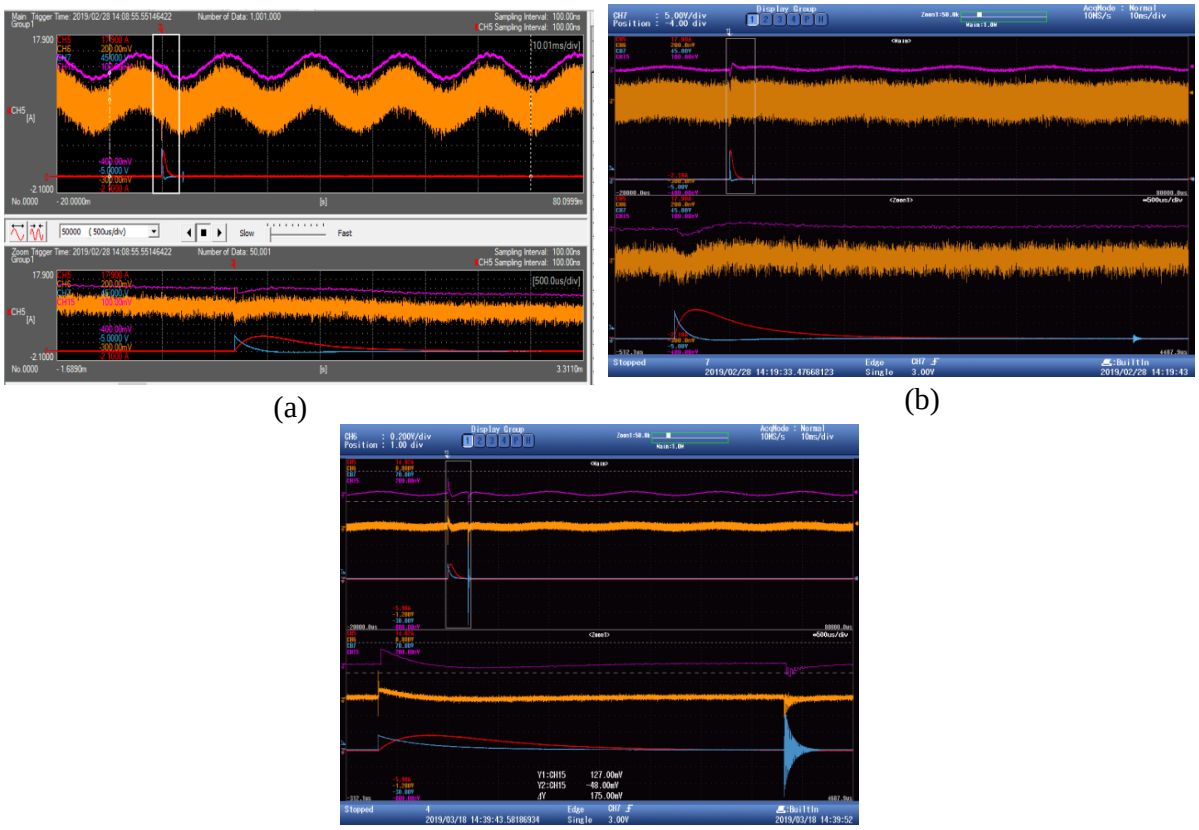

(a) (b) (c)

Figure 41. Measurements showing current injected from commercially available traveling wave test system (red, 2 A/div), voltage across the winding (blue, 5 V/div), and induced voltage across the cable under test and the ground (orange: high-frequency acquisition, pink: low-frequency acquisition, 50 mV/div)

Identifying Model Parameters for the Line-Length Simulator

Because a stated objective of the project is to replicate traveling wave phenomena in a line-length simulator—or at least to show the limitations in doing so—we also measured the wideband impedance of a Spitzenberger & Spies line-length simulator available at NREL. This device engages analog the resistor-inductor circuit elements to reproduce the desired circuit topology. Although validated by the manufacturer at near-nominal system frequencies (≈60 Hz), we characterized it in a wideband manner to compare it to the characterization of the MVOTA.

We reproduced the experiment performed on the MVOTA using an auto-balancing bridge impedance measurement and a four-terminal fixture. Our observations demonstrate the value of a fully programmable impedance network. Note that the behavior of the line simulator at low frequencies (as shown in Figure 49) is close to the ideal response for an resistor-inductor circuit.

At higher frequencies, however, the simulator response is subject to practical considerations that pose a challenge to reproducing traveling waves observed in real circuits, such as the MVOTA. Observe the impedance artifacts related to the parasitic capacitances in the simulator cabling shown in Figure 50. This figure shows the behavior of the Spitzenberger & Spies simulator across the same range of frequencies used to characterize the MVOTA. Here, we see essentially an resistor-inductor circuit element but with a notch resonance at 400 kHz, and we theorize that this self-resonance is likely caused by the parasitic capacitance inside the simulator. If this simulator were used to propagate impulse signatures (with broadband spectra), clearly this self-resonant mode would be excited, causing ringing in the circuit that would be completely spurious. Without compensation for this resonant mode, the simulator can only be

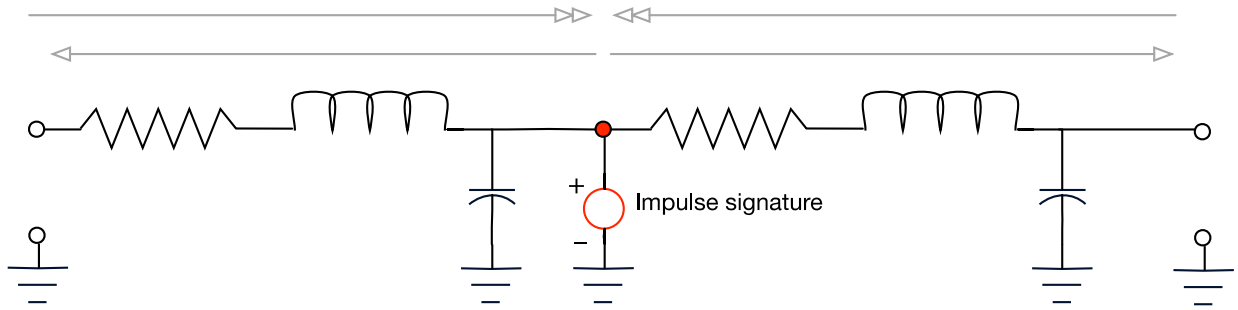

Figure 42. Schematic overview of a desired impulse injection system. Here, the impulse signatures are induced on a test circuit (a segment of electrical conductor), allowing them to propagate and interact with circuit junctions and fault sites without significant contamination from coupling and signal generation artifacts from the test apparatus.

used for systems where the propagation time is greater than 5 μs.

One goal in this task was to assess the bandwidth and capability of the sensors as well as the data acquisition system to capture the high-frequency traveling wave signatures. Multiple current transformers, potential transformers, and acquisition systems were selected and purchased for this project that meet the desired frequency bandwidth in the order of 10^6 Hz however these components may not be the best suited for the task nor endorsed by the project team and so are not individually identified in this report.

4.3 Fault Experiments at Medium Voltage

This chapter has thus far discussed simple experiments and de-energized experiments to show traveling waves in different mediums. This section presents the medium-voltage test setup that was used to run fault experiments and the sensing devices used to capture traveling waves. The current transformers identified earlier in this chapter were used in the outdoor experimental setup where the faults were applied. The results from the experiments performed at medium voltage is shown in Chapter 7.

4.3.1 Experimental Setup at Medium-Voltage Used for Fault Experiments

Figure 51 and Figure 52 show the experimental setup used for the medium-voltage fault experiments. The setup has five segments of underground cables and four segments of overhead lines. Table 8 shows the length of the line sections. The tower configurations and underground cable configurations are not provided here to protect NREL's intellectual property, but the length of the lines and cables should provide adequate information for the study presented here. There are potential impedance mismatches in the overhead line and the underground cable setup. These are also identified in Figure 51 and Figure 52. The figures also identify the potential impedance mismatch in the system. Two sets of current transformers were used in both Location 1 and Location 2 to show that the traveling waves captured are not a result of experimental artifact. The experiments were run more than once to create repeatable results.

The key difference between the experimental Setup 1 and experimental Setup 2 is the use of a bypass between UL2 and UL4 in Setup 2. A second set of current transformers was used in Location 2 (at the bypass) to capture traveling waves in this additional location.

Figure 53 and Figure 54 show the time taken by the fault-induced traveling waves from the fault location in the overhead lines and underground cables. Because the exact configuration of the underground cables were unknown, a maximum speed of 60% of the speed of light and a minimum of 50% of the speed of light were assumed for the speed of the traveling waves in the underground cables based on prior modeling results.

Figure 55 shows the fault contactors that connect the overhead line to the ground. Figure 56 shows the use of current transformers over the conductor. Figure 57 shows the connection from the current transformers to the oscilloscope.

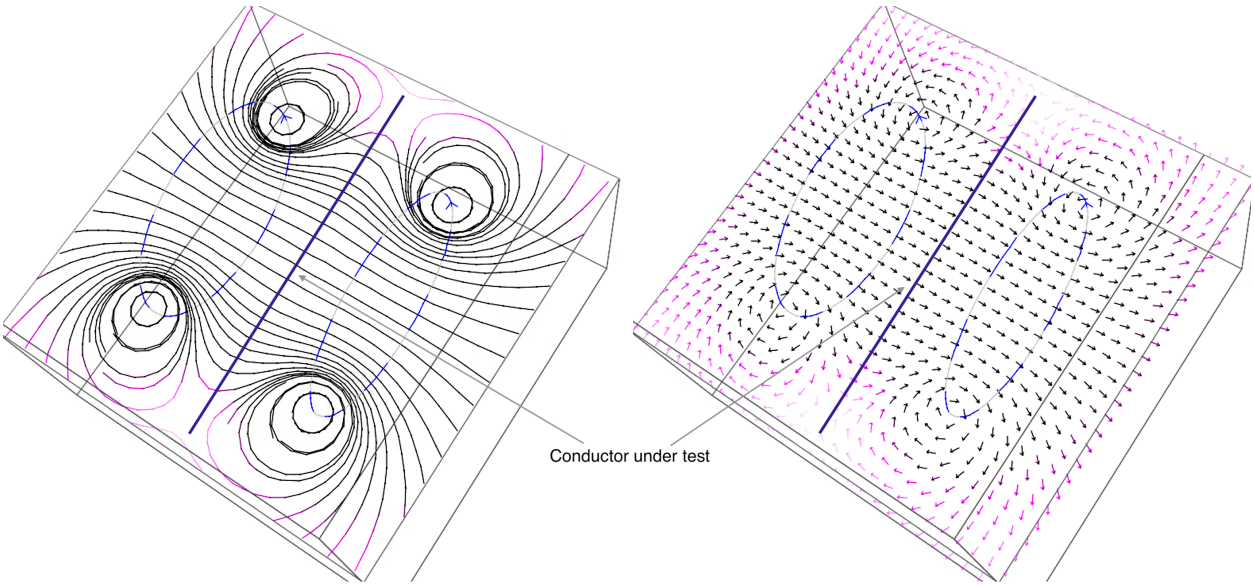

Figure 43. The figures on the left and right illustrate the parallel magnetic field lines and uniform vectors respectively of the magnetic field produced when the diameters of the coils are equal to their spacing.

Figure 58 shows the bypass at Location 2 where the second set of current transformers were connected to measure the traveling waves.

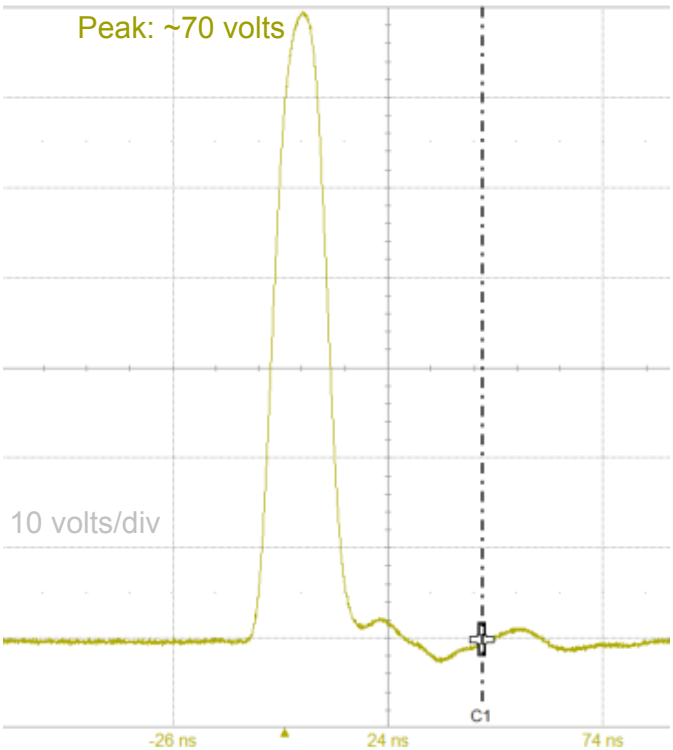

Figure 44. Induced voltage in isotropic media. Note that the induced electrical impulse (measured in volts) is less than 2 ns in width with minimal ringing after the initial excitation.

(a) Electromagnetic impulse injector mounted on a non-magnetic fixture showing a cable under test.

(b) The injector and fixture assembly attached to the MVOTA.

Figure 45. Impulse injector experiments at the Energy Systems Integration Facility

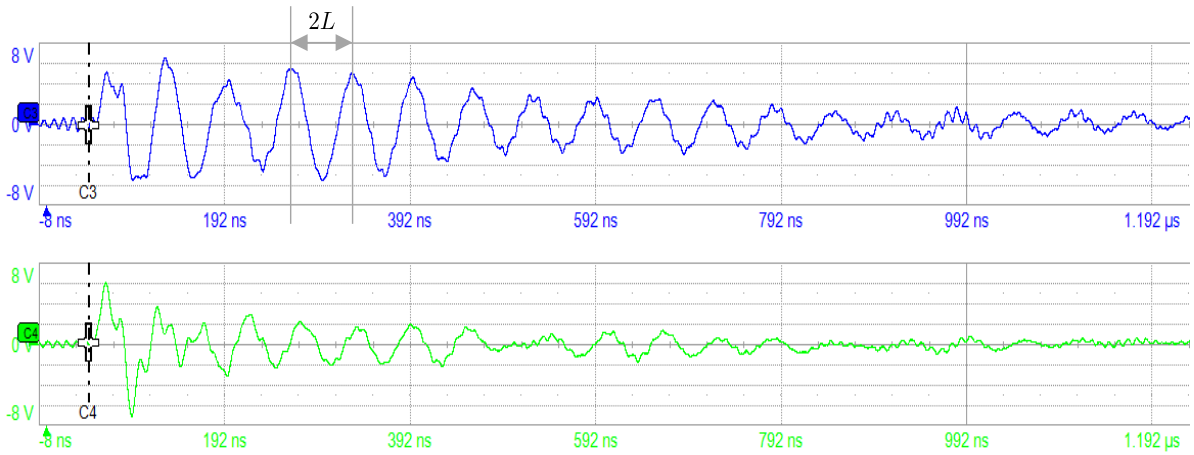

Figure 46. Oscillography from two probes placed 2 m apart. An impulse was applied at $t = 0$ producing close to $1.5\ \mu s$ of perceptible traveling waves.

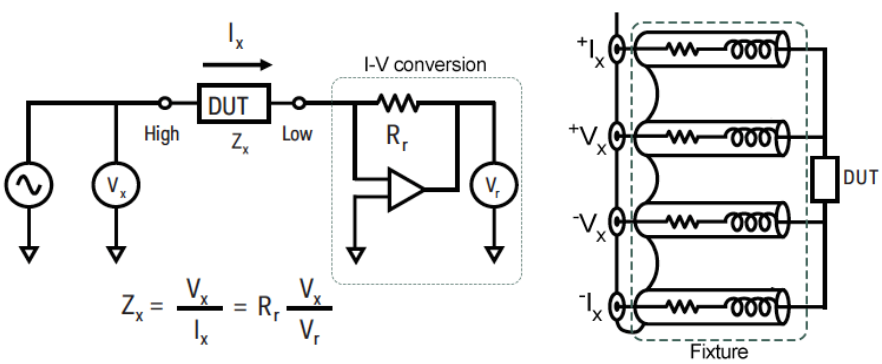

(a) Simplified schematic showing the impedance measurement circuit.

(b) Schematic diagram showing a 4T measurement setup.

Figure 47. Wideband impedance measurement of the MVOTA was conducted using the four-terminal impedance measurement technique. This schematic was adapted from an application note in (Hewlett-Packard 1991).

Table 8. Details of the bobbin used for the test

Length of Line Segment	Experimental Setup 1	Experimental Setup 2
UL1	610 m	610 m
UL2	80 m	80 m
UL3	50 m	1 m
UL4	400 m	400 m
UL5	160 m	160 m
OH6	211 m	211 m
OH7	43 m	43 m
OH8	8 m	8 m
OH9	1 m	1 m

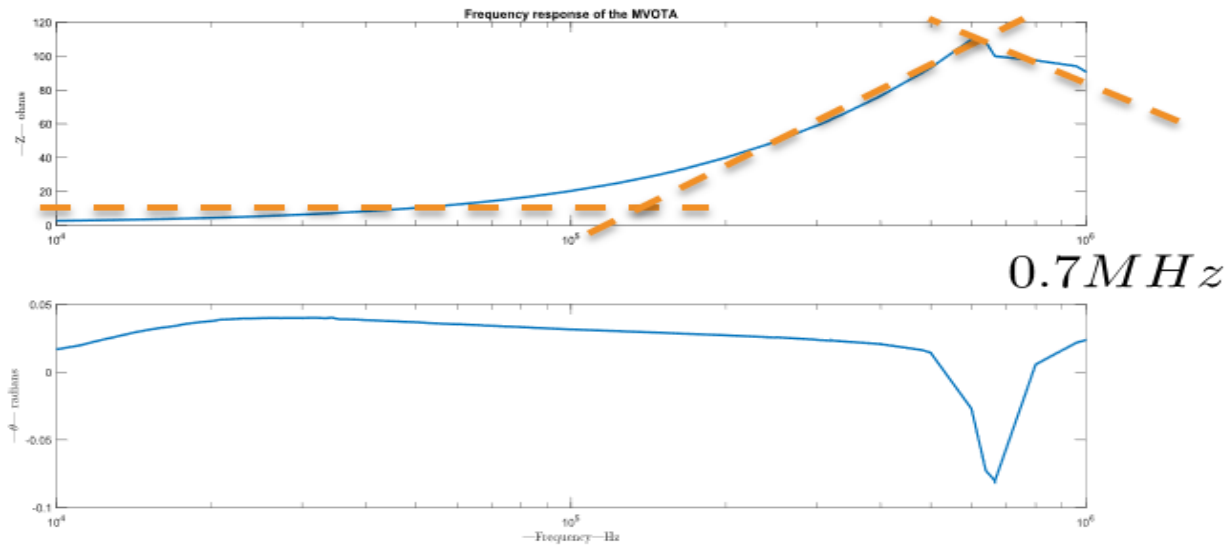

Figure 48. Preliminary results showing the circuit parameters ($|Z|$ (Ohms) and $\angle Z$ (Radians)) of the MVOTA line across the frequency range of interest.

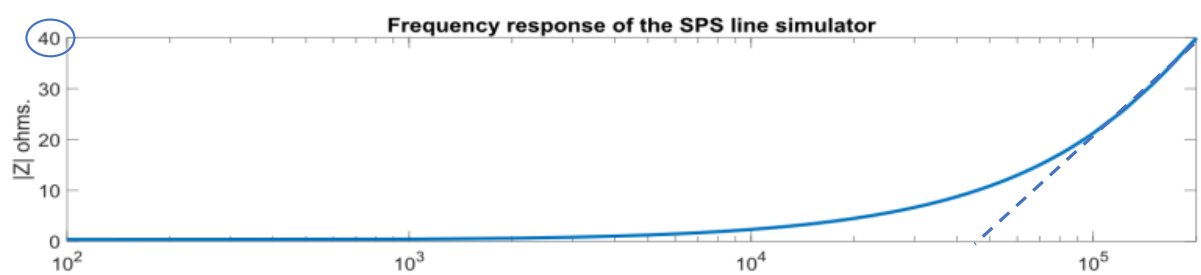

Figure 49. Impedance ($|Z|$ (Ohms))of the Spitzenberger & Spies line simulator showing a near-ideal response for an resistor-inductor circuit up to 10^4 Hz.

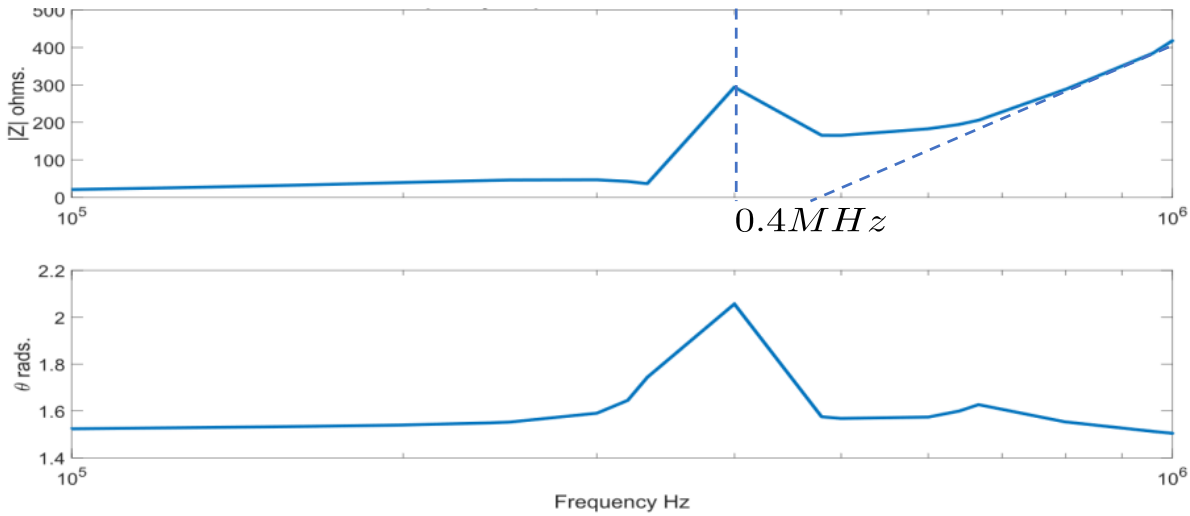

Figure 50. Impedance ($|Z|$ (Ohms) and $\angle Z$ (Radians)) of the Spitzenberger & Spies simulator measured up to 1 MHz

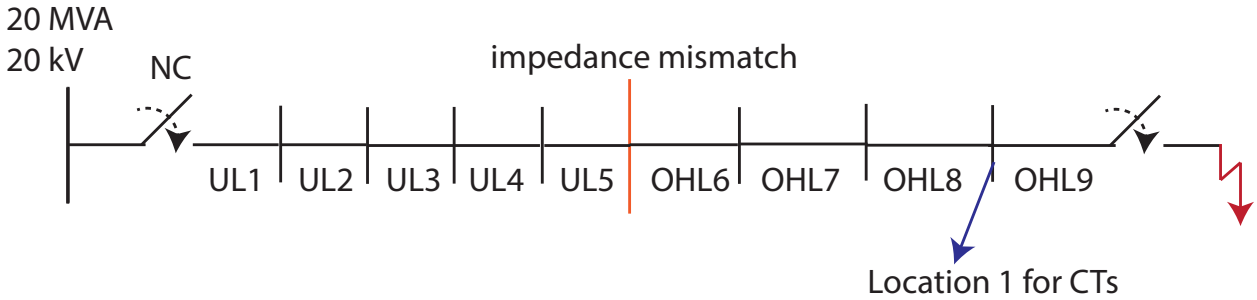

Figure 51. Medium-voltage experimental Setup 1

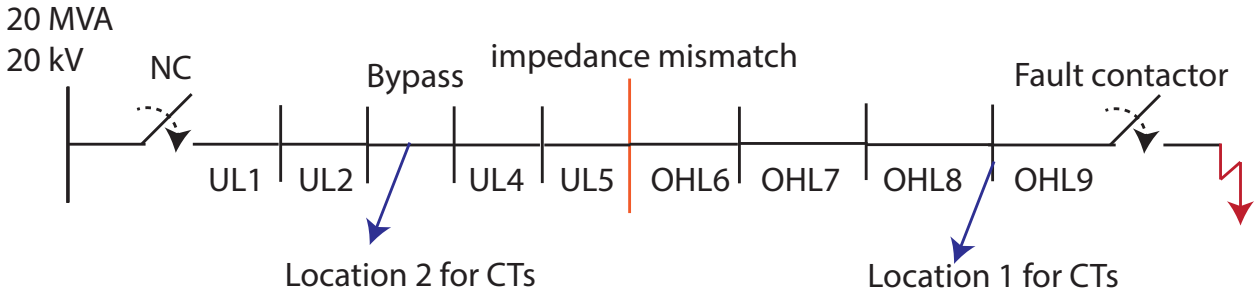

Figure 52. Medium-voltage experimental Setup 2

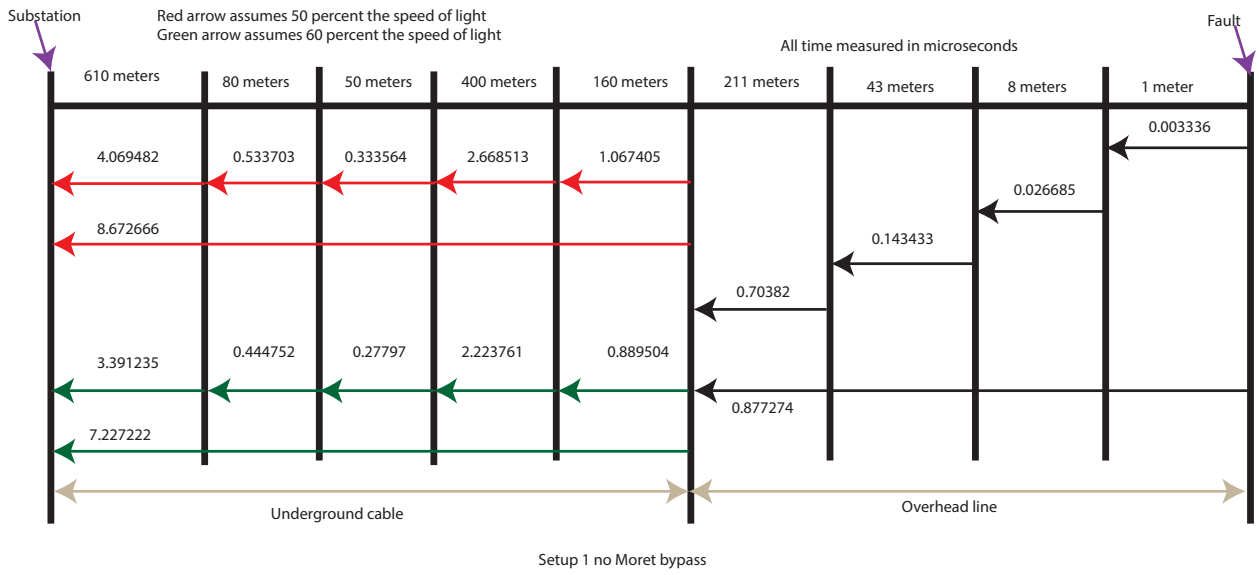

Figure 53. Timing diagram for experimental Setup 1

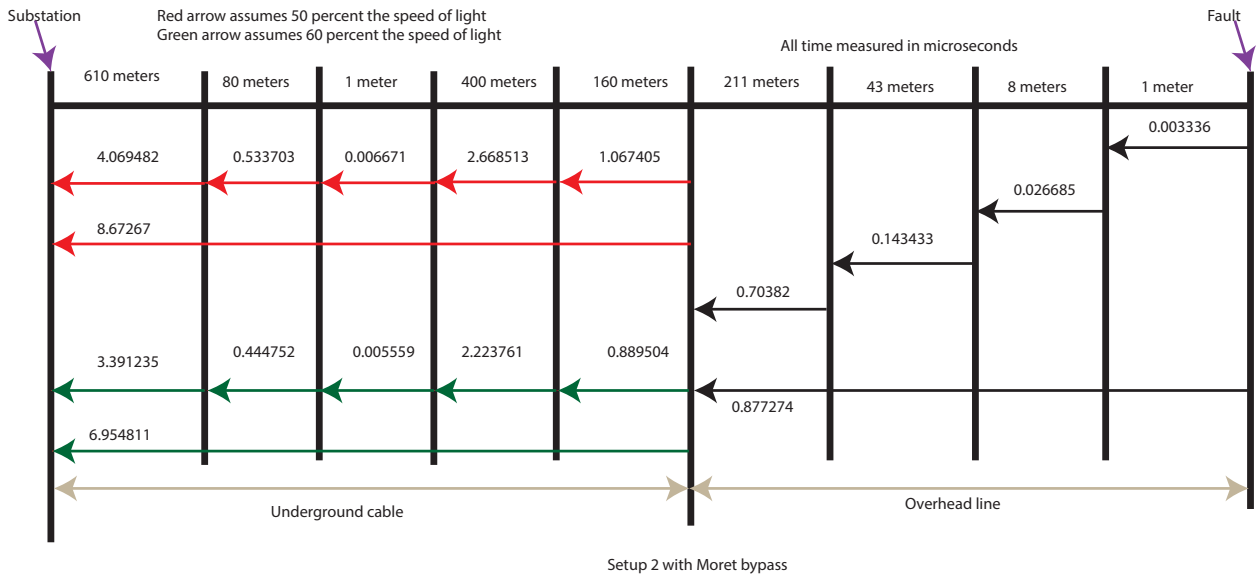

Figure 54. Timing diagram for experimental Setup 2

Figure 55. Test setup used to apply line-to-ground fault.

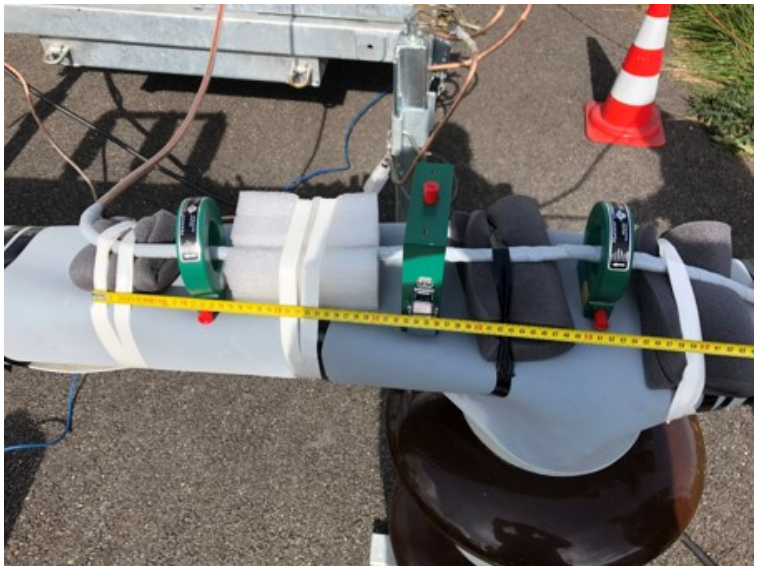

Figure 56. Current transformers used to capture wideband current data during fault experiments

Figure 57. Complete setup with circuit breakers used to apply a fault to the line, current transformers used to measure fault currents, and a wideband oscilloscope used to store data at Location 1

Figure 58. Complete setup with circuit breakers used to apply a fault to the line, current transformers used to measure fault currents, and a wideband oscilloscope used to store data at Location 2 (bypass)

5 Signal-Processing Tools for Traveling Wave Detection

The majority of the electrical power is transmitted and distributed as three-phase alternating systems, and thus they are fundamentally sinusoidal in nature. While measuring voltages and currents of the three phases, these signals were originally modeled as:

$$s(t) = A\sin(\omega t + \phi) + dc + \text{noise},$$

where ω is the fundamental frequency of 60 Hz, A and ϕ are its amplitude and phase angle, and dc is a possible constant DC component. It is well known that other frequencies might be present in the signal—they are referred to as harmonics, subharmonics, and inter-harmonics. Harmonic (or integer harmonics) are frequencies that are an integer factor of the fundamental frequency, subharmonic frequencies are a fraction of the fundamental frequency, and inter-harmonic frequencies are larger than the fundamental frequency and differ from it by a noninteger factor. Considering that the electric grid was originally built assuming a simple directional flow from power generators toward customers, the design of protection systems mostly focused on the amplitude and phase of the fundamental frequency because it is the frequency carrier of the energy, and all other possible frequencies would carry only a tiny fraction of the overall energy. For this reason, legacy and existing protection systems are mostly designed to react only if the current exceeds a (empirically established) threshold value within a short time interval (corresponding to a few cycles of the fundamental frequency). When such a disturbance is detected, these protection systems disconnect the compromised device quickly and safely from the grid and reconnect it—either automatically or with operator intervention—when the system returns to normal operation status.

The introduction of distributed generation—especially in a distribution system—the proliferation of nonlinear power loads, rectifiers, and inverters, which generate a relatively low current, brought significantly more power into the harmonic, subharmonic, and inter-harmonic frequencies. Moreover, these frequencies are modulated in time, reflecting different conditions of the system. Even under normal operation, a variety of significant harmonics are present in distribution system signals and it is well understood that they are a primary cause of power quality problems. For example, the flow of harmonic currents through system impedances creates voltage harmonics, which distort the supply voltage. As a consequence, monitoring and protection systems can no longer ignore nonfundamental frequencies in the network (Langella, Testa, and Alii 2014); however, detecting these frequencies in measured signals presents a mathematical/signal-processing problem. Even if the fundamental frequency and some of its harmonics can be estimated reasonably well, this is definitely not the case for subharmonics and inter-harmonics. In fact, using standard Fourier analysis, these frequencies are represented as a combination of integer harmonics, making their identification difficult, if not impossible. Whereas there have been alternatives to the Fourier analysis for preprocessing signals—e.g., wavelets (Borghetti et al. 2008; Borghetti et al. 2010; Poisson, Rioual, and Meunier 2000)—most representations so obtained either lack fidelity or use a basis that lacks physical interpretabiliy in relation to electrical circuit parameters (see, e.g., (Hu and Gharavi 2018) and references therein).

As described in previous sections a key step in traveling wave-based fault detection is to compactly, efficiently and robustly describe fault signatures. We evaluated several approaches to extract and mathematically describe traveling wave signals using both software and hardware simulations as well as test data. This is a crucial step: if signals are extracted and represented in an appropriate way, pattern (signature) detection in the fault testing data is greatly simplified. We expect that innovations in accurately and robustly representing the often noisy sampled waveforms from electrical circuits will play a fundamental role in future protection algorithms. The standard approach for finding spectral components in a segment of a time series relies on the assumption of stationary frequency components that can then be extracted via Fourier techniques. Since our goal is to identify transient phenomena occurring in a small time interval the stationary persiodicity assumption is invalid and Fourier decomposition would fail to produce accurate features. Linear non-Fourier techniques could potentially be used in some cases, but such approaches (e.g., wavelets) can only approximately identify the dominant frequencies present in a signal.

The signal processing team on this project selected the rational approximations described in Section 2.2.4 for the experiments conducted here. More detailed descriptions of the algorithms developed can be found in (Beylkin and Monzón 2002, 2005, 2009, 2010; Reynolds, Beylkin, and Monzón 2013). The algorithm models signals as polynomial

of exponents in the form:

$$s(t) = \sum_{m=1}^{M} A_m e^{a_m t} \sin(\omega_m t + \phi_m) + dc + \text{noise}, \tag{5.1}$$

and extracts from the measurements a minimal number of real-valued amplitudes, A_m; frequencies, ω_m; phase shifts, ϕ_m; and dc component and additional real-valued parameters, a_m (which determine the local rate of growth or decay on each time interval). This model is similar to that used in conventional decomposition schemes, except that it could have (1) more than one term ($M > 1$) and (2) a nonzero $a_m = 0$. For $M = 1$ and $a_1 = 0$, we recover the familiar representation. The key point is that this information is extracted without using windows, and the frequencies ω_m do not have to be integer or integer factors of the fundamental frequency. In fact, because the fundamental frequency is not exactly 60 Hz because its value drifts slightly around the nominal fundamental frequency—and the same is true for the integer harmonics—our approach also provides better estimates for those frequencies. Importantly, the algorithm requires only a small number of samples, a small multiple of the number of parameters in the representation (5.1); thus, critical differences in our model with respect to the one proposed in (Hu and Gharavi 2018) are the inclusion of the additional exponential factors $e^{a_m t}$ associated with each frequency ω_m as well as minimizing the number of frequencies used in (5.1).

The vector fitting techniques used for the model above relies on accurately and efficiently solving a nonlinear problem, yielding a representation of the data as a short sum of exponential functions. The process extracts precise frequency content without using fixed windows and allows us to separate coherent versus noncoherent components of the signal. These algorithms also yield representations with a near-optimal (smallest) number of terms needed to represent the data within a prescribed accuracy. Besides signal and image processing, these representations enable fast algorithms used to fit low signal amplitude data in the fields of quantum chemistry, geophysics, electron microscopy, among others. Variations of the MIAA approach used for this project have been used for problems in electrical and electronic engineering, telecommunications, computer science, nuclear physics, chemistry, cellular biology, crystallography, finance, and statistics.

Key Properties of our rational function representation

1. The representation can be obtained without using windowing/filtering or denoising. The available samples of the data are used as acquired by an anti-alising analog-to-digital converter.
2. The number of parameters in the representation is minimized for a given target accuracy and time interval. For physical signals, which typically have a sparse representation, these parameters have a clear physical interpretation.
3. The nonlinear algorithm for finding the parameters in a sparse representation is not subject to the standard sampling requirement of at least two samples per period corresponding to the highest frequency present in the signal.
4. The algorithm allows us to control and measure the accuracy of the approximation; in particular, it always recovers the dominant terms representing the signal. It is a powerful denoising mechanism because it clearly distinguishes high-frequency components that may be deemed irrelevant .
5. The algorithms to perform the fit and optimization are fast (of the complexity of the fast Fourier Transform) and robust.
6. Signals can be monitored continuously in overlapping time intervals to track the time evolution of parameters and therefore forecast the expected behavior of the signal. Any departure from the expected behavior can be immediately detected, and their patterns (signatures) can be used to train machine learning algorithms for detection and classification.

Implementation notes

To use these powerful processing tools to build a practical and reliable approach for traveling wave analysis, we performed a series of preliminary experiments to adjust and adapt the general algorithmic approach to suit features in

fault originated traveling waves. Below we list some of the data conditioning and tuning steps we adopted as a guide to potential practitioners:

Checking data reliability and integrity: A manual review of the data was conducted to pre and post fitting to ensure that the features detected by the algorithm were consistent over repeated experiments, consistency improvements sometimes included adjusting the gain of the sensors used and manual removal of artifacts introduced by simulation or emulation tools or while taking data. This step may not be feasible for a field deployment but does highlight the need for careful design and calibration of all components in the data acquistion pipeline to ensure reliable operation.

Time sliding window: Each simulated or measured current and/or voltage signal is processed at a fixed time window. By shifting the window a few samples and extracting the relevant frequency content on each window, we can clearly differentiate the line status before the fault and promptly detect the onset of the fault. One of our goals is to analyze the changes in bandwidth and track the changes in magnitude of the frequency components present before and at the onset of the fault. We plan to experiment with different window lengths and window shifts (amount of samples that are dropped and new ones considered as we slide the processing window) to correctly extract all the relevant information not only at the onset of the fault but also at the arrival of the first reflections. Using the available traveling wave speeds, line configuration, and parameters, we were able to match the measured results with those that can be derived analytically.

Parameterization and interpretation of the processed data: The processing on the sliding window yields a small set of parameters (features) that fit the windowed data. Proper interpretation of the features found requires these features to be consistent across multiple sliding windows. At the time of writing this report, this step was also performed manually by identifying features deemed 'uninformative' or 'redundant' components in the signals. Retaining a small but consistent set of features is necessary for efficient tracking and the inferential determination of an abnormality. In our experience, the feature selection process appears to reflect the operating status of a particular line and so could be proactively configured when the circuit is altered.

6 Development of Visualization Tool

6.1 Background

In our review of prior art, we found very limited work done on methods or tools to visualize traveling wave inference in the context of electrical circuit. The lattice diagram is a popular illustration in the field and was first presented by Bewley in (Bewley 1931) and (Bewley 1933). In (K. P. Wang and Lee 2000), a JAVA-based tool was developed for the analysis of traveling waves. In (Datta and Chatterjee 2013) and (Evrenosoglu, Abur, and Akleman 2007), a MATLAB-based tool was created to analyze traveling waves in 2D and in 3D. These tools were written in an outdated language (JAVA J2SE 1.3). In addition to this, Schweitzer Engineering Laboratories provides a propietary tool to work with their traveling wave-based protection device. Other than these tools, there are no readily available software packages to create Bewley lattice diagrams. To address this, we used the information provided in the literature and created an updated version of an analysis tool in Python. The tool accepts discrete-time event signals consistent with time domain reflections in a line segment and creates a Bewley lattice diagram. An open-source software record was created for the Python-based software module which has been authorized by the U.S. Department of Energy for public dissemination through NREL's GitHub repository. [5]

6.2 Bewley Lattice Analysis Visualization Tool

The Bewley lattice diagram requires the length of the transmission line and the speed of the wave propagation. The main features of the Bewley Python module are to detect the location of the fault, given a set of time-series input data, and to visualize the traveling waves generated.

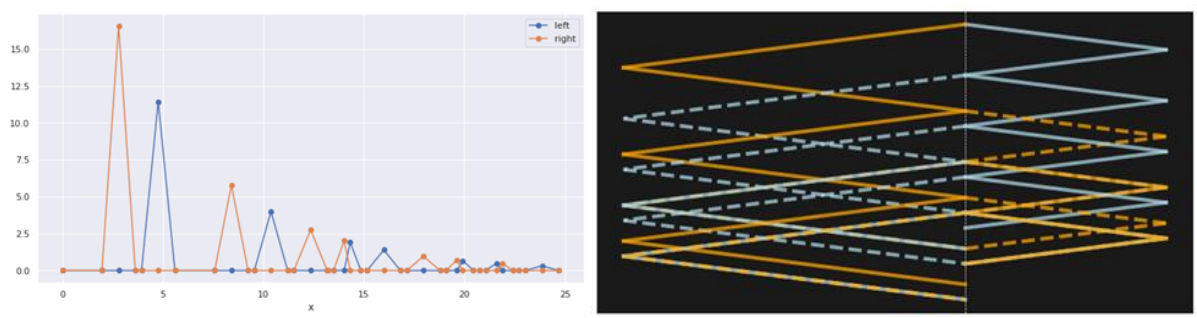

Figure 59. (a) Data used and (b) the corresponding lattice diagram generated by the Bewley module

Given a set of traveling wave time-series data and a line length, the Bewley module can locate the fault and estimate the wave propagation speed. Using this information, users can also visualize the traveling-wave data using a Bewley lattice diagram. The parameters of the visualization can be adjusted to better match the time-series data. This can happen if, for example, a line sag or other environmental variables change the actual wave propagation speed. The Bewley module also facilitates creating example data for testing and experimenting with the module. These synthetic data are provided as a standard pandas data frame object. The data created by this package are shown in Figure 59(a), and the Bewley lattice diagram is shown in Figure 59(b). The Bewley module uses other standard Python modules that are easily installed, such as pandas, NumPy, Matplotlib, and seaborn. This ensures that the code will easily run on Linux, Mac OSX, or Windows.

The first iteration of the Bewley Python package relied on Matplotlib as the base for its plotting. We quickly realized that this is less desirable because most the value of this plot is being able to interact and extract information from the graph. In an effort to make this package more useful, we moved to a fully interactive plot based on Plotly, a visualization package built on web standards and made accessible for scientific visualizations through Python. We also improved the algorithm used to transform the Bewley inputs into the data structure used to make the lattice

[5] https://github.com/nrel/bewley

diagram in Plotly. We compute only the levels needed to visualize the lattice, which makes the code more efficient and more informative for the visualization.

6.3 Working with Electromagnetic Transient Data

The initial set of single-pulse EMT data generated did not contain enough information to determine the fault location. Having an estimate of the wave propagation speed helps narrow the uncertainty around our estimate, but ultimately we will need more information. The next set of EMT data has more information, but our focus was on understanding how these data line up with the Bewley lattice and if there is any error in this alignment. Figure 60 shows the new Bewley lattice diagram with the corresponding time-series diagrams on each side of the lattice.

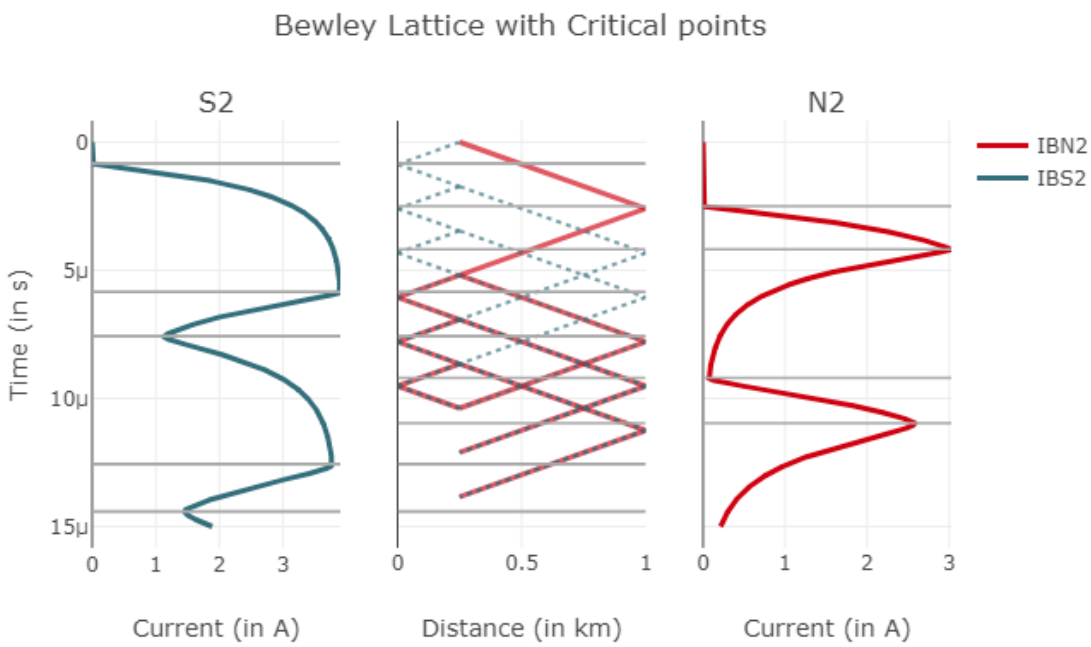

Figure 60. Bewley lattice diagram created from EMT simulations results using updated Python code

The leftmost graph is the southern bus (blue), and the rightmost graph is the northern bus (red). The lattice is in the middle, and the colors correspond to the bus locations. The critical points from each time series are also plotted. It is important to note how these horizontal lines line up well with the lattice inflection points. Figure 61 shows a zoomed-in version of the previous figure and gives a better indication of the error. This also shows the power of interactive visualization—we can zoom and hover on the graph to gain more insight than is available in statically produced graphics.

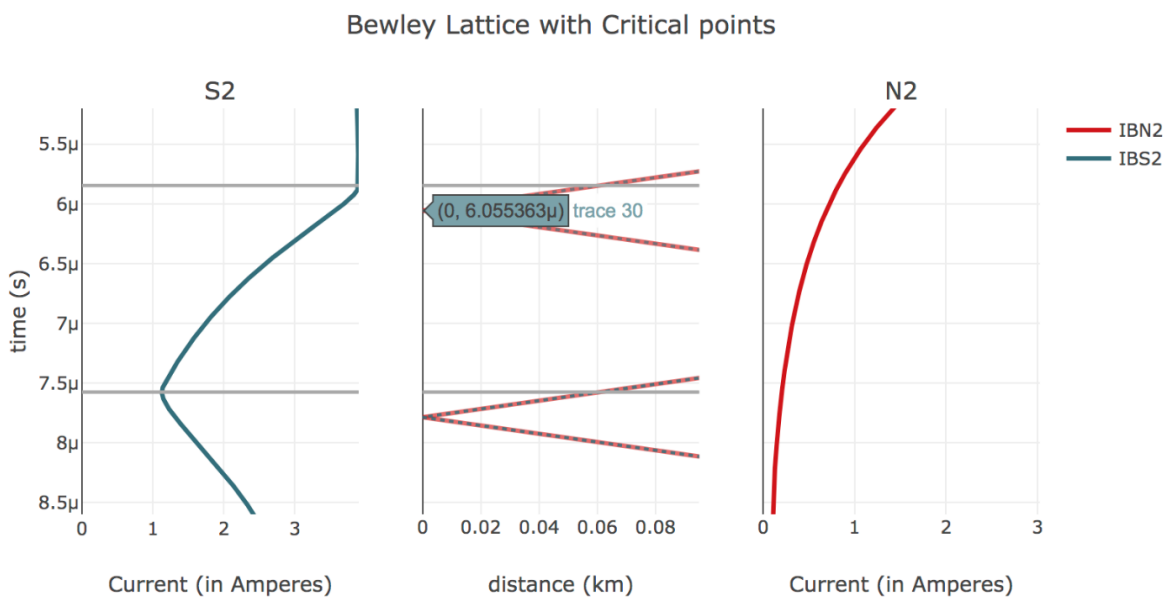

Figure 61. Updated zoom-in feature made available through the use of Plotly

7 Case study: Advanced Processing of Field Data

A variety of tests were performed on the data collected in a controlled experiment to decide the best way to the extract useful traveling wave information from the raw measurements. The experimental setup to collect the data is described in Section 4.3.

To illustrate the extraction of traveling wave information, we consider the result of a line-to-ground fault test. Figure 62 displays the whole range of measurements, and Figure 63 shows the relevant portion of the signal that clearly shows the abrupt change in the signal caused by the fault.

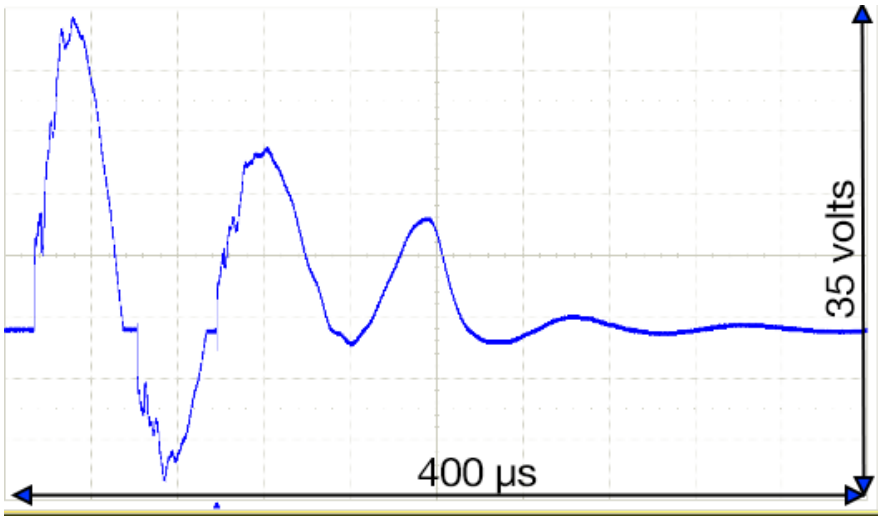

Figure 62. Full time interval of the measured field data

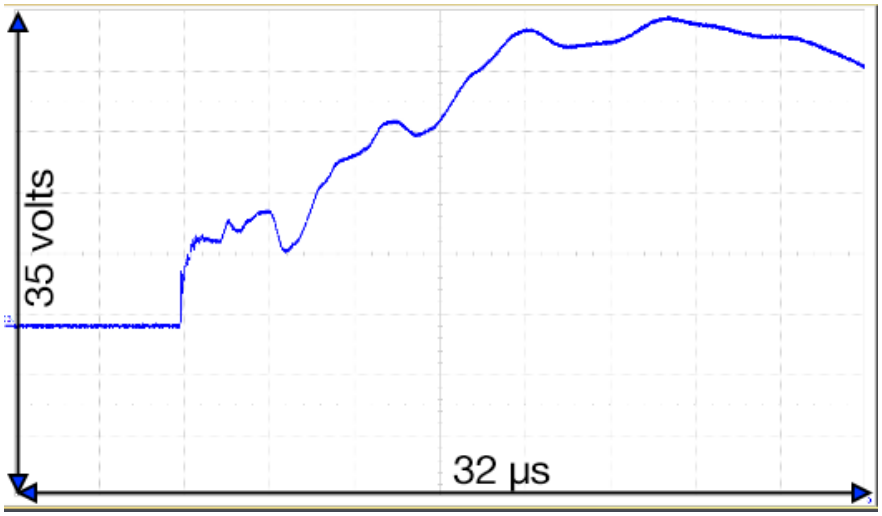

Figure 63. Measured field data (zoomed in)

An acquistion interval was selected that captures the fault onset and a sufficient pre and post fault duration. In order to reduce spurious detections the acquisition window was curtailed to recording evolution of the sampled signal unrelated to the fault. Then the selected raw data are approximated within a target accuracy by the techniques in Chapter 5. The processing time interval and the resulting fit are superimposed in Figure 64. The technique would produce a more accurate fit with more terms; however, there is diminishing value in succesive functions but high computational

costs. In some cases the addtion of terms results in overfitting components of the signal that can be safely ignored or considered noise. Finding the optimal number of functions requires some manual tuning of the system based on the density of reflection points and the resolution of the data being collected.

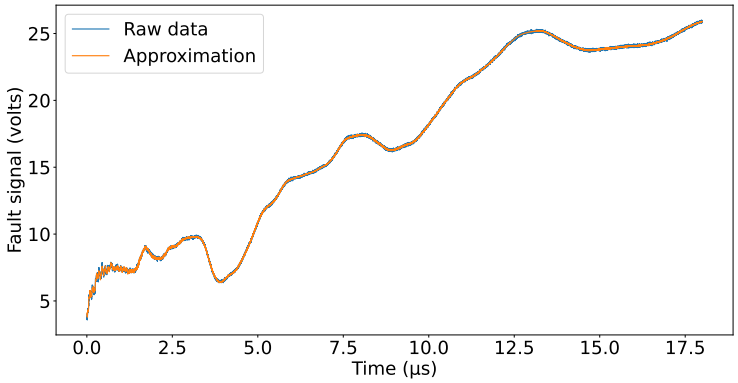

Figure 64. Data and their approximation on the processing time interval, which includes the fault onset

Figure 65 displays the resulting approximation error together with the accuracy requested (horizontal red line). As expected, the onset of the fault is very hard to reproduce unless a very high-frequency range is included in the approximation. As shown in Figure 66, however, the distribution of the errors is close to Gaussian in nature, which is a verification of the succesful recovery of the structures in the signal using our approximation algorithm. This fit was achieved using 20 terms in the approximation model of the form described in (5.1). Figure 67 shows each component, labeled and organized in increasing frequency from top to bottom and left to right. Of these 20 components, only 6 (terms 3 through 8) belong to the frequency range (115 kHz to 758 kHz) that we expect to be accurately captured by the current transformers and to be of practical use. For this reason, Figure 68 shows the approximation (denoised) signal, the sum of these 6 kept components, and the discarded portion so that the kept portion plus the discarded adds up to the denoised signal. For later reference, we also indicate the locations of signal extrema for the retained portion—that is, the locations where the signal reaches its local maximum and minimum values. The location of these extrema can now be associated with different properties of the signal and the reflections expected to be generated from the test setup.

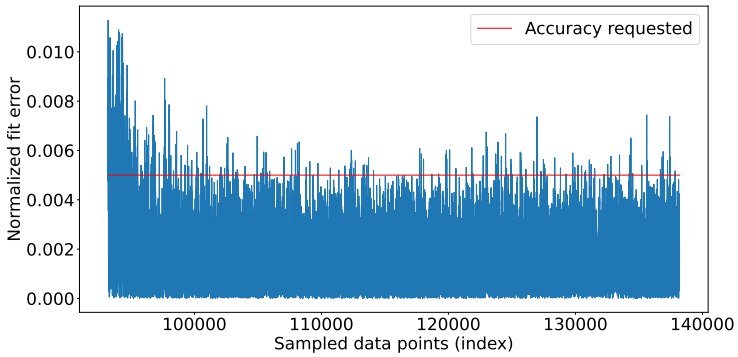

Figure 65. Approximation error and target accuracy

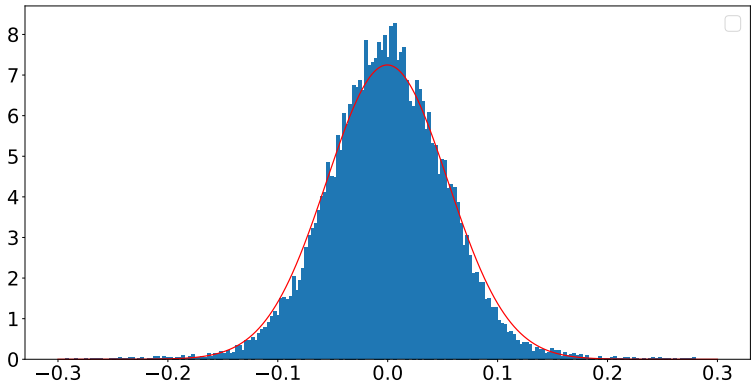

Figure 66. Distribution of approximation error values (blue) show good correspondence with a model Gaussian distribution (red).

Summary

- Our signal processing technique accurately fits the raw data while adequately reducing noise and ignoring extraneous high-frequency components. Traveling wave signatures can so be determined with high fidelity with good discrimination between different fault types.
- Because individual rational components are have frequency domain interpretation, those outside the current transformer calibration range can be safely removed without distorting the components corresponding to the frequencies of interest.
- Even when test data from a real fault was fit using the MIAA scheme only a few rational components were requred to capture the fundamental properties of a real line fault. This bodes well for the practical feasibility when scaling this solution up to larger circuits with more junctions and sensor sites.

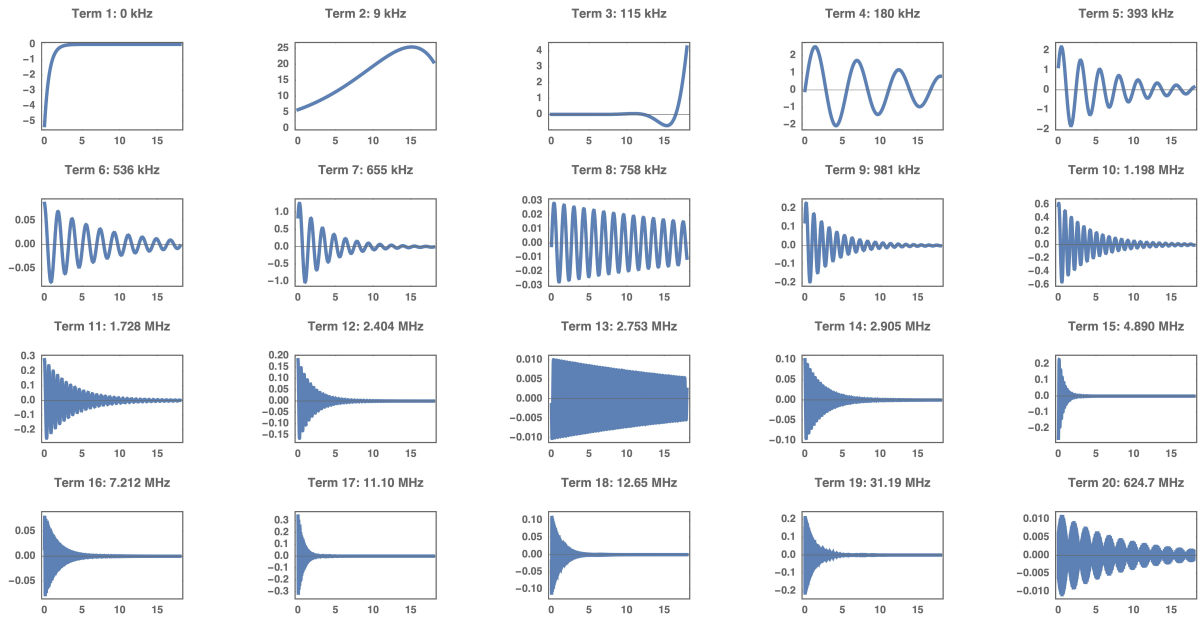

Figure 67. The set of 20 individual rational components used for the signal approximation

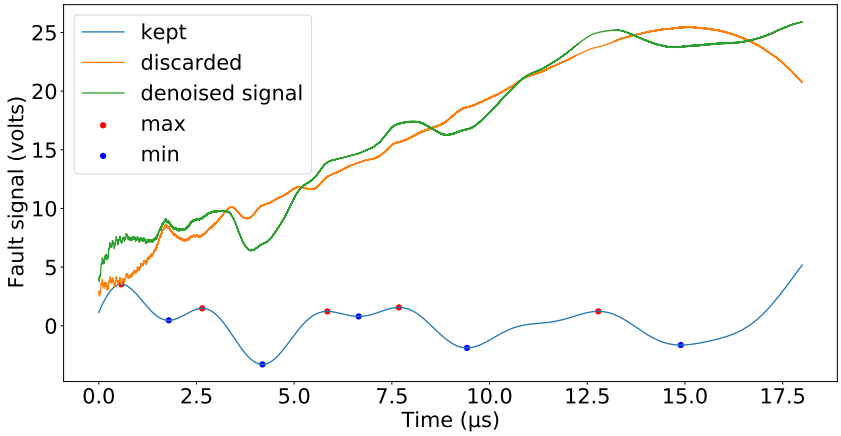

Figure 68. Denoised, discarded, and kept signal portions

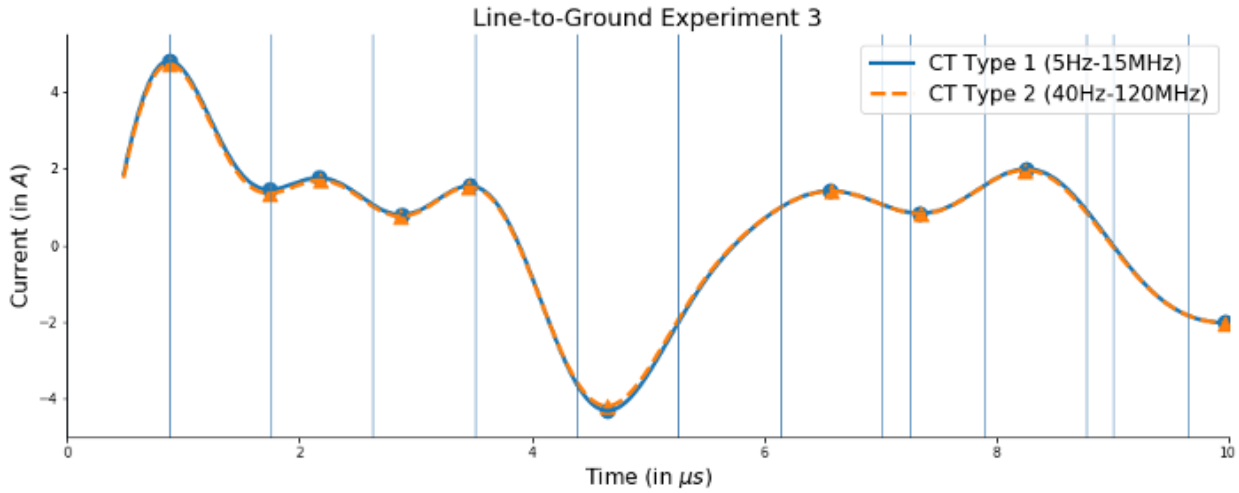

Figure 69. Traveling Wave observed in filtered current measurements in a line-to-ground fault experiment

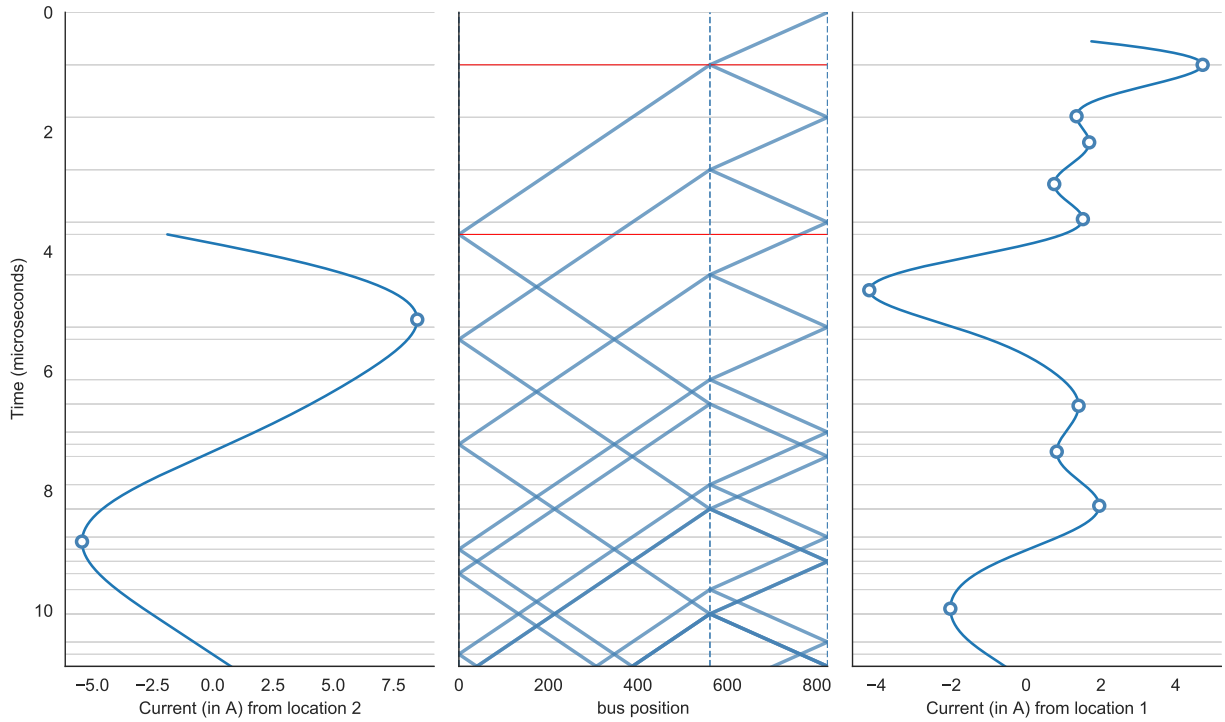

Figure 70. Traveling wave visualized using the developed Bewley lattice diagram in filtered current measurements in a line-to-ground fault experiment

8 Conclusions and Future Work

The protection of distribution systems with high penetrations of inverter-based distributed energy resources is a major challenge for utilities. Traveling wave-based fault location has been proposed in the literature, and the project team performed a detailed literature survey on this. This report discussed the feasibility of using traveling waves to detect and locate faults. The report addressed the main gaps identified in the literature survey.

This report presented the appropriate modeling requirements to model the power system components in the EMT domain to recreate and study traveling waves in distribution systems. The modified IEEE test system presented in this report considers frequency dependent line models. Frequency-dependent line modeling is mature, and the literature has covered this in detail. But frequency-dependent modeling of other power system components—such as transformers and inverter-based distributed energy resources—needs to be revisited and improved to accurately model traveling waves in the EMT domain.

Advanced signal-processing tools and visualization tools were developed in this project, and brief introductions to the developed tools were presented. The developed visualization tools are available in open source through NREL's GitHub repository.

Finally, medium-voltage experiments were performed at an outdoor experimental facility. Multiple fault scenarios were run, and high-frequency current information was captured using wideband current transformers. The captured current information was filtered and visualized using the tools developed in this project. The results indicate that high-frequency current signatures generated as a result of fault events and traveling wave information can be successfully extracted from sampled measurements. One experimental data collection campaign was digitized, filtered, processed, analyzed and visualized using the full suite of tools developed by the team to show a prototype of an end to end traveling wave based localization workflow.

Additional modeling, simulation, and experiments need to be performed to fully understand traveling wave phenomena in distribution systems and to use it for distribution system fault detection and identification. The modeling approach and the experimental results presented in this report were primarily intended to fill some gaps in the literature and to validate some theoretical results in signal processing.

A significant part of our contribution is in the engineering and design of test hardware, data acquistion systems and signal processing software. We are optimistic that the tools we have developed here will help other researchers developing algorithms for fault localization, identification and service restoration and significantly accelerate testing and validation of the still nascent but exciting field.

Bibliography

Abhyankar, S., J. Brown, E. M. Constantinescu, D. Ghosh, B. F. Smith, and H. Zhang. 2018. "PETSc/TS: A Modern Scalable ODE/DAE Solver Library". *preprint arXiv:1806.01437*.

Antonini, G., A. Orlandi, and S. A. Pignari. 2013. "Review of Clayton R. Paul Studies on Multiconductor Transmission Lines". *IEEE Transactions on Electromagnetic Compatibility* 55 (4): 639–647. doi:10.1109/TEMC.2013.2265038.

"Application of Capacitors on Rural ELectric Systems". 2018. *RUS 1724D-112* ().

Berljafa, M., and S. Güttel. 2017. "The RKFIT algorithm for nonlinear rational approximation". *SIAM Journal on Scientific Computing* 39 (5): A2049–A2071.

Bewley, L. V. 1931. "Traveling Waves on Transmission Systems". *Transactions of the American Institute of Electrical Engineers* 50, no. 2 (): 532–550. doi:10.1109/T-AIEE.1931.5055827.

Bewley, L. 1933. *Traveling waves on transmission systems*. J. Wiley & sons. https://books.google.com/books?id=MRQhAAAAMAAJ.

Beylkin, G., G. Fann, R. J. Harrison, C. Kurcz, and L. Monzón. 2012. "Multiresolution representation of operators with boundary conditions on simple domains". *Applied and Computational Harmonic Analysis* 33 (1): 109–139.

Beylkin, G., C. Kurcz, and L. Monzón. 2007. "Grids and transforms for band-limited functions in a disk". *Inverse Problems* 23 (5): 2059.

– . 2008. "Fast algorithms for Helmholtz Green's functions". *Proceedings of the Royal Society A: Mathematical, Physical and Engineering Sciences* 464 (2100): 3301–3326.

– . 2009. "Fast convolution with the free space Helmholtz Green's function". *Journal of Computational Physics* 228 (8): 2770–2791.

Beylkin, G., R. D. Lewis, and L. Monzón. 2012. "On the design of highly accurate and efficient IIR and FIR filters". *IEEE Transactions on Signal Processing* 60 (8): 4045–4054.

Beylkin, G., and L. Monzón. 2002. "On generalized Gaussian quadratures for exponentials and their applications". *Applied and Computational Harmonic Analysis* 12 (3): 332–373.

– . 2005. "On approximation of functions by exponential sums". *Applied and Computational Harmonic Analysis* 19 (1): 17–48.

– . 2009. "Nonlinear inversion of a band-limited Fourier transform". *Applied and Computational Harmonic Analysis* 27 (3): 351–366.

– . 2010. "Approximation by exponential sums revisited". *Applied and Computational Harmonic Analysis* 28 (2): 131–149.

– . 2016. "Efficient representation and accurate evaluation of oscillatory integrals and functions". *Discrete & Continuous Dynamical Systems-A* 36 (8): 4077–4100.

Beylkin, G., L. Monzón, and I. Satkauskas. 2018. "On computing distributions of products of non-negative independent random variables". See also arXiv:1707.07762, *Appl. Comput. Harmon. Anal.* 46 (2): 400–416. doi:https://doi.org/10.1016/j.acha.2018.01.002. https://www.sciencedirect.com/science/article/pii/S1063520318300228.

– . 2019. "On computing distributions of products of random variables via Gaussian multiresolution analysis". See also arXiv:1611.08580, *Appl. Comput. Harmon. Anal.* 47 (2): 306–337. doi:https://doi.org/10.1016/j.acha.2017.08.008. http://www.sciencedirect.com/science/article/pii/S1063520317300969.

Beylkin, G., and K. Sandberg. 2014. "ODE solvers using band-limited approximations". *Journal of Computational Physics* 265:156–171.

Bo, Z. Q., M. A. Redfern, and G. C. Weller. 2000. "Positional protection of transmission line using fault generated high frequency transient signals". *IEEE Transactions on Power Delivery* 15, no. 3 (): 888–894. doi:10.1109/61.871348.

Bo, Z., G. Weller, and M. Redfern. 1999. "Accurate Fault Location Technique for Distribution System Using Fault-Generated High-Frequency Transient Voltage Signals". *IEE Proceedings - Generation, Transmission and Distribution* 146 (1): 73. ISSN: 13502360.

Borghetti, A., M. Bosetti, M. Di Silvestro, C. Nucci, and M. Paolone. 2008. "Continuous-wavelet transform for fault location in distribution power networks: Definition of mother wavelets inferred from fault originated transients". *IEEE Transactions on Power Systems* 23 (2): 380–388.

Borghetti, A., M. Bosetti, C. A. Nucci, M. Paolone, and A. Abur. 2010. "Integrated use of time-frequency wavelet decompositions for fault location in distribution networks: Theory and experimental validation". *IEEE Transactions on Power Delivery* 25 (4): 3139–3146.

Borghetti, A., S. Corsi, C. A. Nucci, M. Paolone, L. Peretto, and R. Tinarelli. 2006. "On the use of continuous-wavelet transform for fault location in distribution power systems". *International Journal of Electrical Power & Energy Systems* 28 (9): 608–617.

Bradley, B. K., B. A. Jones, G. Beylkin, K. Sandberg, and P. Axelrad. 2014. "Bandlimited implicit Runge-Kutta integration for Astrodynamics". *Celestial Mechanics and Dynamical Astronomy* 119, no. 2 (): 143–168. ISSN: 1572-9478, visited on 04/10/2019. doi:10.1007/s10569-014-9551-x. https://doi.org/10.1007/s10569-014-9551-x.

Brandao Faria, J. A., and J. F. Borges da Silva. 1990. "The effect of randomly earthed ground wires on PLC transmission-a simulation experiment". *IEEE Transactions on Power Delivery* 5, no. 4 (): 1669–1677. doi:10.1109/61.103661.

Budner, A. 1970. "Introduction of Frequency-Dependent Line Parameters into an Electromagnetic Transients Program". *IEEE Transactions on Power Apparatus and Systems* PAS-89, no. 1 (): 88–97. doi:10.1109/TPAS.1970.292674.

Cabral, E. S. Bañuelos, B. Gustavsen, J. A. Gutiérrez Robles, H. K. Hoidalen, and J. L. Naredo. 2016. "Computational efficiency improvement of the universal line model by use of rational approximations with real poles". *Electric Power Systems Research* 140:424–434.

Carson, J. R. 1926. "Wave propagation in overhead wires with ground return". *The Bell System Technical Journal* 5, no. 4 (): 539–554. doi:10.1002/j.1538-7305.1926.tb00122.x.

Castellanos, F., J. R. Martí, and F. Marcano. 1997. "Phase-domain multiphase transmission line models". *International Journal of Electrical Power & Energy Systems* 19 (4): 241–248.

Castro, S. L., L. A. Monzón, G. A. Wick, R. D. Lewis, and G. Beylkin. 2018. "Subpixel variability and quality assessment of satellite sea surface temperature data using a novel High Resolution Multistage Spectral Interpolation (HRMSI) technique". *Remote sensing of environment* 217:292–308.

Che, L., M. E. Khodayar, and M. Shahidehpour. 2014. "Adaptive Protection System for Microgrids: Protection practices of a functional microgrid system." *IEEE Electrification Magazine* 2, no. 1 (): 66–80. doi:10.1109/MELE.2013.2297031.

Cullen, C. G. 2012. *Matrices and linear transformations*. Courier Corporation.

Damle, A., G. Beylkin, T. Haut, and L. Monzón. 2013. "Near optimal rational approximations of large data sets". *Applied and Computational Harmonic Analysis* 35 (2): 251–263.

Datta, B., and S. Chatterjee. 2013. "Simulation of Bewley's lattice diagram using MATLAB". In *2013 IEEE 1st International Conference on Condition Assessment Techniques in Electrical Systems (CATCON)*, 11–16. doi:10.1109/CATCON.2013.6737466.

Davis, T. A., and E. Palamadai Natarajan. 2010. "Algorithm 907: KLU, a direct sparse solver for circuit simulation problems". *ACM Transactions on Mathematical Software* 37 (3): 36.

Deschrijver, D., B. Gustavsen, and T. Dhaene. 2007. "Advancements in iterative methods for rational approximation in the frequency domain". *IEEE Transactions on Power Delivery* 22 (3): 1633–1642.

DeTroye, D. J., and R. J. Chase. 1994. *The calculation and measurement of Helmholtz coil fields*. Tech. rep. Army Research Lab Adelphi MD.

"Distribution Conductor Clearances and Span Limitations". 2003. *RUS 1724E-154* ().

Dommel, H. W. 1996. *EMTP Theory Book*. 2nd ed. Microtran Power System Analysis Corporation.

Dwivedi, A., and X. Yu. 2011. "Fault location in radial distribution lines using travelling waves and network theory". In *2011 IEEE International Symposium on Industrial Electronics*, 1051–1056.

El-Hami, M., L. L. Lai, D. J. Daruvala, and A. T. Johns. 1992. "A new travelling-wave based scheme for fault detection on overhead power distribution feeders". *IEEE Transactions on Power Delivery* 7, no. 4 (): 1825–1833. doi:10.1109/61.156985.

Evrenosoglu, C., A. Abur, and E. Akleman. 2007. "Three dimensional visualization and animation of travelling waves in power systems". *Electric power systems research* 77 (7): 876–883. doi:https://doi.org/10.1016/j.epsr.2006.08.002. http://www.sciencedirect.com/science/article/pii/S0378779606001787.

F. Yan, Z. Chen, Z. Liang, Y. Kong, and P. Li. 2002. "Fault location using wavelet packets". In *Proceedings. International Conference on Power System Technology*, vol. 4, 2575–2579 vol.4. doi:10.1109/ICPST.2002.1047251.

Golub, G., and C. V. Loan. 1996. *Matrix Computations*. 3rd. Johns Hopkins University Press.

Grasselli, U., and A. Prudenzi. 2010. “Voltage transient origin localization tests: Short low voltage cable case study”. In *SPEEDAM 2010*, 74–79. doi:10.1109/SPEEDAM.2010.5545045.

Guidelines for Representation of Network Elements When Calculating Transients. 1990.

Gustavsen, B. 2005. “Validation of frequency-dependent transmission line models”. *IEEE Transactions on Power Delivery* 20 (2): 925–933.

Gustavsen, B. 2006. “Improving the pole relocating properties of vector fitting”. *IEEE Transactions on Power Delivery* 21, no. 3 (): 1587–1592. doi:10.1109/TPWRD.2005.860281.

Gustavsen, B. 2008. “User’s Guide for vectfit3.m”. *SINTEF Energy Research, Trondheim, Norway*.

Gustavsen, B. 2012. “Modal Domain-Based Modeling of Parallel Transmission Lines With Emphasis on Accurate Representation of Mutual Coupling Effects”. *IEEE Transactions on Power Delivery* 27, no. 4 (): 2159–2167. doi:10.1109/TPWRD.2012.2202923.

Gustavsen, B., and J. Nordstrom. 2008. “Pole Identification for The Universal Line Model Based on Trace Fitting”. *IEEE Transactions on Power Delivery* 23, no. 1 (): 472–479. doi:10.1109/TPWRD.2007.911186.

Gustavsen, B., and A. Semlyen. 1998a. “Calculation of transmission line transients using polar decomposition”. *IEEE Transactions on Power Delivery* 13, no. 3 (): 855–862. doi:10.1109/61.686984.

– . 1998b. “Combined phase and modal domain calculation of transmission line transients based on vector fitting”. *IEEE Transactions on Power Delivery* 13, no. 2 (): 596–604. doi:10.1109/61.660936.

– . 1998c. “Simulation of transmission line transients using vector fitting and modal decomposition”. *IEEE Transactions on Power Delivery* 13, no. 2 (): 605–614. doi:10.1109/61.660941.

– . 1999. “Rational approximation of frequency domain responses by vector fitting”. *IEEE Transactions on Power Delivery* 14, no. 3 (): 1052–1061. doi:10.1109/61.772353.

Gustavsen, B. 2013. “Avoiding numerical instabilities in the universal line model by a two-segment interpolation scheme”. *IEEE transactions on power delivery* 28 (3): 1643–1651.

Gutt, G., D. Lawrence, S. Cobb, and M. O’Connor. 2018. “Recent PNT improvements and test results based on low earth orbit satellites”. In *Proceedings of the 2018 International Technical Meeting of The Institute of Navigation*, 570–577.

Haut, T., G. Beylkin, and L. Monzón. 2013. “Solving Burgers’ equation using optimal rational approximations”. *Applied and Computational Harmonic Analysis* 34 (1): 83–95.

Hendrickx, W., and T. Dhaene. 2006. “A discussion of "Rational approximation of frequency domain responses by vector fitting"”. *IEEE Transactions on Power Systems* 21, no. 1 (): 441–443. doi:10.1109/TPWRS.2005.860905.

Hewlett-Packard, H. 1991. “Model 4284A Precision LCR Meter”. *Operation Manual (Dec. 1991) pp*: 2–1.

Hu, B., and H. Gharavi. 2018. “A Fast Recursive Algorithm For Spectrum Tracking in Power Grid Systems”. *IEEE Transactions on Smart Grid* 10 (3): 2882–2891.

IEEE. 2018. “IEEE Standard for Interconnection and Interoperability of Distributed Energy Resources with Associated Electric Power Systems Interfaces”. *Std 1547-2018 (Revision of IEEE Std 1547-2003)*: 1–138. doi:10.1109/IEEESTD.2018.8332112.

“IEEE Guide for Determining Fault Location on AC Transmission and Distribution Lines”. 2015. *IEEE Std C37.114-2014 (Revision of IEEE Std C37.114-2004)* (): 1–76. doi:10.1109/IEEESTD.2015.7024095.

Iserles, A. 2009. *A First Course in the Numerical Analysis of Differential Equations*. Google-Books-ID: M0tkw4oUucoC. Cambridge University Press. ISBN: 978-0-521-73490-5.

K. P. Wang and K. Lee. 2000. “Visualizing wavelet transformed travelling waves on power transmission line using JAVA”. In *2000 International Conference on Advances in Power System Control, Operation and Management, APSCOM-00*, vol. 2, 349–353 vol.2. doi:10.1049/cp:20000421.

Kavousi-Fard, A., and T. Niknam. 2014. “Optimal Distribution Feeder Reconfiguration for Reliability Improvement Considering Uncertainty”. *IEEE Transactions on Power Delivery* 29, no. 3 (): 1344–1353. doi:10.1109/TPWRD.2013.2292951.

Kersting, W. H. 2001. “Radial Distribution Test Feeders”. In *2001 IEEE Power Engineering Society Winter Meeting. Conference Proceedings (Cat. No.01CH37194)*, 2:908–912. Columbus, OH, USA: IEEE.

Kocar, I., and J. Mahseredjian. 2015. “Accurate frequency dependent cable model for electromagnetic transients”. *IEEE Transactions on Power Delivery* 31 (3): 1281–1288.

Kocar, I., J. Mahseredjian, and G. Olivier. 2010. “Improvement of numerical stability for the computation of transients in lines and cables”. *IEEE transactions on power delivery* 25 (2): 1104–1111.

Kroposki, B., B. Johnson, Y. Zhang, V. Gevorgian, P. Denholm, B. Hodge, and B. Hannegan. 2017. "Achieving a 100% Renewable Grid: Operating Electric Power Systems with Extremely High Levels of Variable Renewable Energy". *IEEE Power and Energy Magazine* 15, no. 2 (): 61–73. doi:10.1109/MPE.2016.2637122.

Langella, R., A. Testa, and E. Alii. 2014. *IEEE recommended practice and requirements for harmonic control in electric power systems*. IEEE.

Lewis, R. D., G. Beylkin, and L. Monzón. 2013. "Fast and accurate propagation of coherent light". *Proceedings of the Royal Society A: Mathematical, Physical and Engineering Sciences* 469 (2159): 20130323.

Lipiński, M, E Van Der Bij, J Serrano, T Włostowski, G Daniluk, A Wujek, M Rizzi, and D Lampridis. 2018. "White rabbit applications and enhancements". In *2018 IEEE International Symposium on Precision Clock Synchronization for Measurement, Control, and Communication (ISPCS)*, 1–7. IEEE.

Marcano, F. J. 1996. "Modelling of transmission lines using idempotent decomposition". PHD Thesis, University of British Columbia.

Marcano, F. J., and J. R. Martí. 1997. "Idempotent line model: Case studies". In *Int. Conf. Power Syst. Transients, Seattle, WA*.

Martí, J. R. 1981. "The Problem of Frequency Dependence in Transmission Line Modelling". Thesis, University of British Columbia.

Martí, J. R. 1982. "Accurate Modelling of Frequency-Dependent Transmission Lines in Electromagnetic Transient Simulations". *IEEE Transactions on Power Apparatus and Systems* PAS-101, no. 1 (): 147–157. doi:10.1109/TPAS.1982.317332.

Martí, J. R. 1982. "Accurate Modelling of Frequency-Dependent Transmission Lines in Electromagnetic Transient Simulations". *IEEE Transactions on Power Apparatus and Systems* PAS-101, no. 1 (): 147–157. doi:10.1109/TPAS.1982.317332.

Marti, J. R. 1982. "Accurate Modelling of Frequency-Dependent Transmission Lines in Electromagnetic Transient Simulations". *IEEE Transactions on Power Apparatus and Systems* PAS-101, no. 1 (): 147–157.

Martí, J. R., and J. Lin. 1989. "Suppression of numerical oscillations in the EMTP power systems". *IEEE Transactions on Power Systems* 4, no. 2 (): 739–747. doi:10.1109/59.193849.

Martí, L. 1988. "Simulation of transients in underground cables with frequency-dependent modal transformation matrices". *IEEE Transactions on Power Delivery* 3, no. 3 (): 1099–1110. doi:10.1109/61.193892.

Martí, L., R. H. Brierley, and T. E. Grainger. 1995. "Analysis of electromagnetic transients in cross-bounded cable systems using frequency depedent cable models". In *IPST*, 95:5–10.

Meliopoulos, A. P. S., G. J. Cokkinides, Z. Tan, S. Choi, Y. Lee, and P. Myrda. 2013. "Setting-Less Protection: Feasibility Study". In *2013 46th Hawaii International Conference on System Sciences*, 2345–2353. doi:10.1109/HICSS.2013.628.

Meyer, W. S., and H. W. Dommel. 1974. "Numerical Modelling of Frequency-Dependent Transmission-Line Parameters in an Electromagnetic Transients Program". *IEEE Transactions on Power Apparatus and Systems* PAS-93, no. 5 (): 1401–1409. doi:10.1109/TPAS.1974.293870.

Monzón, L., W. Johns, S. Iyengar, M. Reynolds, J. Maack, and K. Prabakar. 2020. "A Multi-Function AAA Algorithm Applied to Frequency-Dependent Line Modeling". *Conference: 2020 IEEE PES General Meeting, Montreal, Canada*.

Morales-Rodriguez, J., E. Medina, J. Mahseredjian, A. Ramirez, K. Sheshyekani, and I. Kocar. 2019. "Frequency-Domain Fitting Techniques: A Review". *IEEE Transactions on Power Delivery*: 1–1. doi:10.1109/TPWRD.2019.2932395.

Morales Rodriguez, J. 2019. "Computation of Frequency Dependent Network Equivalents Using Vector Fitting, Matrix Pencil Method and Loewner Matrix". PhD thesis, Polytechnique Montréal.

Morched, A., B. Gustavsen, and M. Tartibi. 1999. "A universal model for accurate calculation of electromagnetic transients on overhead lines and underground cables". *IEEE Transactions on Power Delivery* 14, no. 3 (): 1032–1038. doi:10.1109/61.772350.

Morched, A, B Gustavsen, and M Tartibi. 1999. "A Universal Model for Accurate Calculation of Electromagnetic Transients on Overhead Lines and Underground Cables". *IEEE Transactions on Power Delivery* 14, no. 3 (): 1032–1038. doi:10.1109/61.772350.

Morton, Y. J., F. van Diggelen, J. J. Spilker Jr, B. W. Parkinson, S. Lo, and G. Gao. 2021. *Position, Navigation, and Timing Technologies in the 21st Century: Integrated Satellite Navigation, Sensor Systems, and Civil Applications*. John Wiley & Sons.

Nagaoka, N., and A. Ametani. 1988. "A development of a generalized frequency-domain transient program-FTP". *IEEE Transactions on Power Delivery* 3 (4): 1996–2004.

Nakatsukasa, Y., O. Sète, and L. N. Trefethen. 2018. "The AAA Algorithm for Rational Approximation". *SIAM Journal on Scientific Computing* 40 (3): A1494–A1522. ISSN: 1095-7197. doi:10.1137/16m1106122. http://dx.doi.org/10.1137/16M1106122.

NERC. 2017. *1,200 MW Fault Induced Solar Photovoltaic Resource Interruption Disturbance Report*.

Neville Watson and Jos Arrillaga. 2003. *Power Systems Electromagnetic Transients Simulation*. First. UK: IET. ISBN: 978-0-85296-106-3.

Noda, T., K. Takenaka, and T. Inoue. 2009. "Numerical Integration by the 2-Stage Diagonally Implicit Runge-Kutta Method for Electromagnetic Transient Simulations". *IEEE Transactions on Power Delivery* 24, no. 1 (): 390–399. doi:10.1109/TPWRD.2008.923397.

Paul, C. R. 1994. *Analysis of Multiconductor Transmission Lines*. 1st. New York, NY, USA: John Wiley & Sons. ISBN: 047102080X.

Paul, C. R. 1996. "Decoupling the multiconductor transmission line equations". *IEEE Transactions on Microwave Theory and Techniques* 44, no. 8 (): 1429–1440. doi:10.1109/22.536026.

– . 2007. "A Brief History of Work in Transmission Lines for EMC Applications". *IEEE Transactions on Electromagnetic Compatibility* 49, no. 2 (): 237–252. doi:10.1109/TEMC.2007.897162.

Poisson, O., P. Rioual, and M. Meunier. 2000. "Detection and measurement of power quality disturbances using wavelet transform". *IEEE transactions on Power Delivery* 15 (3): 1039–1044.

Redfern, M. A., S. C. Terry, F. V. P. Robinson, and Z. Q. Bo. 2003. "A Laboratory Investigation into the Use of MV Current Transformers for Transient Based Protection." In *International Conference on Power Systems Transients (IPST) 2003*, 6. New Orleans, LA: IPST.

Redfern, M. 2004. "The Application of Distribution System Current Transformers for High Frequency Transient Based Protection". In *Eighth IEE International Conference on Developments in Power System Protection*, 2004:108–111. Amsterdam, Netherlands: IEE. ISBN: 978-0-86341-385-8.

Reliability Guideline BPS-Connected Inverter-Based Resource Performance. 2018.

Reynolds, M., G. Beylkin, and L. Monzón. 2013. "Rational approximations for tomographic reconstructions". *Inverse Problems* 29 (6): 065020.

Schweitzer, E. O., B. Kasztenny, and M. V. Mynam. 2016. "Performance of Time-Domain Line Protection Elements on Real-World Faults". In *2016 69th Annual Conference for Protective Relay Engineers (CPRE)*, 1–17. College Station, TX, USA: IEEE. ISBN: 978-1-5090-1532-0.

SEL-T4287. 2020 (accessed June 30, 2020). *SEL-T4287 Traveling-Wave Test System*. https://selinc.com/products/T4287/.

Selman, J. D. 1990. "Evaluation of shunt capacitor switching in power systems using the electromagnetic transients program". PhD thesis, University of Colorado at Denver.

Semlyen, A., and A. Dabuleanu. 1975. "Fast and accurate switching transient calculations on transmission lines with ground return using recursive convolutions". *IEEE Transactions on Power Apparatus and Systems* 94, no. 2 (): 561–571. doi:10.1109/T-PAS.1975.31884.

Shannon, C. E. 1949. "Communication in the Presence of Noise". *Proceedings of the IRE* 37, no. 1 (): 10–21. ISSN: 2162-6634.

Snelson, J. K. 1972. "Propagation of Travelling Waves on Transmission Lines - Frequency Dependent Parameters". *IEEE Transactions on Power Apparatus and Systems* PAS-91, no. 1 (): 85–91. doi:10.1109/TPAS.1972.293294.

Tavighi, A. 2017. "A Frequency-dependent Multiconductor Transmission Line Model with Collocated Voltage and Current Propagation". PhD thesis, University of British Columbia.

Tavighi, A., J. R. Martí, V. A. Galván, and J. A. Gutierrez-Robles. 2018. "Time-Window-Based Discrete-Time Fourier Series for Electromagnetic Transients in Power Systems". *IEEE Transactions on Power Delivery* 33, no. 5 (): 2551–2561. doi:10.1109/TPWRD.2018.2794887.

Vigni, V. L., A. Di Stefano, R. Candela, and E. R. Sanseverino. 2017. "A two-end traveling wave fault location system for MV cables based on LoRa technology". In *2017 IEEE International Conference on Environment and Electrical*

Engineering and 2017 IEEE Industrial and Commercial Power Systems Europe (EEEIC / I& CPS Europe), 1–6. doi:10.1109/EEEIC.2017.7977493.

Wedepohl, L. M. 1993. "Frequency domain analysis of wave propagation in multiconductor transmission systems". *Lecture Notes, Univ. of British Columbia, Dept. of Electrical Engineering, Canada*.

Yan, F., T. Ge, and H. Zhao. 2008. "A New Method of Single-Phase-to-Earth Fault Location for Rural MV Power Networks". In *2008 Joint International Conference on Power System Technology and IEEE Power India Conference*, 1–5. doi:10.1109/ICPST.2008.4745251.

Yarman, C. E., L. Monzón, M. Reynolds, and N. Heaton. 2013. "A new inversion method for NMR signal processing". In *2013 5th IEEE International Workshop on Computational Advances in Multi-Sensor Adaptive Processing (CAMSAP)*, 260–263. IEEE.

Yarman, C. E., R. D. Lewis, and L. Monzon. 2016. *Representing a function bandlimited within a polygonal space*. US Patent 9,442,892.

Zhao, X., Y. Qi, and G. Li. 2011. "Research and implementation of PLC for multiport traveling wave fault location in the medium voltage distribution network". In *2011 4th International Conference on Electric Utility Deregulation and Restructuring and Power Technologies (DRPT)*, 614–617. doi:10.1109/DRPT.2011.5993966.

Zhou, Z., and V. Dinavahi. 2014. "Parallel Massive-Thread Electromagnetic Transient Simulation on GPU". *IEEE Transactions on Power Delivery* 29, no. 3 (): 1045–1053. doi:10.1109/TPWRD.2013.2297119.

Zidan, A., M. Khairalla, A. M. Abdrabou, T. Khalifa, K. Shaban, A. Abdrabou, R. El Shatshat, and A. M. Gaouda. 2017. "Fault Detection, Isolation, and Service Restoration in Distribution Systems: State-of-the-Art and Future Trends". *IEEE Transactions on Smart Grid* 8, no. 5 (): 2170–2185. doi:10.1109/TSG.2016.2517620.